

LA SAPIENZA, UNIVERSITÀ DEGLI STUDI DI ROMA



**DIPARTIMENTO DI INGEGNERIA DELL'INFORMAZIONE, ELETTRONICA E
TELECOMUNICAZIONI.**

**DOTTORATO IN MODELLI MATEMATICI PER L'INGEGNERIA,
ELETTROMAGNETISMO E NANOSCIENZE,
XXIX CICLO.**

Analysis and synthesis of plasmonic devices and metamaterials at optical and terahertz frequencies

Andrea Veroli

Supervisor

Prof. Fabrizio Frezza

Rome, Italy, 2016

To my Irene.

INDEX

CHAPTER 1. – INTRODUCTION.	6
1.2. - References.	9
CHAPTER 2. – THEORY AND FUNDAMENTALS.	11
2.1. - Metamaterials.	11
2.2. - Surface plasmon polaritons.	12
2.3. - Surface plasmon polaritons at a single interface.	16
2.4. - Multilayer system.	21
2.5. - Circular dichroic factor.	26
2.6. - Metamaterial absorbers in THz regime.	27
2.7. - References.	29
CHAPTER 3. – NUMERICAL TAILORING OF LINEAR RESPONSE FROM PLASMONIC NANO-RESONATORS GROWN ON A LAYER OF POLYSTYRENE SPHERES.	32
3.1. - Introduction.	32
3.2. - Numerical modeling.	33
3.3 - Numerical examples.	36
3.4. - Conclusions.	40
3.5. - References.	41
CHAPTER 4. – NUMERICAL EVALUATION OF IRRADIATION DIAGRAM BY PLASMONIC GRATING AND SLIT APERTURES.	44
4.1 - Introduction.	44
4.2. - Numerical scheme.	45
4.3. - Some examples.	49
4.4. - Conclusions.	56

4.4. - References.	57
CHAPTER 5. – ANALYSIS ON VERTICAL DIRECTIONAL COUPLERS WITH LONG RANGE SURFACE PLASMONS FOR MULTILAYER OPTICAL ROUTING.	60
5.1. - Introduction.	60
5.2. - Schematic and settings.	61
5.3. - Parameter Evaluation.	63
A. Coupling length of the straight path.	63
B. Additional coupling computation and control.	64
5.4. - Fabrication torerances.	67
5.5. - Conclusions and future developments.	69
5.6. - Acknowledgments.	71
CHAPTER 6. – FABRICATION TECHNIQUES.	74
6.2. - Vacuum evaporator.	75
6.3. - Sputtering.	77
6.4. - Photolithography.	79
6.5. - Etching.	82
6.6. - Electron beam lithography.	82
6.7. - References.	86
CHAPTER 7. – NANO AND MICRO MANUFACTURING.	87
7.1. - Fabrication of gold nano slit apertures with chirped grating.	87
7.2. - Fabrication of gold nano slit apertures with chirped grating: fabrication process flow.	88
7.3. - EBL study and characterization.	91
7.4. - Dose influence on the PMMA e-Resist for the development of high-aspect ratio and reproducible nanostructures by Electron Beam Lithography.	94
7.4.I. - Introduction.	94
7.4.II. - Material & methods.	95
7.4.III. – Results & discussion.	97

7.4.IV. - Conclusion.	102
7.4.V. - Acknowledgments.	102
7.5. - Fabrication of gold nano slit apertures with chirped grating: fabrication results of the gold grating.	103
7.6. - Fabrication of metamaterial THz absorber.	105
7.8. - References.	110
CHAPTER 8. – PLANAR PLASMONIC BEAN-LIKE NANO-STRUCTURES FOR HIGH DICHROIC FILTERING: THEORY, FABRICATION AND EXPERIMENT.	112
8.1. - Introduction.	112
8.2. - Theoretical Project and FDTD Analysis.	112
8.3. - Fabrication process flow of the nano-beans.	115
8.4. - Measurement setup and results.	116
8.5. - Conclusions.	118
8.6. - References.	118
CHAPTER 9. – CONCLUSION.	120
9.1. - Author's bibliography.	122
ACKNOWLEDGMENTS.	124
APPENDICES.	124
A.1. - Nano-sieve filter for microfluidic sensing on lab-on-chip.	124
A.2. - Nano electro-mechanical systems.	127
A.3 - References	128

Chapter 1. – Introduction.

Fabrication technologies have played a major role ever since the '60s to the rapid growth of information processing, and to the information revolution we are living today; in the electronic industry, by scaling down the size of devices, it has been possible to improve performance, functionality and reliability, all while reducing cost and increasing the production volume of the devices. Industrial success has given more impetus to further research microfabrication and nanofabrication [1 - 3], which has not only propelled more success, but has also opened to scientists and engineers a new array of physical phenomena to study and apply [4]. Over the last decades, the same fabrication apparatus and approach have allowed significant development in the field of optics, plasmonics, metamaterials, microfluidics and even mechanics [5 - 7]; those are still being extensively researched, sometimes in conjunction, for key applications such as: creation of novel materials, increase in volume of computation and communication, precise medical operations, and sensors for chemistry, biology and telecommunication [8 - 10].

As an example, we can take the plasmonics, where the discovering of a subwavelength confinements [11], coupled to the research of new nano-metamaterials [12, 13], has contributed to different families of the nanodevices with unprecedented functionalities, such as subwavelength waveguides [14, 15], optical nanoantennas [16 – 18], superlenses [19, 20], optical invisibility cloaks [21, 22], hyperlenses [23, 24], planar magnifying hyperlens and light concentrators [25, 26].

In this thesis, I present my research activity as a PhD student which encompasses various projects. My main objective has been the analysis and synthesis of plasmonic filters based on metamaterials; I have also worked on a waveguiding systems and gratings-sensors supporting long range surface plasmon polaritons. The activities were focused mainly on optical frequencies, but some devices worked on THz regime.

In the first part of my PhD, I have studied devices working in plasmonic optical frequencies. In order to perform the analysis and design, I have used numerical instruments such as the finite-difference time-domain method (FDTD) included in the software Lumerical FDTD; with the aim to have a numerical comparison for the Lumerical's results I have also used the Finite Element Method (FEM) present in the Comsol Multiphysics software. The post-processing of the simulation's results were performed by using Matlab. I could use these tools in the S.B.A.I. (Basic and Applied Sciences for Engineering at Sapienza University of Rome) department and in the LabCEM2 laboratory of the D.I.E.T. (Department of Information Engineering, Electronics and Telecommunications at Sapienza University of Rome).

To complete and then expand the analysis performed with numerical instruments in the second part of my PhD I have worked on the fabrication of the devices. With the

gradual reduction of the devices' dimension, various challenges have been encountered: as can be seen in later chapters, while research on nano-optics and metamaterials may be mature from an analytical and numerical point of view, there are still many challenges on the actual fabrication of the devices, because of non-ideality of geometrical shapes, materials and chemical composition; sometimes, even the characterization poses as a limiting factor. Thus, a good part of the activities has been the study of compromises between feasibility and performance of the devices: study on the fabrication tolerances and optimum fabrication dosages.

As already told, I have used the same fabrication approach of microelectronics field, which is defined “top down”: externally controlled tools are used to deposit, etch, and shape materials (lithography) into the desired shape. In contrast, the bottom-up approach the devices are fabricated by using the auto-assembly of molecular components through their chemical bonds; these methods are widely used today to manufacture a large variety of useful chemicals such as pharmaceuticals or commercial polymers.

Therefore, I created a nanofabrication procedure following the top-down approach and by using the classic microelectronic processes and techniques: *Spin Coating* followed by *Hot plate* for the deposition of polymer materials; *Vacuum Evaporator* and *Sputtering* for the deposition of metals and *Electron Beam Lithography* to imprint the desired geometry to the devices in nano-fabrication; while, for imprint geometry in micro-fabrication field, I used the standard UV-Lithography. I have performed the processes described above in collaboration with the CNR-IMM (Institute for Microelectronics and Microsystem) of Rome and I could use the *FESEM Zeiss Auriga* system who is kept in the Sapienza's C.N.I.S. (Centro di Ricerca per le Nanotecnologie Applicate all'Ingegneria) laboratory in order to perform the EBL technique. The characterization of the manufactured samples are finally carried out in collaboration with the CNR-Nanotech institute of nanotechnology and University of Palermo.

In the chapter 2 of the present manuscript, are presented the theoretical foundation for my work: the theory and fundamentals of metamaterials and of the surface plasmons. In the chapter 3 I reported the results of the first paper published during my first PhD year: “*Numerical tailoring of linear response from plasmonic nano-resonators grown on a layer of polystyrene spheres*”; in the chapter 4 I report the paper: “*Numerical evaluation of irradiation diagram by plasmonic gratings and slit apertures*” and in the chapter 5 follows the paper: “*Analysis on vertical directional couplers with long range surface plasmons for multilayer optical routing*”. In the chapter 6 the fabrication processes and methods used in my work are listed, while in chapter 7 are shown the fabrication procedures and results for different projects and devices. In chapter 8 is reported the work “*Planar plasmonic bean-like nano-structures*”

for high dichroic filtering: theory, fabrication and experiment” which was submitted at “Nano Innovation 2016”. Finally, the conclusions are set out in chapter 9.

1.2. - References.

- [1] M. Madou. "Fundamentals of Microfabrication", (2nd ed, 2002). ISBN 0-8493-0826-7
- [2] S. Franssila, "Introduction to Microfabrication", (2004). ISBN 0-470-85106-6
- [3] N. P. Mahalik. "Micromanufacturing and Nanotechnology"(2006), Springer, ISBN 3-540-25377-7.
- [4] K. E.Drexler. "Engines of Creation: The Coming Era of Nanotechnology",(1986). Doubleday. ISBN 0-385-19973-2.
- [5] K. E. Drexler. "Nanosystems: Molecular Machinery, Manufacturing, and Computation",(1992). New York: John Wiley & Sons. ISBN 0-471-57547-X.
- [6] L. Coldren, Et al. "Diode Lasers and Photonic Integrated Circuits" (Second ed.). John Wiley and Sons, (2012).
- [7] V. Choudhary, K. Iniewski. "MEMS: Fundamental Technology and Applications". CRC Press, (2013).
- [8] A. Cavalcanti, Et al. "Medical Nanorobot Architecture Based on Nanobioelectronics". Recent Patents on Nanotechnology. 1: 1–10, (2007). doi:10.2174/187221007779814745.
- [9] "Nanotechnology Information Center: Properties, Applications, Research, and Safety Guidelines". American Elements. Retrieved 13 May 2011
- [10] "Nanoscience and nanotechnologies: opportunities and uncertainties". Royal Society and Royal Academy of Engineering. July 2004. Retrieved 13 May 2011.
- [11] S.A. Maier and H.A. At water, J. Appl. Phys. 98, 011101 (2005).
- [12] R.S. Kshetrimayum. "A brief intro to metamaterials". IEEE Potentials, Vol 23, Issue 5, (2005).
- [13] P. R.West, Et al. "Searching for better plasmonic materials", Laser Photonics Rev.4, No.6, (2010).
- [14] S.A. Maier, Et al. "Local detection of electromagnetic energy transport below the diffraction limit in metal nanoparticle plasmon waveguides" Nat. Mater.2, 229–232 (2003).
- [15] S.I. Bozhevolnyi, Et al. "Channel plasmon subwavelength waveguide components including interferometers and ring resonators" Nature440, 508–511 (2006).
- [16] W. Rechberger, Et al. "Optical properties of two interacting gold nanoparticles". Opt. Commun. 220, 137–141 (2003).

- [17] D.P. Fromm, Et al. “Gap-dependent optical coupling of single "bowtie" nanoantennas resonant in the visible”. *Nano Lett.*4, 957–961 (2004).
- [18] T. Atay, Et al. “Strongly Interacting Plasmon Nanoparticle Pairs: From Dipole-Dipole Interaction to Conductively Coupled Regime”. *Nano Lett.* 4, 1627–1632 (2004).
- [19] J.B. Pendry. “Negative refraction makes a perfect lens”. *Phys. Rev. Lett.*85, 3966–3969 (2000).
- [20] N. Fang, Et al. “Sub-diffraction-limited optical imaging with a silver superlens”. *Science*308, 534– 537 (2005).
- [21] U. Leonhardt, “Optical conformal mapping” *Science*312, 1777–1780 (2006).
- [22] A. Al`u and N. Engheta. “Theory and potentials of multi-layered plasmonic covers for multi-frequency cloaking”. *Phys. Rev. Lett.* 100, 113901 (2008).
- [23] A. Salandrino and N. Engheta. “Far-field sub diffraction optical microscopy using metamaterial crystals: theory and simulation”. *Phys. Rev. B* 74, 75103 (2006).
- [24] Z. Liu, Et al. “Far-Field Optical Hyperlens Magnifying Sub-Diffraction Limited Objects”. *Science* 315, 1686–1686 (2007).
- [25] A.V. Kildishev and V.M. Shalaev. “Engineering space for light via transformation optics”. *Opt. Lett.* 33, 43–45 (2008).
- [26] Y. Xiong, Et al. “A simple design of flat hyperlens for lithography and imaging with half-pitch resolution down to 20 nm”. *Appl. Phys. Lett.* 94, 203108 (2009).

Chapter 2. – Theory and fundamentals.

In this section, will present the theoretical foundations of my PhD works. I have firstly studied the plasmonic metamaterials and devices in order to obtain optical integrated components for optical circuits. Then, with the techniques and methods used for the first works, I realized a THz metamaterial absorber. Below a brief introduction on the concept of metamaterial is exposed followed by the basics of the surface plasmon polariton, circular dichroic factor and finally with the absorbers in THz regime.

2.1. - Metamaterials.

In the scientific research the recent progress has brought to relevant results in the synthesis of new material kinds. A *metamaterial* (from the Greek word μετά meta, meaning "beyond") is a material engineered to have a property that is not found in nature [1]. They are manufactured by assembling multiple elements retrieved from composite materials such as metals or plastics. The materials are usually set in repeating patterns, at scales that are smaller than the wavelengths of the phenomena they influence. Their particular shape, geometry, size, orientation and arrangement gives them a new type of properties capable of manipulating electromagnetic waves: by blocking, absorbing, enhancing, or bending waves, to achieve benefits that go beyond what is possible with traditional materials. The potential applications of metamaterials are different: such as optical filters, medical devices, lenses for high-gain antennas, and in many other fields [2, 3].

When appropriately designed metamaterials can affect waves of electromagnetic radiation in a way not observed in classical bulk materials [4, 5]. Those that exhibit a negative index of refraction for particular wavelengths have attracted many significant research [1, 6, 7]. These materials are known as *negative-index metamaterials*. The pioneer of these topic was the Russian physicist V. G. Veselago that in 1968 published the paper “The electrodynamics of substances with simultaneously negative values of ϵ and μ ” [7].

As mentioned above metamaterial are frequently arranged in repeating pattern; in this type of materials the global properties depend on the nature of the pattern rather than on the atomic structures of the matter. The oscillations of the free electrons in high conductive metal such as gold, silver and copper originates an electromagnetic response in the metamaterial; this phenomenon gives a desired resonant reply of the permittivity and permeability. The electromagnetic wave, not able to detect the individual constituent blocks of dimensions less than the wavelength, perceives an average. The medium dimension of the cell, much smaller than wavelength,

characterized the effective homogeneous structure. If this requirement is fulfilled an homogeneous material can be described by the effective macroscopy permittivity $\varepsilon(\omega) = \varepsilon^I(\omega) - i\varepsilon^II(\omega)$ and the effective macroscopy permeability $\mu(\omega) = \mu^I(\omega) - i\mu^II(\omega)$. Appropriately varying $\varepsilon(\omega)$ and $\mu(\omega)$, making them both negative (double-negative DNG), it can obtain *left-handed* (LH) metamaterial (figure 2.1) which performing properties such the regressive propagation, the negative refractive index (NRI), the negative phase velocity medium (NPV) and backward-wave (BW).

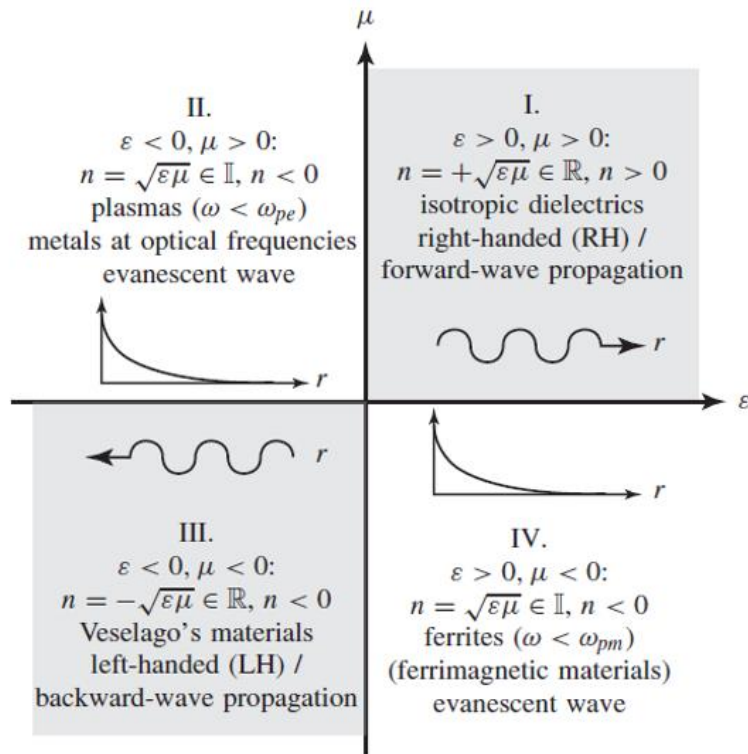


Figure 2.1. Material classification based on permittivity and permeability (Rif. [6]).

Finally, the metamaterials have the ability of creating electrical and magnetic independent reply to the impinging radiation. This feature offers the opportunity of new kind of physical study in the future applications.

2.2. - Surface plasmon polaritons.

The surface plasmon polaritons are electromagnetic excitations which propagate the interfaces between a dielectric and a conductor, confined evanescently in the perpendicular direction. These electromagnetic surface waves appear due to coupling the electromagnetic fields to oscillations of the conductor's electron plasma.

In order to investigate the physical properties of surface plasmon polaritons (SPPs), we have to apply Maxwell's equations to the planar interface between

a conductor and a dielectric.

$$\begin{aligned}
\vec{\nabla} \cdot \vec{D} &= \rho_{ext} \\
\vec{\nabla} \cdot \vec{B} &= 0 \\
\vec{\nabla} \times \vec{E} &= -\frac{\partial \vec{B}}{\partial t} \\
\vec{\nabla} \times \vec{B} &= \vec{J}_{ext} + \frac{\partial \vec{D}}{\partial t}
\end{aligned} \tag{2.1.1}$$

set

$$\vec{\nabla} \times \vec{\nabla} \times \vec{E} = -\mu_0 \frac{\partial^2 \vec{D}}{\partial t^2} \tag{2.1.2}$$

then using the identities $\vec{\nabla} \times \vec{\nabla} \times \vec{E} = \vec{\nabla}(\vec{\nabla} \cdot \vec{E}) - \nabla^2 \vec{E}$, as well as $\vec{\nabla} \cdot (\epsilon \vec{E}) \equiv \vec{E} \cdot \vec{\nabla} \epsilon + \epsilon \vec{\nabla} \cdot \vec{E}$ and presuming the absence of external stimuli $\vec{\nabla} \cdot \vec{D} = 0, \vec{J}_{ext} = 0$, we obtain:

$$\vec{\nabla} \left(-\frac{1}{\epsilon} \vec{E} \cdot \vec{\nabla} \epsilon \right) - \nabla^2 \vec{E} = \mu_0 \epsilon_0 \epsilon \frac{\partial^2 \vec{E}}{\partial t^2} \tag{2.1.3}$$

For negligible changes of the dielectric profile $\epsilon = \epsilon(\mathbf{r})$ over distances on the order of optical wavelength we obtain the **central equation** of electromagnetic wave theory:

$$\nabla^2 \vec{E} - \frac{\epsilon}{c^2} \frac{\partial^2 \vec{E}}{\partial t^2} = 0 \tag{2.1.4}$$

This equation has to be solved separately in regions of constant ϵ and the obtained solutions have to be matched using appropriate boundary conditions. To cast (2.1.4) in a form suitable for the description of confined propagating waves, we proceed in two steps; first, we assume in all generality an harmonic time dependence of the electric field $\vec{E}(\vec{r}, t) = \vec{E}(\vec{r})e^{-j\omega t}$ Inserted into (2.1.4) we obtain:

$$\nabla^2 \vec{E} + k_0^2 \epsilon \vec{E} = 0 \tag{2.1.5}$$

where $k_0 = \frac{\omega}{c}$ is the wave vector of the propagation wave in vacuum.

The equation (2.1.5) is known as *Helmholtz equation*. Now we have to define the propagation geometry. We assume for simplicity a one-dimensional problem, i.e. ϵ depends only on one spatial coordinate. Specifically, the waves propagate along the x-direction of a Cartesian coordinate system, and show no spatial variation in the perpendicular, in-plane y-direction (see Fig. 2.1); therefore, $\epsilon = \epsilon(z)$.

Applied to electromagnetic surface problems, the plane $Z = 0$ coincides with the interface sustaining the propagating waves, which can now be described as $\vec{E}(x, y, z) = \vec{E}(z)e^{j\beta x}$.

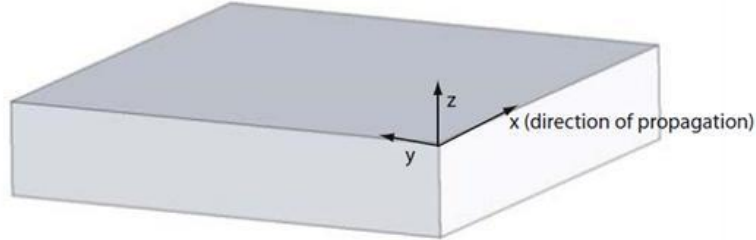


Figure 2.2. Definition of a planar waveguide geometry. The waves propagate along the x direction in a cartesian coordinate system (Rif. [8]).

The complex parameter $\beta = k_x$ is called the propagation constant of the travelling waves and matches to the component of the wave vector in the direction of propagation. Inserting this expression into (2.1.5) we obtain the desired form of the wave equation:

$$\frac{d^2 \vec{E}(z)}{dz^2} + (k_0^2 \varepsilon - \beta^2) \vec{E}(\vec{r}) = 0 \quad (2.1.6)$$

a similar equation exists for the magnetic field $\vec{H}(\vec{r})$.

Equation (2.1.1) is the starting point for the general analysis of guided electromagnetic modes in waveguides. In order to use the wave equation for determining the spatial field profile and dispersion of propagating waves, now we are going to find explicit expressions for the different field components of $\vec{E}(\vec{r})$ and $\vec{H}(\vec{r})$.

This can be done using the third and fourth component of the Maxwell equation (2.1.1). For harmonic time dependence $\left(\frac{\partial}{\partial t} = -i\omega\right)$, we arrive at the following set of coupled equations:

$$\frac{\partial E_z}{\partial y} - \frac{\partial E_y}{\partial z} = i\omega\mu_0 H_x \quad (2.1.7a)$$

$$\frac{\partial E_x}{\partial z} - \frac{\partial E_z}{\partial x} = i\omega\mu_0 H_y \quad (2.1.7b)$$

$$\frac{\partial E_y}{\partial x} - \frac{\partial E_x}{\partial y} = i\omega\mu_0 H_z \quad (2.1.7c)$$

$$\frac{\partial H_z}{\partial y} - \frac{\partial H_y}{\partial z} = -i\omega\varepsilon_0 \varepsilon E_x \quad (2.1.7d)$$

$$\frac{\partial H_x}{\partial z} - \frac{\partial H_z}{\partial x} = -i\omega\varepsilon_0 \varepsilon E_y \quad (2.1.7e)$$

$$\frac{\partial H_y}{\partial x} - \frac{\partial H_x}{\partial y} = -i\omega\varepsilon_0\varepsilon E_z \quad (2.1.7f)$$

For propagation along the x-direction ($\frac{\partial}{\partial x} = i\beta$) and homogeneity in the y direction ($\frac{\partial}{\partial y} = 0$) this system of equation simplifies to:

$$\frac{\partial E_y}{\partial z} = -i\omega\mu_0 H_x \quad (2.1.8a)$$

$$\frac{\partial E_x}{\partial z} - i\beta E_z = i\omega\mu_0 H_y \quad (2.1.8b)$$

$$i\beta E_y = i\omega\mu_0 H_z \quad (2.1.8c)$$

$$\frac{\partial H_y}{\partial z} = i\omega\varepsilon_0\varepsilon E_x \quad (2.1.8d)$$

$$\frac{\partial H_x}{\partial z} - i\beta H_z = -i\omega\varepsilon_0\varepsilon E_y \quad (2.1.8e)$$

$$i\beta H_y = -i\omega\varepsilon_0\varepsilon E_z \quad (2.1.8f)$$

It becomes evident that this system allows two sets of self-consistent solutions with different polarization properties of the propagating waves. The first set is composed by the transverse magnetic (*TM* or *p*), modes, where only the field components E_x , E_z and H_y are nonzero, and the second set the transverse electric (*TE* or *s*) modes, with only H_x , H_z and E_y being nonzero. For *TM* modes, the system of governing equations (2.1.8) reduces to

$$E_x = -i \frac{1}{\omega\varepsilon_0\varepsilon} \frac{\partial H_y}{\partial z} \quad (2.1.9a)$$

$$E_z = -i \frac{\beta}{\omega\varepsilon_0\varepsilon} H_y \quad (2.1.9b)$$

and the wave equation for *TM* modes is

$$\frac{\partial^2 H_y}{\partial z^2} + (k_0^2\varepsilon - \beta^2)H_y = 0 \quad (2.1.9c)$$

For *TE* modes the analogous set is

$$H_x = i \frac{1}{\omega\mu_0} \frac{\partial E_y}{\partial z} \quad (2.1.10a)$$

$$H_z = -i \frac{\beta}{\omega\mu_0} E_y \quad (2.1.10b)$$

with the *TE* wave equation

$$\frac{\partial^2 E_y}{\partial z^2} + (k_0^2\varepsilon - \beta^2)E_y = 0 \quad (2.1.10c)$$

these equations are the basis to begin the description of surface plasmon polaritons.

2.3. - Surface plasmon polaritons at a single interface.

The first geometry that we examine and that can support SPPs is that of a single, flat interface (fig 2.3) between a dielectric, non-absorbing half space ($Z > 0$) with positive real dielectric constant ε_2 and an adjacent conducting half space ($Z < 0$) [8, 10, 11] described via a dielectric function $\varepsilon_1(\omega)$. The requirement of metallic character implies that $Re[\varepsilon_1] < 0$. We want to look for propagating wave solutions confined to the interface, i.e. with evanescent decay in the perpendicular z -direction.

We start with the *TM* solutions. Using the equation set (2.1.9) in both half spaces we obtain:

$$H_y(z) = A_2 e^{i\beta x} e^{-k_2 z} \quad (2.2.11a)$$

$$E_x(z) = iA_2 \frac{1}{\omega \varepsilon_0 \varepsilon_1} k_2 e^{i\beta x} e^{-k_2 z} \quad (2.2.11b)$$

$$E_z(z) = -A_2 \frac{\beta}{\omega \varepsilon_0 \varepsilon_2} e^{i\beta x} e^{-k_2 z} \quad (2.2.11c)$$

for $Z > 0$ and

$$H_y(z) = A_1 e^{i\beta x} e^{k_1 z} \quad (2.2.12a)$$

$$E_x(z) = -iA_1 \frac{1}{\omega \varepsilon_0 \varepsilon_1} k_1 e^{i\beta x} e^{k_1 z} \quad (2.2.12b)$$

$$E_z(z) = -A_1 \frac{\beta}{\omega \varepsilon_0 \varepsilon_2} e^{i\beta x} e^{-k_1 z} \quad (2.2.12c)$$

for $Z < 0$, $k_i \equiv k_{z,i}$ ($i = 1, 2$) is the component of the wave vector perpendicular to the interface in the two media. Its reciprocal value, $\hat{z} = 1/|k_z|$, defines the evanescent decay length of the fields perpendicular to the interface, which quantifies the confinement of the wave. The continuity of $\varepsilon_i E_z$ at the interface requires that $A_1 = A_2$ and

$$\frac{k_2}{k_1} = -\frac{\varepsilon_2}{\varepsilon_1} \quad (2.2.13)$$

Is now needed to point out that with our convention of the signs in the exponents in (2.2.11, 2.2.12), confinement to the surface demands $Re[\varepsilon_1] < 0$ if $\varepsilon_2 > 0$ the surface waves exist only at interfaces between materials with opposite signs of the real part of their dielectric permittivities, i.e. between a conductor and an insulator.



Figure 2.3. Geometry for SPP propagation at a single interface between a metal and a dielectric (Rif. [8]).

The expression for H_y further has to fulfill the wave equation (2.1.9c):

$$k_1^2 = \beta^2 - k_0^2 \varepsilon_1 \quad (2.2.14a)$$

$$k_2^2 = \beta^2 - k_0^2 \varepsilon_2 \quad (2.2.14b)$$

combining this and (2.2.13) we arrive at the central result of this subsection, the dispersion relationship of *SPPs* propagating at the interface between the two half spaces:

$$\beta = k_0 \sqrt{\frac{\varepsilon_1 \varepsilon_2}{\varepsilon_1 + \varepsilon_2}} \quad (2.2.15)$$

This expression is valid both for real and complex ε_l , i.e. for conductors without and with attenuation [8, 9, 10, 12].

Before discussing the dispersion properties of (2.2.15) we now briefly analyze the possibility of *TE* surface modes. Using (2.2.10), the respective expressions for the field components are:

$$E_y(z) = A_2 e^{i\beta x} e^{-k_2 z} \quad (2.2.16a)$$

$$H_x(z) = -iA_2 \frac{1}{\omega \mu_0} k_2 e^{i\beta x} e^{-k_2 z} \quad (2.2.16b)$$

$$H_z(z) = A_2 \frac{\beta}{\omega \mu_0} e^{i\beta x} e^{-k_2 z} \quad (2.2.16c)$$

for $Z > 0$, and:

$$E_y(z) = A_1 e^{i\beta x} e^{k_1 z} \quad (2.2.17a)$$

$$H_x(z) = iA_1 \frac{1}{\omega \mu_0} k_1 e^{i\beta x} e^{k_1 z} \quad (2.2.17b)$$

$$H_z(z) = A_1 \frac{\beta}{\omega \mu_0} e^{i\beta x} e^{-k_1 z} \quad (2.2.17c)$$

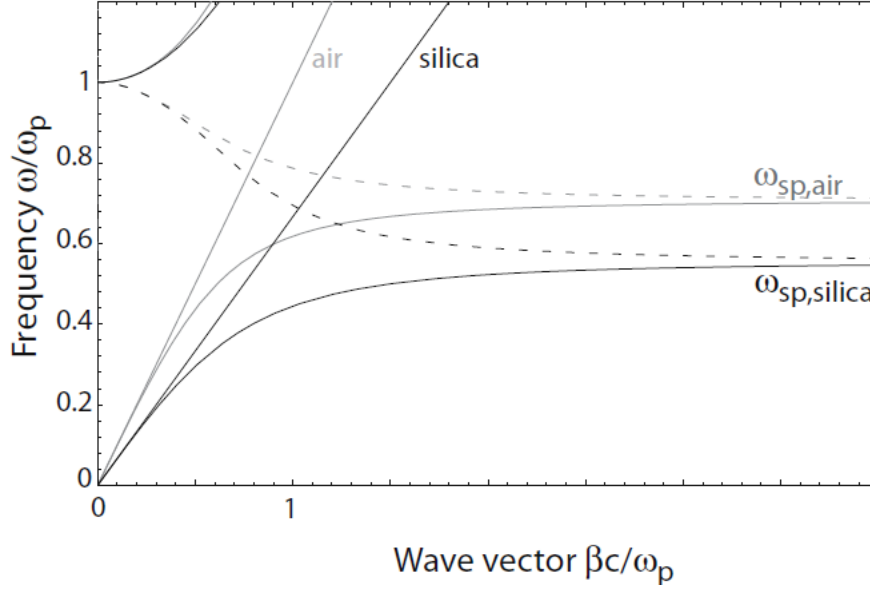


Figure 2.4. Dispersion relationship of SPPs at the interface between a Drude metal with negligible collision frequency and air (gray curves) and silica (black curves); (Rif. [8]).

for $Z < 0$; continuity of E_y and H_x at the interface leads to the condition:

$$A_1(k_1 + k_2) = 0 \quad (2.2.18)$$

Since confinement to the surface requires $Re[k_1] > 0$ and $Re[k_2] > 0$, this condition is only fulfilled if $A_1 = 0$, so that also $A_1 = A_2 = 0$. Therefore, no surface modes exist for TE polarization. Surface plasmon polaritons only exist for TM polarization.

We now want to study the dispersion relation of SPPs. The figure 2.3 shows plots of (2.2.15) for a metal with negligible damping described by the real Drude dielectric function [8, 9], for an air ($\epsilon_2 = 1$) and a fused silica ($\epsilon_2 = 2.25$) interface. In this plot, the frequency ω is normalized to the plasma frequency ω_p , and both the real (continuous curves) and the imaginary part (broken curves) of the wave vector β are shown. Due to their bound nature, the *SPP* excitations correspond to the part of the dispersion curves lying to the right of the respective light lines of air and silica. The radiation into the metal occurs in the transparency regime $\omega > \omega_p$, between the regime of the bound and radiative modes, a frequency gap region with purely imaginary β prohibiting propagation exists. When β is real if it is parallel to the interface and imaginary if orthogonal to the interface.

For small wave vectors corresponding to low (mid-infrared or lower) frequencies, the *SPP* propagation constant is close to k_0 at the light line, and the waves extend over many wavelengths into the dielectric space. In this regime, *SPPs* therefore acquire the nature of a grazing-incidence light field, and are also known as *Sommerfeld-Zenneck* waves [13].

In the opposite regime of large wave vectors, the frequency of the *SPPs* approaches to the characteristic *surface plasmon frequency*.

$$\omega_{SP} = \frac{\omega_P}{\sqrt{1+\epsilon_2}} \quad (2.2.19)$$

as can be shown by inserting the free-electron dielectric function (Drude):

$$\epsilon(\omega) = 1 - \frac{\omega_P^2}{\omega^2 + i\gamma\omega} \quad (2.2.20)$$

in the limit of negligible damping of the conduction electron oscillation (implying $Im[\epsilon_I(\omega)] = 0$). The mode thus acquires electrostatic character, and is known as the *surface plasmon* [8].

It can indeed be obtained by means of straightforward solution of the Laplace equation $\nabla^2\phi = 0$ for the single interface geometry of figure 2.2, where ϕ is the electric potential. A solution that is wavelike in the x-direction and exponentially decaying in the z-direction is given by:

$$\phi(z) = A_2 e^{i\beta x} e^{-k_2 z} \quad (2.2.21)$$

for $Z > 0$ and

$$\phi(z) = A_1 e^{i\beta x} e^{k_1 z} \quad (2.2.22)$$

for $Z < 0$. $\nabla^2\phi = 0$ requires that $k_1 = k_2 = \beta$: the exponential decay lengths $|z| = 1/k_2$ into the dielectric and into the metal are equal. Continuity of ϕ and $\epsilon\partial\phi/\partial z$ ensure continuity of the tangential field components and the normal components of the dielectric displacement and require that $A_1 = A_2$ and additionally:

$$\epsilon_1(\omega) + \epsilon_2 = 0 \quad (2.2.23)$$

For a metal described by a dielectric function of the form:

$$\epsilon(\omega) = 1 - \frac{\omega_P^2}{\omega^2} \quad (2.2.24)$$

this condition is fulfilled at ω_{SP} . Comparison of (2.2.23) and (2.2.15) show that the surface plasmon is indeed the limiting form of a *SPP* as $\beta \rightarrow \infty$.

The above discussions, on the figure 2.4, have assumed an ideal conductor with $Im[\epsilon_I(\omega)] = 0$. Excitations of the conduction electrons of real metals however suffer both for free-electron and interband damping. Therefore, $\epsilon_I(\omega)$ is complex, and with it also the *SPP* propagation constant β . The travelling *SPPs* are damped with an energy attenuation length (also called propagation length) $L = (2Im[\epsilon_I(\omega)])^{-1}$ typically between 10 and 100 μm in the visible regime, depending upon the metal/dielectric configuration in question [8 - 10].

In figure 2.5 it's shown as an example the dispersion relationship of *SPPs* propagating at a silver/air and silver/silica interface, with the dielectric function $\epsilon_1(\omega)$ of silver obtained from Johnson e Christy [8].

Compared with the dispersion relation of completely undamped SPPs depicted in figure 2.4, it can be seen that the bound *SPPs* approach now a maximum finite wave vector at the *surface plasmon frequency* ω_{SP} .

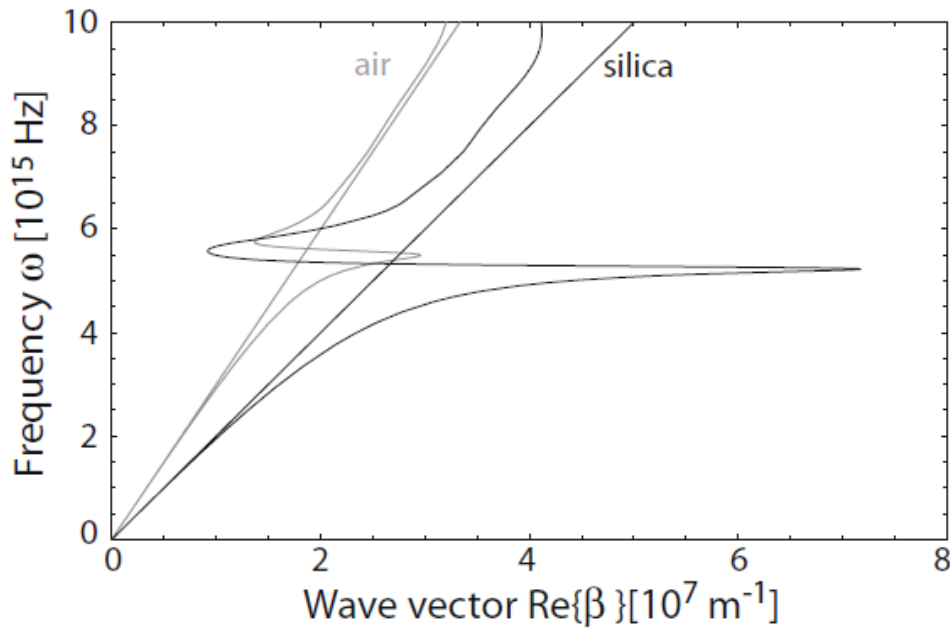


Figure 2.5. Dispersion relationship of SPPs at a silver/air (gray curve) and silver/silica (black curve) interface. Due to the damping, the wave vector of the bound SPPs approaches a finite limit at the surface plasmon frequency (Rif. [8]).

This limitation puts a lower bound both on the wavelength $\lambda_{SP}=2\pi/Re[\beta]$ of the surface plasmon and also on the amount of mode confinement perpendicular to the interface, since the *SPP* fields in the dielectric fall off as $e^{-|k_z||z|}$ with $k_z = \sqrt{\beta^2 - \epsilon_2 \left(\frac{\omega}{c}\right)^2}$. Also, the quasi bound, leaky part of the dispersion relationship between ω_{SP} and ω_P is now allowed, in contrast to the case of an ideal conductor, where $Re[\beta]=0$ is in this regime (figure 2.4).

2.4. - Multilayer system.

Now we are going to study SPPs in multilayers consisting of alternating conducting and dielectric thin films. In such a system, each single interface can sustain bound SPPs. When the separation between adjacent interfaces is comparable to or smaller than the decay length \hat{z} of the interface mode, interactions between SPPs give rise to coupled modes.

In order to elucidate the general properties of coupled *SPPs* we will focus on two specific three layer systems of the geometry depicted in figure 2.6.

In the first system we considered a thin metallic layer (I) sandwiched between two (infinitely) thick dielectric claddings (II) e (III) that realize an insulator/metal/insulator (*IMI*) heterostructure. In the second system a thin dielectric core layer (I) sandwiched between two metallic claddings (II,III) a metal/insulator/metal (*MIM*) heterostructure.

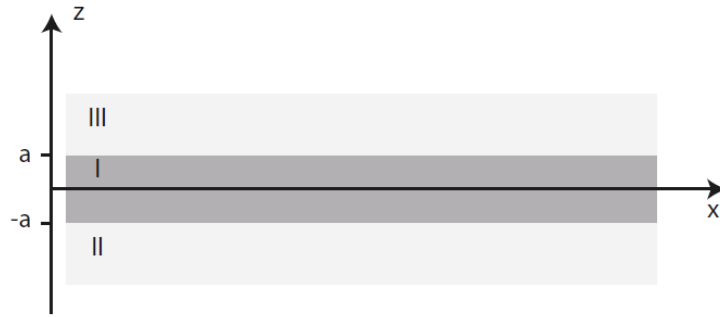


Figure 2.6. Geometry of a three-layer system consisting of a thin layer I sandwiched between two infinite half spaces II and III (Rif. [8]).

Now we are only interested in the lowest-order bound modes, we start with a general description of *TM* modes that are non-oscillatory in the *z*-direction normal to the interfaces, using (2.1.9).

For $Z > a$ the field components are:

$$H_y = A e^{i\beta x} e^{-k_3 z} \quad (2.3.1a)$$

$$E_x = A \frac{1}{\omega \varepsilon_0 \varepsilon_3} k_3 e^{i\beta x} e^{-k_3 z} \quad (2.3.1b)$$

$$E_z = -A \frac{\beta}{\omega \varepsilon_0 \varepsilon_3} e^{i\beta x} e^{-k_3 z} \quad (2.3.1c)$$

while for $Z < -a$ we get:

$$H_y = B e^{i\beta x} e^{k_2 z} \quad (2.3.2a)$$

$$E_x = -iB \frac{1}{\omega \varepsilon_0 \varepsilon_2} k_2 e^{i\beta x} e^{k_2 z} \quad (2.3.2b)$$

$$E_z = -B \frac{\beta}{\omega \varepsilon_0 \varepsilon_2} e^{i\beta x} e^{k_2 z} \quad (2.3.2c)$$

thus, we demand that the field decay exponentially in the cladding **(II)** and **(III)**. Note that we denote the component of the wave vector perpendicular to the interface simply $k_i = k_z, i$.

In the core region $-\alpha < Z < \alpha$, the modes localized at the bottom and top interface couple:

$$H_y = C e^{i\beta x} e^{k_1 z} + D e^{i\beta x} e^{-k_1 z} \quad (2.3.3a)$$

$$E_x = -iC \frac{1}{\omega \varepsilon_0 \varepsilon_1} k_1 e^{i\beta x} e^{k_1 z} + iC \frac{1}{\omega \varepsilon_0 \varepsilon_1} k_1 e^{i\beta x} e^{-k_1 z} \quad (2.3.3b)$$

$$E_z = C \frac{\beta}{\omega \varepsilon_0 \varepsilon_1} e^{i\beta x} e^{k_1 z} + D \frac{\beta}{\omega \varepsilon_0 \varepsilon_1} e^{i\beta x} e^{-k_1 z} \quad (2.3.3c)$$

the requirement of continuity of H_y and E_x leads to

$$A e^{-k_3 a} = C e^{k_1 a} + D e^{-k_1 a} \quad (2.3.4a)$$

$$\frac{A}{\varepsilon_3} k_3 e^{-k_3 a} = -\frac{C}{\varepsilon_1} k_1 e^{k_1 a} + \frac{D}{\varepsilon_1} k_1 e^{-k_1 a} \quad (2.3.4b)$$

at $Z = \alpha$, and:

$$B e^{-k_2 a} = C e^{k_1 a} + D e^{-k_1 a} \quad (2.3.5a)$$

$$-\frac{B}{\varepsilon_2} k_2 e^{-k_2 a} = -\frac{C}{\varepsilon_1} k_1 e^{k_1 a} + \frac{D}{\varepsilon_1} k_1 e^{-k_1 a} \quad (2.3.5b)$$

for $Z = -\alpha$, that is, a linear system of four coupled equations H_y further has to fulfill the wave equation (1.9c) in the three distinct regions, by the equation:

$$k_i^2 = \beta^2 + k_0^2 \varepsilon_i \quad (2.3.6)$$

With $i=1,2,3$. Solving this system of linear equations results in an implicit expression for the dispersion relation linking β and ω via:

$$e^{-4k_1 a} = \frac{k_1/\varepsilon_1 + k_2/\varepsilon_2}{k_1/\varepsilon_1 - k_2/\varepsilon_2} \frac{k_1/\varepsilon_1 + k_3/\varepsilon_3}{k_1/\varepsilon_1 - k_3/\varepsilon_3} \quad (2.3.7)$$

we can note that for infinite thickness ($\alpha \rightarrow \infty$), (2.3.7) reduces to (2.2.13), that is, the equation of two uncoupled *SPP* at the respective interfaces.

At this point we can consider the interesting special case where the sub- and the superstrates **(II)** and **(III)** are equal in terms of their dielectric response, i.e. $\varepsilon_2 = \varepsilon_3$ and thus $k_2 = k_3$. In this case, the dispersion relation (2.3.7) can be split into a pair of equations:

$$\tanh k_1 a = \frac{k_2 \varepsilon_1}{k_1 \varepsilon_2} \quad (2.3.8a)$$

$$\tanh k_1 \alpha \frac{k_1 \varepsilon_2}{k_2 \varepsilon_1} \quad (2.3.8b)$$

It can be shown that equation (2.3.8a) describes modes of odd vector parity ($E_X(z)$, $H_Y(z)$, $E_Z(z)$ are even functions) while (2.3.8b) describes modes of even vector parity ($E_X(z)$, $H_Y(z)$, $E_Z(z)$ are odd).

The dispersion relation (2.3.8a, 2.3.8b) can now be applied to *IMI* and *MIM* structures to investigate the properties of the coupled *SPP* modes in this two systems. We start with the *IMI* geometry: a thin metallic film of thickness 2α sandwiched between two insulating layers. In this case $\varepsilon_1 = \varepsilon_1(\omega)$ represents the dielectric function of the metal, and ε_2 the positive, real dielectric constant of the insulating sub- and superstrates. The figure 2.7 shows the dispersion relation of the odd and even modes (2.3.8a, 2.3.8b) for an air/silver/air geometry for two different thicknesses of the silver thin film. For making it simpler, here the dielectric function of silver is approximated via a Drude model with negligible damping (2.2.24) so that $Im[\beta] = 0$.

The odd modes have frequencies ω_+ higher than the respective frequencies for a single interface *SPP*, and the even modes lower frequencies ω_- . For large wave vectors β which are only achievable if $Im[\varepsilon(\omega)] = 0$ the limiting frequencies are:

$$\omega_+ = \frac{\omega_p}{\sqrt{1+\varepsilon_2}} \sqrt{1 + \frac{2\varepsilon_2 e^{-2\beta a}}{1+\varepsilon_2}} \quad (2.3.9a)$$

$$\omega_- = \frac{\omega_p}{\sqrt{1+\varepsilon_2}} \sqrt{1 - \frac{2\varepsilon_2 e^{-2\beta a}}{1+\varepsilon_2}} \quad (2.3.9b)$$

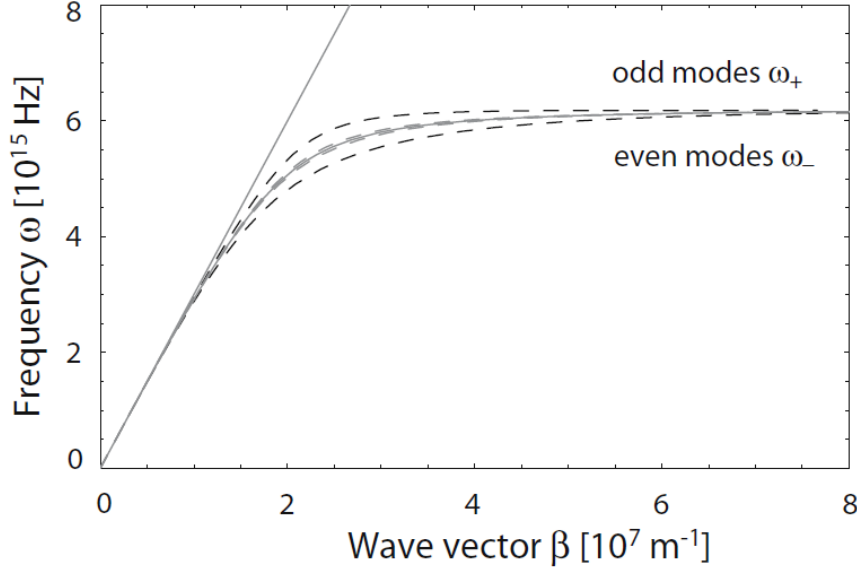


Figure 2.7. Dispersion relation of the coupled odd and even modes for an air/silver/air multilayer with a metal core of thickness 100 nm (dashed gray curves) and 50 nm (dashed black curves). It is also shown the dispersion of a single silver/air interface (gray curve). Silver is modeled as a Drude metal with negligible damping (Rif. [8]).

Odd modes have the interesting property that upon decreasing metal film thickness, the confinement of the coupled *SPP* to the metal film decreases as the mode evolves into a plane wave supported by the homogeneous dielectric environment. For real, absorptive metals described via a complex $\varepsilon(\omega)$, this implies a drastically increased *SPP* propagation length [8 - 10]. The even modes exhibit the opposite behaviour: their confinement to the metal increases while decreasing metal film thickness, so resulting in a reduction in propagation length.

Moving on to *MIM* geometries, we now set $\varepsilon_2 = \varepsilon_2(\omega)$ as the dielectric function of the metal and ε_1 as the dielectric constant of the insulating core in equations (2.3.8a, 2.3.8b). From an energy confinement point of view, the most interesting mode is the fundamental odd mode of the system, which does not exhibit a cut-off for vanishing core layer thickness [8 - 10].

Figure 2.8 shows the dispersion relationship of this mode for a silver/air/silver heterostructure. This time, the dielectric function $\varepsilon(\omega)$ was taken as a complex fit to the dielectric data of silver obtained by Johnson and Christy [8]. Thus β does not go to infinity as the surface plasmon frequency is approached, but folds back and eventually crosses the light line, as for *SPPs* propagating at single interfaces.

It is apparent that large propagation constants β can be achieved even for excitation well below ω_{SP} , provided that the width the dielectric core is chosen is sufficiently small. The ability to access such large wave vectors and thus small penetration lengths \hat{z} into the metallic layers by adjusting the geometry indicates that localization effects that for a single interface can only be sustained at excitations near ω_{SP} , can for such *MIM* structures also be attained for excitation out in the infrared. For more detail

consult the reference [8].

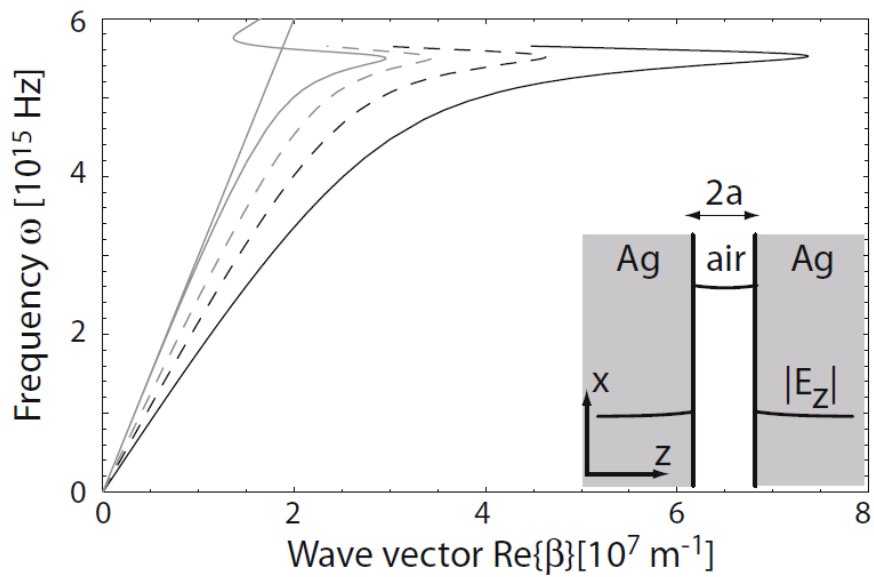


Figure 2.8. Dispersion relation of the fundamental coupled SPP modes of a silver/air/silver multilayer geometry for an air core of size 100 nm (broken gray curve), 50 nm (broken black curve), and 25 nm (continuous black curve). Also shown is the dispersion of a SPP at a single silver/air interface (gray curve) and the air light line (gray line) (Rif. [8]).

2.5. - Circular dichroic factor.

Chirality is a geometry notion who refer to property of asymmetry important in several branches of science. The term *chiral* comes from Greek word “*chiro*” which means precisely “hand”, like the left hand that is a non-superimposable mirror image of the right hand: no matter how the two hands are oriented, it is impossible for all the major features of both hands to coincide across all axes; an object can be defined as chiral if it cannot be brought into congruence with its mirror image by translation and rotation, acquiring a left or right handedness [14,15]. A chiral object and its mirror image are called enantiomorphs (Greek opposite forms) or, when referring to molecules, enantiomers.

The chirality effects can be observed and studied in 3D [16], 2D [17], and even in 1D systems [18]. Chirality plays a key role in the life of plants, animals and also pharmaceutical, agricultural and other chemical industries. In particular, in pharmaceutical industries, 56% of the drugs currently in use are chiral products and the 88% of the last ones are marketed as racemates consisting of an equimolar mixture of two enantiomers [19].

In the electromagnetic field, regarding electromagnetic wave propagation, *Circular polarization* is the polarization such that of the tip of the electric field vector when describes a helix. The magnitude of the electric field vector is constant and the projection of the tip of the electric field vector upon any fixed plane intersecting, and normal to, the direction of propagation, describes a circle. Circular polarization may be referred to as "right-hand" or "left-hand," depending on whether the helix describes the thread of a right-hand or left-hand screw, respectively. *Circular dichroism (CD)* is dichroism involving circularly polarized light, i.e., is the particular ability of a material to make waves the differential absorption of left- and right-handed light. This characteristic is generally obtained by the use of elements with chiral shape, i.e., it can be achieved in metamaterials, through a process of engineering the elementary cell of a periodic structure [20] or by the particular alignment of a material with no real intrinsic chirality, settled with an orientation such as it breaks the symmetry of the system. In this particular ultimate case, it is called extrinsic or induced chirality [21 – 24].

SPPs based devices have been demonstrated to be very attractive for photonic applications in many areas such as nano-optics [25], wave-guiding [26], near-field optical microscopy [27] and biomedical sensing [28,29], because of their sub-wavelength scale features and field enhancement effect [30]; the plasmonic structures can also enhance interaction with circularly polarized light and some exhibit strong chiroptical effects and thus an important CD [16, 31].

In this manuscript in order to give an estimate of the CD of the design and manufactured device afterward the *circular dichroic factor*(*CDF*) is defined as:

$$CDF = 2 \frac{T^+ - T^-}{T^+ + T^-} \quad (2.4)$$

where T^+ and T^- are the output transmission spectra, respectively, for left and right circularly polarized impinging waves, at a given wavelength.

2.6. - Metamaterial absorbers in THz regime.

In the last decades, there was an increased interest on the metamaterials working in tera hertz regime, commonly named THz gap. The THz bandwidth has not been classified until the devices working in this regime are became strategic for civil and military security. The benefits of THz frequency band originate from the fact of following wave can cross the bodies, making visible hidden metallic objects in different coatings (like the micro-wave also can do) but, at the same time, they have a radius nature rather than wave; this feature guarantees to recreate an imagine with very high detail level [32, 33].

With the metamaterials (section 2.1) researchers can obtain new electromagnetic characteristics, some not possible with the use of natural materials; thanks to their properties to be geometrically scaled in order to obtain desired electromagnetic response in the various frequency bandwidths. So the metamaterial devices can be working in different spectral ranges: radio-wave, micro-wave, infrared and even in optical frequencies. This relevant feature is largely exploit in the THz technologies [34, 35].

An important class of THz device are the *metamaterial perfect absorbers* (MPAs); they can be successfully used in applications such as emitters, sensors, spatial light modulators, wireless communications, and in thermo-photovoltaic devices [36]. The MPAs, in according with the metamaterials theory, can be described as an effective medium that allows the designer to control the electromagnetic properties by varying the geometry. The *near unity* ideal absorber is a device in which all incident radiation are absorbed in the working frequency. Finally, the extremely thin substrate of the MPAs bypasses the traditional limit of physical dimension due to diffraction.

The MPAs are divided into two groups: *resonant absorbers* and *broadband absorbers*. The resonant absorbers take advantage of the material interaction with the impinging radiation at a specific frequency. The realization of these type of absorbers, consists in the juxtaposition of multiple layers separated by a distance equal to a quarter

of the working wavelength. Following the theory of the transmission lines, the impedance of the perfect electric conductor, i.e. a short circuit, becomes an open circuit at $\lambda/4$ distance (where λ is the wavelength) [37]. When the load impedance is adapted to that free space the reflection tends to zero. For introducing additional losses it is possible to achieve a high absorption peak, which is influenced strongly by the screen resistance, the permittivity of the dielectric and the angle of incidence. The broadband absorbers instead using materials whose properties don't depend by frequency, and have the ability to absorb the radiation of a wider band of frequencies [38]. Examples of this type of MPAs are absorbers with geometric transition commonly used in anechoic rooms: this models, which take advantage of forms such as pyramids and wedges with appropriate loads, slowly realizes a transition from space variable free to the material losses; the reflection is minimized and the wave is gradually absorbed by the elements that make up the structure. Broadband absorbers have expanded to THz the range of working frequencies with the use of metamaterials components.

2.7. - References.

- [1] R. A. Shelby, Et al. "Experimental Verification of a Negative Index of Refraction". *Science*. 292 (5514): 77–79, (2001).
- [2] M. Brun, Et al. "Achieving control of in-plane elastic waves". *Appl. Phys. Lett.* 94 (61903): 1–7, (2009).
- [3] Alici, Et al. "Radiation properties of a split ring resonator and monopole composite". *Physical status solid (b)*. 244 (4): 1192–1196, (2007).
- [4] Engheta, Et al. "Metamaterials: Physics and Engineering Explorations". Wiley & Sons. (2006).
- [5] Zouhdi, Et al. "Metamaterials and Plasmonics: Fundamentals, Modelling, Applications". New York: Springer-Verlag, (2008).
- [6] J. B. Pendry. "Negative Refraction" *Contemporary Physics*. Princeton University Press, (2004).
- [7] V. G. Veselago. "The electrodynamics of substances with simultaneously negative values of ϵ and μ ". *Soviet Physics Uspekhi*. 10 (4): 509–514, (1968).
- [8] S. A. Maier. "Plasmonics: Fundamentals and Applications". Springer Science Business Media, LLC University of Bath, Department of Physics, (2007).
- [9] Michael G. Et al. "Introduction to Surface and Superlattice Excitations". Cambridge University Press, (1989).
- [10] H. Raether. "Excitation of plasmons and interband transitions by electrons". Springer-Verlag, (1980).
- [11] Zayats, Et al. "Nano-optics of surface plasmon polaritons". *Physics Reports*, 408 (3–4): 131–314, (2005).
- [12] Barnes, Et al. "Surface plasmon subwavelength optics". *Nature*, 424 (6950): 824–830, (2003).
- [13] G. Goubau. "Surface waves and their application to transmission lines", *J. Appl. Phys*, vol. 21, pp. 1119–1128, (1950).
- [14] G. H. Wagnière. "On Chirality and the Universal Asymmetry: Reflections on Image and Mirror Image, (2007).
- [15] Sir William Thomson Lord Kelvin. "The Molecular Tactics of a Crystal". Clarendon Press, (1894).
- [16] M. Esposito, Et al. "Triple-helical nanowires by tomographic rotatory growth for chiral photonics", *ncomms* 7484. doi: 10.1038, (2015).

- [17] R. Raval, “Mirrors in Flatland”, *nature*, Vol. 425, (2003).
- [18] C. Rizza, Et al. “One-dimensional chirality: strong optical activity in epsilon-near-zero metamaterials”, *PhysRevLett.* 115.057401, (2015).
- [19] R. A. Estevesde Castro, Et al. “Infrared spectroscopy of racemic and enantiomeric forms of atenolol”. *SpectrochimicaActa Part A* 67, (2007).
- [20] M. Esposito, Et al. “Three dimensional three dimensional chiral metamaterial nanospirals in the visible range by vertically compensated focused ion beam induced-deposition”. *Adv. Opt. Mater.* 2(2), (2014).
- [21] T. Verbiest, Et al. “Light-polarization-induced optical activity”. *Phys. Rev. Lett.* 82(18), 3601 (1999).
- [22] E. Plum, Et al. “Metamaterials: optical activity without chirality”. *Phys. Rev. Lett.* 102, 113902 (2009).
- [23] K. Konishi, Et al. “Circularly polarized light emission from semiconductor planar chiral nanostructures”. *Phys. Rev. Lett.* 106, 057402 (2011).
- [24] A. Maksimov, Et al. “Circularly polarized light emission from chiral spatially structured planar semiconductor microcavities”. *Phys. Rev. B* 89, 045316 (2014).
- [25] J. Miao, Et al. “Far-Field Focusing of Spiral Plasmonic Lens”. *Plasmonics* 7:377–381, (2012).
- [26] A. Mahigir, Et al. “Plasmonic coaxial waveguide-cavity devices”. *OSA*, Vol. 23, No. 16, (2015).
- [27] T. Ishi, Et al. “Si Nano-Photodiode with a Surface Plasmon Antenna”. *jap*, Vol. 44, No. 12, (2005).
- [28] O. S. Wolfbeis, “Fiber-Optic Chemical Sensors and Biosensors”. *Anal. Chem.* 76, 3269-3284, (2004).
- [39] K. Kurihara, Et al. “Fiber-optic conical microsensors for surface plasmon resonance using chemically etched single-mode fiber”. *Analytical Chemical Acta* 523, (2004).
- [30] W. Knoll, “Interfaces and thin film as seen by bound electromagnetic waves”. *Annu. Rev. Phys. Chem.* 49:569–638, (1998).
- [31] N. Engheta, D. L. Jaggard, “Electromagnetic Chirality and Its Applications”. *IEEE Antennas and Propagation Society Newsletter*, October 1988.
- [32] J. Trontelj, A. Sesek. “Electronic terahertz imaging for security applications”. *SPIE Newsroom* (2016).
- [33] J. F. Federici, Et al. “THz imaging and sensing for security applications—explosives, weapons and drugs”. *Semicond. Sci. Technol.* 20, (2005).

- [34] J. F. O'Hara, Et al. "Properties of planar electric metamaterials for novel terahertz applications", Journal of nanoelectronics and optoelectronics, vol. 2, (2007).
- [35] W. J. Padilla, Et al. "Electrically resonant terahertz metamaterials: theoretical and experimental investigations", Physical Review, vol. 75, (2007).
- [36] N. I. Landy, Et al. "Perfect metamaterial absorber", Phys. Rev. Lett., vol. 100, (2008).
- [37] F. Frezza, "Compendio di campi elettromagnetici", Aracne, Roma, (2013).
- [38] C. M. Watts, Et al. "Metamaterial electromagnetic wave absorbers", Advanced Optical Materials, vol. 24, n. 23, (2012).

Chapter 3. – Numerical tailoring of linear response from plasmonic nano-resonators grown on a layer of polystyrene spheres.

3.1. - Introduction.

In recent years, nanotechnology has become one of the most intriguing, explored, and above all promising research sectors [1, 2]. It actually refers to an entire world of scientific fields whose common task is to reach the highest order of integration for electronic [3, 4], mechanic [5, 6], and electromagnetic (e.m.) [7, 8] devices, together with the smallest power consumption and processing speed. The embracement of nano-scale fabrication allows to manipulate the light signal toward the optical range, thanks to the adoption of linear [9, 10] and non-linear optical materials [11, 12].

Unfortunately, the realization of large areas nanostructured materials operating in the visible range requires state of art technologies and high fabrication costs. For this reason, self-assembly techniques are extremely appealing [13]. They allow the development of highly structured, large area materials without the need of slow and expensive serial operations.

Self-assembly techniques has been widely used to produce meta-surface composed by nano-resonators as efficient filters in the microwave (MW) [14, 15], THz [16, 17], infrared (IR) [18], and optical [19] regime. In Ref. 20, were described a technique to develop golden nano-resonators grown by evaporation at grazing incidence on top of a polystyrene (PS) artificial opals' layer on a glass substrate. The choice of PS has been made for both its mechanical and electromagnetic properties, like its low absorption coefficient in the visible and near infrared ranges, and its robustness and light weight, which allows to easily manipulate the micro-spheres and collect them into a suitable substrate. At the same time, the gold has been chosen among the noble metals primary for its major chemical stability in many environments. This technique is promising because is easily controllable and shows high levels of accuracy for the realized samples. Indeed, the shape acquired by the nano-resonators, acting as antennas, allows making these artificial materials to be functional as anisotropic optical filters with controllable resonant frequencies, and appear to be natural candidates as alternatives to the conventional electrodes for the new generations of optically enhanced solar cells and highly integrated sensors [20].

In Refs. 21 and 22 have been reported second harmonic generation (SHG) measurements showing a dichroic behavior both for linearly and circularly polarized waves. Dichroism is the ability of a material to selectively absorb a radiation with a particular polarization orientation. Circular dichroism (CD) is the particular ability of a material to make waves presenting opposite sense of circular polarization be absorbed by different amounts. This feature is generally achieved by the use of elements with chiral shape, i.e., elements which do not superpose with their mirror image with respect to a reference direction [23]. It can be obtained in metamaterials, by engineering the elementary cell of a periodic structure (in this case we have intrinsic or true chirality) [24,25] or by the particular alignment of a material with no real intrinsic chirality, placed with an orientation such that it breaks the symmetry of the system. In this latter

case, it is called extrinsic (induced) chirality [26 – 31]. Linear dichroism (LD) is present in this class of metasurface too, and we will provide a brief description of this behavior in the same structures.

In this chapter, we investigate the transmission properties of a generic configuration of self-assembled Au and Ag nano-resonators on the PS spheres' layer through the use of numerical calculations based on a finite difference time domain (FDTD) method. By modeling the elements involved in the simulations, we are able to predict resonant effects and spectral behaviors, which makes this class of artificial materials promising for compact size light manipulators, either for circularly or linear polarized plane waves.

The aim of this work is to gain full insights into the fundamental phenomenon, which will provide the reader with a further comprehensive explanation about the linear behavior of the samples shown in Ref. 22, and to numerically obtain the most suitable configuration able to enhance the CD and LD responses in this class of metamaterials. In subsection 2, a brief description of the numerical modeling is presented, focusing on the beam and shadows projections at the base of process to determine the shapes of the metal nanoparticles on top of the PS spheres. In Sub. 3, we analyze the numerical results and evaluate the dichroic factor and the anisotropic nature for each configuration according to the relative transmission spectra. Finally, in Sub. 4, the main conclusions are drawn.

3.2. - Numerical modeling.

The artificial material is composed of a regular array of plasmonic scatterers produced by grazing evaporating gold upon a self-ordered disposition of polystyrene nanospheres under hexagonal arrangements. The overall structure is a hybrid plasmonic-photonics nanostructure (HPPN), which can be considered as a meta-surface for its contained size along the orthogonal direction to the deposition plane. Due to the morphology of the gold nano-elements, the overall structure presents several e.m. properties in both linear and circular polarized light [32] as experimentally verified in Ref. 22 by using SHG technique.

To investigate the several properties of the meta-surface in linear regime, we made a transposition of the experimental fabrication process into a numerical counterpart by the use of primitives elements as spheres and cylinders, as suggested by Figure 3.1.

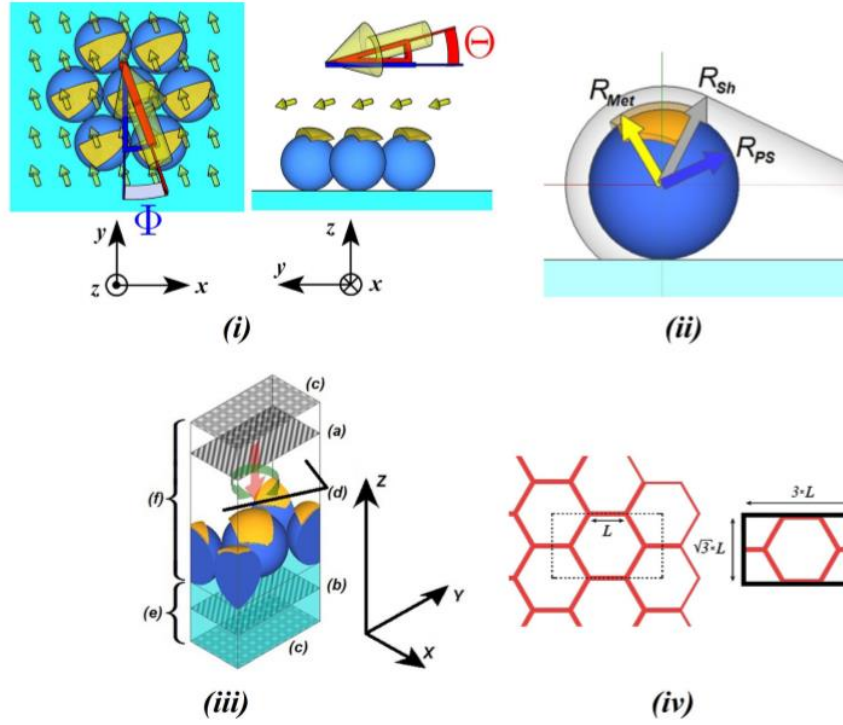


Figure 3.1. (i) schematic view of the geometrical technique used to model the metal nano-antennas (yellow) grown upon the PS spheres (blue-violet), which follow a periodic hexagonal distribution on a glass substrate (blue). The modeling is provided by the interaction of the metal vapor flux against the PS spheres. It projects a shaded region (transparent) outside which the metal deposition is possible. In (ii), definition of the 3 radii for the PS-sphere (R_{PS}), gold layer (R_{Met}), and shaded region (R_{Sh}). (iii) The elementary periodic cell modeled in the numerical simulations. A plane wave emitted by an input plane (a) reaches the metasurface whose located in the air region (f) and is partially transmitted toward the substrate (e), where another plane (b) has been placed to evaluate the transmittance. The cell has been confined setting perfect matching layers (PML) for the 2 sides normal to the z direction (c), and PBC for the 4 sides whose normal lay parallel to the x and y axes (d). (iv) Depiction of a portion of the entire periodic set with hexagonal distribution and top-view of the periodic elementary box, with relative proportions.

We used the definition of the two types of circular polarized waves, i.e., left-handed (L) and right-handed (R), as depicted in Fig. 3.2, by following the convention in conformity with the IEEE standard [33].

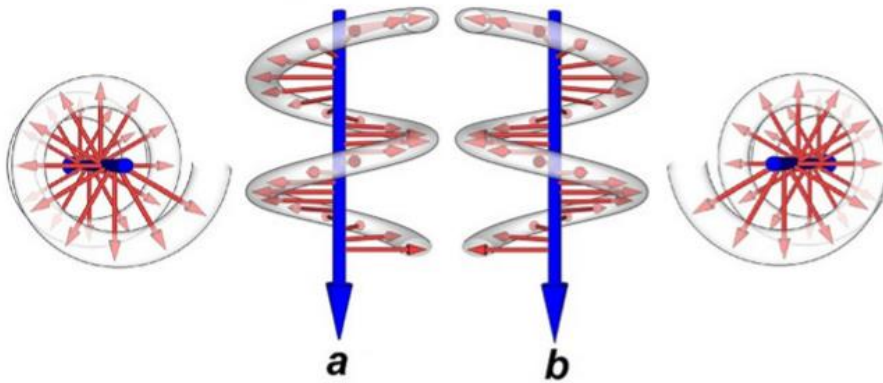


Figure 3.2. Convention adopted for the circular polarization. The Poynting vector and the electric field, as in an fixed instant of time during the propagation process, are depicted in blue and red, respectively. In (a) left handed/counter-clockwise polarized wave, in (b) right handed/clockwise polarized wave.

The metal resonators upon each PS sphere has been modeled by the application of etching regions, which emulate the shadows, produced by the PS spheres, projected by the metal vapor flux during the deposition process [20]. These etching regions assume an orientation as a function of two angles H and U , describing the orientation of the gold flux (yellow arrow in Fig. 3.1(i)). The two angles are indicated in Figure 3.1(i) in red and blue, respectively. The shadows determine the shape of the metal particle upon the PS spheres' layer, thus they strongly affect the optical properties of the entire sample, by controlling the resonant response of each particle, which behaves as an antenna.

The metal layer has been set to 10nm in thickness in order to fit the experimental results obtained in Ref. 22. This value is directly dependent on the technique adopted to grow the samples. Furthermore, in order to provide the right spacing between nano-resonators, the shaded region has been described adopting spheres and cylinders with augmented radii with respect to the PS spheres' radius. Indeed, a certain shrinking effect is observed in the experimental case [22], thus the resonator will be smaller in size than the free region exposed to the metal vapor flux.

We took into account this effect by adding a further shadow enlargement, whose value has been chosen after a speculative investigation of the previous experimental samples [22]. To assign the correct size and mutual spacing in the case of PS sphere with a diameter 250nm in size, we assumed the following formula:

$$R_{Sh} = R_{PS} + (2.32 \cdot \theta + 0.25 \cdot \phi - 0.008 \cdot \theta \cdot \phi - 8)[nm] \quad (3.1)$$

valid for the range $[0^\circ, 30^\circ]$ for both U and H , with the meaning of R_{Sh} and R_{PS} being explained in Fig. 1(ii).

Adopting a rectangle-based geometry for all the CAD stages of our numerical simulations (see Fig. 1(iii)), we used periodic boundary conditions (PBC) to emulate the infinite extension along the x and y directions of the meta-surface. All the simulations have been performed under Lumerical FDTD Solutions. We delimited the entire system along the z direction by placing two opposite absorbing boundary layers, one in the background region laying on the top and the other in the region filled by the substrate glass below the metasurface. The transmission spectra have been always evaluated for normally impinging plane waves. The final spectra have been evaluated by multiplying the results of the simulations with the theoretical glass-to-air transmission coefficient to take into account the final transmittance in air avoiding the spurious multiple coherent reflections between opposite substrate faces. In real samples, the substrate's thickness is around 1mm, therefore the inclusion of the entire glass substrate into the simulation region would give rise to unexpected and unrealistic etalon effects.

To reduce numerical errors, we adopted a sufficiently dense mesh (about 1.2nm) for the FDTD processing.

3.3 - Numerical examples.

In order to give an estimate of the CD of the metasurface, we will consider both the case of gold (Au) and silver (Ag) [34] nano-resonators. We afterwards defined the circular dichroic factor (CDF) as

$$CDF(\Phi, \Theta) = \frac{I_L(\Phi, \Theta) - I_R(\Phi, \Theta)}{I_L(\Phi, \Theta) + I_R(\Phi, \Theta)} \quad (3.2)$$

where I_L and I_R are the output intensities for left and right circularly polarized impinging waves, respectively, at a given wavelength.

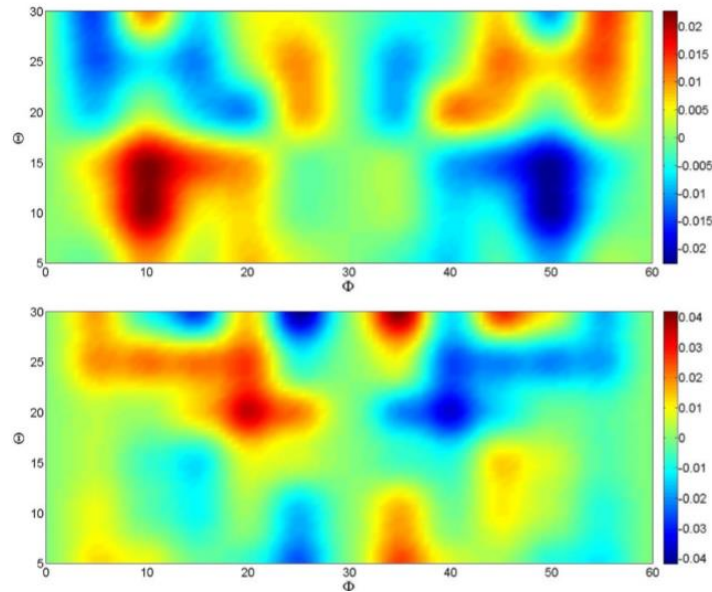


Figure 3.3. CDF map for Au (above) and Ag (below) nano-resonators over PS spheres as a function of Φ and Θ at $\lambda = 800nm$. Inside the angular region of our investigation, peak values of the CDF are approximately $2.1E-2$ and $4E2$, for gold and silver respectively, at $\lambda = 800nm$.

Previously [22] was measured the chiral nature of samples composed of gold-on-PS resonators and was detected a noticeable amount of chirality at $\lambda = 800nm$ by the means of the SH generated field at $\lambda = 400nm$. Due to the nonlinear effect of SHG, the measured CDF at the fundamental field could be affected by the intrinsic chirality experienced by the beams at both fundamental and SH frequencies. However, an evaluation of the CDF at 400nm reveals that the CDF peak value at the SH wavelength is approximately 350 times weaker than the CDF peak at the fundamental one due to the lack of an effective plasmon resonance and fields' localization at the SH frequency.

In Fig. 3.3, we report the CDF calculated at a fixed wavelength of 800nm for both *Au* and *Ag* NP as a function of Φ and Θ for 250nm diameter spheres.

We considered different values of Φ from 0° to 60° , after which the CDF profile is repeated periodically because of the symmetry of the elementary cell in the hexagonal lattice. A maximum value of Θ equal to 30° has been set because for larger H part of the evaporated gold can be deposited directly on the substrate through the spaces between adjacent spheres. The theoretical maximum allowed Θ for $\Phi = 0$ and $\Phi = 30$, respectively, is given by

$$\max\{\Theta\}_{\Phi=0} = \frac{180}{\pi} \arctan\left(\frac{\sqrt{2}}{2}\right),$$

$$\max\{\Theta\}_{\Phi=30} = \frac{180}{\pi} \arctan\left(\frac{\sqrt{2\sqrt{3}-3}}{\sqrt{4-3\sqrt{3}}}\right), \quad (3.3)$$

which are approximately equal to 35.3° and 40.9° , respectively.

From Fig. 3.3, it is possible to retrieve the Φ and Θ that give rise to the maximum response in terms of CDF. For *Au* nano-resonators, we reported a CDF peak approximately of 0.02 belonging to the configuration associated with the angular couple $(\Phi, \Theta) = (10^\circ, 14^\circ)$; whilst for *Ag* nano-resonators, we registered a sharp peak of 0.038 for $(\Phi, \Theta) = (20^\circ, 20^\circ)$. The reason behind this small but evident difference in transmittance for the two opposite signs of circular polarization resides in the different field localization across the elementary metal resonator (see Figure 4).

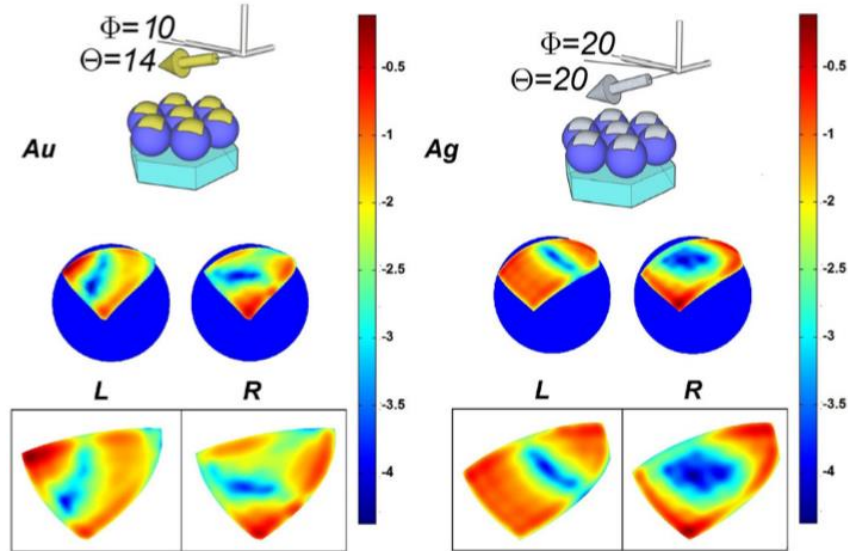


Figure 3.4. Logarithmic profile of intensity (with respect to the maximum value) for *Au*-($10^\circ, 14^\circ$) (left) and *Ag*-($20^\circ, 10^\circ$) (right). For both left (L) and right (R) circular polarisation, the top view of the 3D profile on the nano-resonator's surface are shown. The shadow radii are 151nm and 165nm for the the gold and silver configurations, respectively (250nm diameter PS spheres).

This is allowed by the chiral nature of the 2D projection of the resonators toward the O_{xy} plane, and it receives a further enhancement by the bending of this surface across the superior PS hemisphere. A different field localization means different resonances for the single nano-resonator according to the sign of the circular polarization. In the following, we will refer to these latter configurations as Au -(10° , 14°) and Ag -(20° , 20°), respectively.

In Figure 3.5, we show the transmission spectra (Figs. 3.5(a) and 3.5(c)) of circular polarised light together with the CDF spectra (Figs. 3.5(b) and 3.5(d)) for gold and silver resonators. Cut-off limits in the CDF are observed approximately above 600nm for gold and 480nm for silver due to the surface plasmon polariton (SPP) response in metals, which are the responsible for the resonant behavior of the resonators and their consequent circular dichroic effects with normally impinging waves. The sharp peak commonly retrieved for both circular signs around 325nm is a Bragg resonance due to the hexagonal disposition of PS spheres, and its spectral location in terms of wavelengths is directly proportional to the sphere's diameter, with a general peak-to-diameter ratio of 1.3 for any configuration. We note that a zero value of the CDF does not necessary mean equal behavior for the two opposite circular senses. Indeed, the meta-surface is also responsible for different phase alteration of the impinging wave for the left and right senses.

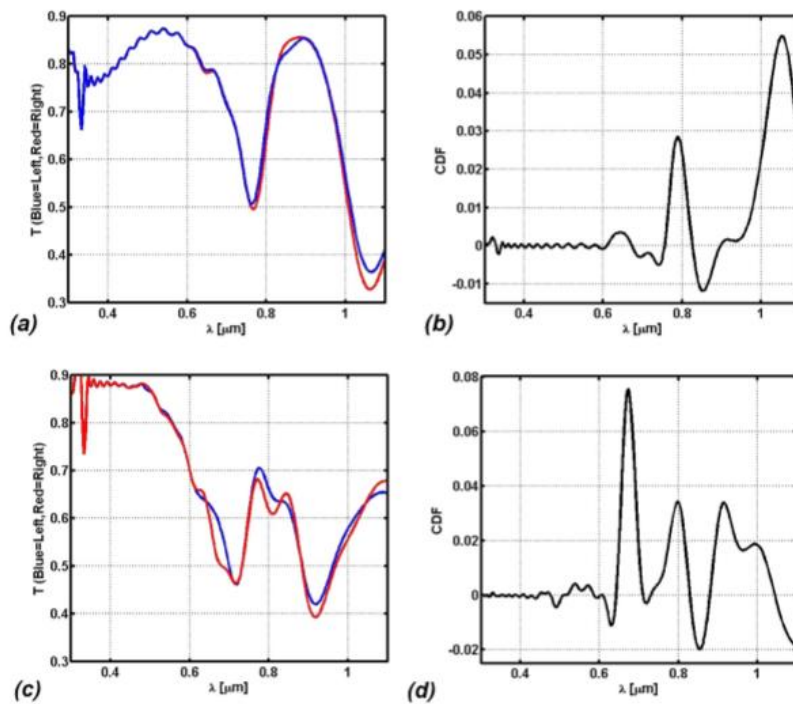


Figure 3.5. (a) Transmission spectra and (b) corresponding CDF at $\lambda = 800\text{nm}$ for the Au -(10° , 14°) and (c) and (d) for Ag -(20° , 20°) configurations, respectively. Due to the direct link of the dichroic effect to the presence of SPPs, the CDF is negligible for wavelengths below 600nm and 480nm for the gold and silver nano-resonator, respectively. For Au -(10° , 14°), we found another peak at 1045nm showing a CDF value of 0.055; and for Ag -(20° , 20°), a narrow peak around 673nm appears, with a CDF approximately equal to 0.076.

The calculated values are in agreement with the experimental results reported in Ref. 22, showing that the fast construction technique related with this work allows to get metamaterials with high CDF. Although being powerful, some other techniques, such as the ones in Refs. 27 and 30, appear to be more promising for their higher recorded CDF values. In particular, the authors of Ref. 30 reported maximal CDF values around 0.7–0.8, which are one order of magnitude higher than those shown in Fig. 3.5. Anyway the authors adopted an electron-beam lithography technique which despite being accurate implies the serial design of each elementary unit and consequently long construction times. Having a self-assembly process at the core, the technique presented in Ref. 22 appears to be less effective but potentially more convenient in terms of time and costs of laboratory equipment.

The particular shape acquired by the nano-resonator introduce also a linear dichroism, i.e., anisotropy, which makes the transmittance a function of the polarization angle. To investigate the anisotropic character of the meta-surface and to conclude the analysis of their transmission properties in order to get a more complete phenomenological description of the device, we choose to numerically evaluate the transmission spectra for the linear polarizations, assuming that the electric field lays either orthogonal or parallel to the direction in the O_{xy} plane determined by Φ . We defined a LDF as follows:

$$LDF(\Phi, \Theta) = \frac{I_{\perp}(\Phi, \Theta) - I_{\parallel}(\Phi, \Theta)}{I_{\perp}(\Phi, \Theta) + I_{\parallel}(\Phi, \Theta)} \quad (3.4)$$

where I_{\perp} and I_{\parallel} are the output intensities of impinging waves at a given wavelength having the linearly polarization senses as explained above.

We report our main results in Fig. 3.6 for Φ ranging from 0° to 30° with a step of 5° , and Θ ranging from 5° to 20° with the same step. The LDF profile are provided both for gold and silver meta-surfaces. Due to the different spectral range for SPPs in metals, we restricted our investigation to the (600–1100) nm and (400–1100) nm range for gold and silver, respectively. Each angular configuration provides the nano-resonators with a different shape and consequently with different effective lengths along the two orthogonal directions upon indicated. The effective lengths affect the resonant wavelengths of the nano-antennas, and this produces a different transmittance for the orthogonal linear polarization. We report the numerical results in Fig. 3.6.

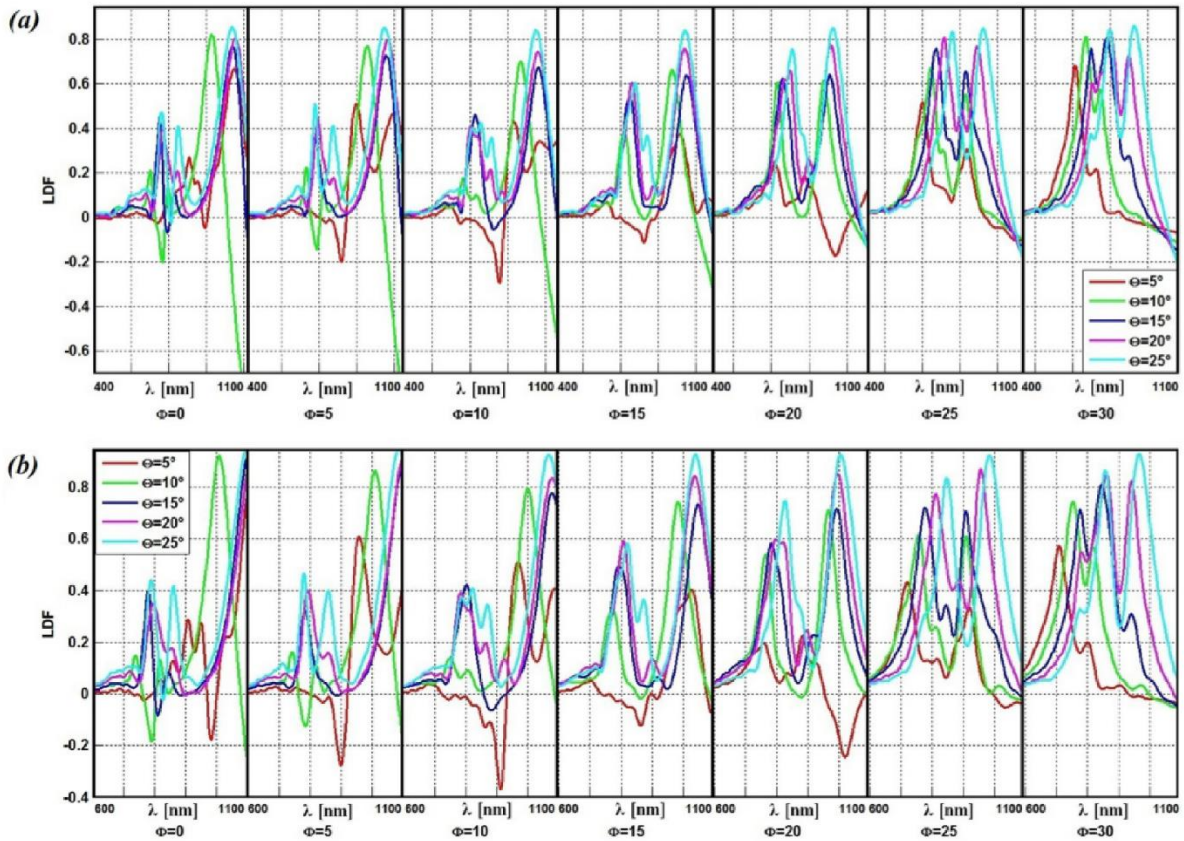


Figure 3.6. (a) Gold and (b) silver LDFs for several angular values of the metal vapor flux. Each window contains 4 plots, related to different θ values as described by the legend. ϕ ranges from 0° to 30° with a step of 5° . LDF covers almost its possible codomain ($[-1,1]$) and is generally stronger in comparison with the corresponding CDF's values.

The registered LDF values for both metals are generally one order of magnitude higher and their spectral profiles are smoother than those corresponding to the CDF. These features reveal that these meta-surfaces are more promising as linear than as circular polarizers.

3.4. - Conclusions.

We studied the transmission properties of meta-surfaces realized by a new self-assembling technique based on the deposition of a metal vapor flux upon polystyrene spheres, and we tested different geometries produced by changing the flux deposition parameters. By changing the flux direction, it is possible to easily obtain controlled achiral or chiral asymmetric nano-resonators acting like antennas in the visible and near infrared frequencies. The obtained 2D distributions can be actually considered as a homogeneous resonant meta-surface. The electromagnetic field distribution along the structure has been calculated to retrieve the spectroscopic aspect of several geometries. We analyzed the transmission properties both for linear and circular polarization of the

impinging wave. We also provided a brief evaluation of the general dichroism in the structures under investigation by defining two important parameters, the LDF and CDF, respectively. We obtained a 2D profile for the CDF at the specific wavelength of 800nm and we similarly gave a representation of the LDF for the same set of 3D angles. We predict that those kind of promising self-assembled and low cost 2D meta-material can be adopted to produce efficient and versatile dichroic filters, such as circular polarizers and optical rotators for the visible light and near infrared frequencies.

3.5. - References.

- [1] F. J. Boehm. “Nanomedical Device and Systems Design: Challenges, Possibilities”, Visions (CRC Press, 2013).
- [2] M. Wilson, Et al. “Nanotechnology: Basic Science and Emerging Technologies” (Taylor & Francis, 2002).
- [3] N. Melosh, Et al. “Ultrahigh-density nanowire lattices and circuits,” *Science* 300(5616), 112–115 (2003).
- [4] S. Das, Et al. “Designs for ultra-tiny, special-purpose nanoelectronic circuits,” *Trans. Circ. Syst.-1* 54(11), 2528–2540 (2007).
- [5] J. E. Hughes, Et al. “Introduction to nanoscale science and technology,” in *Nanostructure Science and Technology* (Springer, 2004).
- [6] Ye. Tao and C. Degen, “Facile fabrication of single-crystal-diamond nanostructures with ultrahigh aspect ratio,” *Adv. Mater.* 25, 3962–3967 (2013).
- [7] M. Kadic, Et al. “Metamaterials beyond electromagnetism,” *Rep. Prog. Phys.* 76, 126501 (2013).
- [8] I. Grigorenko, Et al. “Optimal control of electromagnetic field using metallic nanoclusters,” *New J. Phys.* 10, 043017 (2008).
- [9] P. Gay-Balmaz and O. J. F. Martin, “Electromagnetic resonances in individual and coupled split-ring resonators,” *J. Appl. Phys.* 92(5), 2929–2936 (2002).
- [10] A. Christ, Et al. “Near-field induced tunability of surface plasmon polaritons in composite metallic nanostructures,” *J. Microsc.* 229, 344–353 (2008).
- [11] A. Benedetti, Et al. “Engineering the second harmonic generation pattern from coupled gold nanowires,” *J. Opt. Soc. Am. B* 27(3), 408–416 (2010).
- [12] A. Benedetti, Et al. “Second harmonic generation from 3D nanoantennas: On the surface and bulk contributions by far-field pattern analysis,” *Opt. Express* 19(27), 26752–26767 (2011).

- [13] A. Parviz, Et al. “Using self-assembly for the fabrication of nano-scale electronic and photonic devices,” *IEEE Trans. Adv. Packag.* 26(3), 233–341 (2003).
- [14] C. Caloz and T. Itoh. “Electromagnetic Metamaterials: Transmission Line Theory and Microwave Applications” (Wiley-IEEE Press, 2005).
- [15] M. Hawkes, Et al. “A microwave metamaterial with integrated power harvesting functionality,” *Appl. Phys. Lett.* 103, 163901 (2013).
- [16] H. T. Chen, Et al. “Active terahertz metamaterial devices,” *Nature* 444, 597–600 (2006).
- [17] W. Withayachumnankul and D. Abbott. “Metamaterials in the terahertz regime,” 1(2), 99–118 (2009).
- [18] G. Dolling, Et al. “Negative-index metamaterial at 780nm wavelength,” *Opt. Lett.* 32(1), 53–55 (2007).
- [19] W. Cai and V. Shalaev. “Optical Metamaterials-Fundamentals and Applications” (Springer, 2010).
- [20] V. Robbiano, Et al. “Hybrid plasmonic–photonic nanostructures: gold nanocrescents over opals,” *Adv. Opt. Mater.* 1, 389 (2013).
- [21] A. Belardini, Et al. *Proc. SPIE* 8772, 877203 (2013).
- [22] A. Belardini, Et al. “Second harmonic generation circular dichroism from self-ordered hybrid plasmonic–photonic nanosurfaces,” *Adv. Opt. Mater.* 2(2), 208–213 (2014).
- [23] V. K. Valev, Et al. “Chirality and chiroptical effects in plasmonic nanostructures: Fundamentals, recent progress, and outlook,” *Adv. Mater.* 25, 2517–2534 (2013).
- [24] M. Esposito, Et al. “Three dimensional three dimensional chiral metamaterial nanospirals in the visible range by vertically compensated focused ion beam induced-deposition,” *Adv. Opt. Mater.* 2(2), 154–161 (2014).
- [25] J. K. Gansell, Et al. “Gold helix photonic metamaterial as broadband circular polarizer,” *Science* 325(5947), 1513–1515 (2009).
- [26] T. Verbiest, Et al. “Light-polarization-induced optical activity,” *Phys. Rev. Lett.* 82(18), 3601 (1999).
- [27] M. Kuwata-Gonokami, Et al. “Giant optical activity in quasi-two dimensional planar nanostructures,” *Phys. Rev. Lett.* 95, 227401 (2005).
- [28] E. Plum, Et al. “Metamaterials: optical activity without chirality,” *Phys. Rev. Lett.* 102, 113902 (2009).

- [29] A. Belardini, Et al. “Circular dichroism in the optical second-harmonic emission of curved gold metal nanowires,” *Phys. Rev. Lett.* 107(25), 257401 (2011).
- [30] K. Konishi, Et al. “Circularly polarized light emission from semiconductor planar chiral nanostructures,” *Phys. Rev. Lett.* 106, 057402 (2011).
- [31] A. A. Maksimov, Et al. “Circularly polarized light emission from chiral spatially structured planar semiconductor microcavities,” *Phys. Rev. B* 89, 045316 (2014).
- [32] A. Balanis. “Antenna Theory Analysis and Design”, 3rd ed. (John Wiley & Sons, 2005).
- [33] EE Std 149-1979 (R2008), “IEEE Standard Test Procedures for Antennas”. Approved 15-12-1977, Reaffirmed 10-12-2008, IEEE-SA Standards Board. Approved 9-10-2003, American National Standards Institute, ISBN 0-471-08032-2, doi:10.1109/IEEESTD.1979.120310, Sec. 11.1, p. 61.
- [34] D. Palik, *Handbook of Optical Constants of Solids* (Elsevier, 1997).

Chapter 4. – Numerical Evaluation of Irradiation Diagram by Plasmonic Grating and Slit Apertures.

4.1 - Introduction.

Surface plasmon polaritons (SPPs) are transverse-magnetic polarized bounded electromagnetic modes that propagate along the interface between a dielectric and a metal [1, 2], being confined at the interface by the exponential decay of the fields in the directions perpendicular to the interface. The field confinement and manipulation at subwavelength scale achievable with SPPs holds promise for enabling dramatic miniaturization of the sizes of optical filters and sensors [3 - 5].

The incidence of a plasmon across surface defects has been intensively studied, and several models have been adopted for the spatial description of the near and far field. Radiative scattering, together with plasmonic reflection and transmission phenomena in surface defects in metal films, has been widely investigated by means of numerical methods [6 - 9] and experimental techniques [10 - 12]. In particular cases, the adoption of approximated analytical models [13] has also been applied to calculate the far-field irradiation diagram (ID) [14]. Moreover, nowadays the combination of surface defects into plasmonic gratings (PGs) [15 - 20] has seen increased interest due to its high localization effects [21 - 23] and the possibility to improve the efficiency of coupling electromagnetic waves in optical circuits and devices [24 - 26].

Feeding plasmonic gratings is possible either by direct light illumination or by the use of subwavelength slit apertures carved on the same metal layer [27 - 31]. These latter devices have seen renewed interest for their ability to exhibit relatively high transmission levels [32 - 34] and strong output coherence by means of supported Fabry–Perot-like modes for light polarized perpendicular to the slit. Their output emission can be increased in power and directivity by patterning the output faces and taking advantage of the surface defects' ability to convert plasmonic fields into radiated waves; thus, the combination of plasmonic gratings and slit apertures completes the coupling mechanism and allows the transmitted field pattern to acquire interesting features. The coupling with the impinging wave can be further increased by also patterning the input face [18], but this topic is beyond the scope of this chapter. Here, we present a way to calculate the irradiation diagram of a generic planar structure composed of a set of slit apertures and plasmonic gratings without the need for full bidimensional (2D) simulations. It proceeds by the ideal decomposition of the system into a linear array of discrete basic cells and the subsequent recombination of their scattered complex profiles, indicated with ψ . This combining procedure requires the adoption of a complete set of information about the electromagnetic properties of all the scatterers compounding this system. The investigation of periodic dispositions of symmetric scatterers has been already treated in the literature, and expanded also for three-dimensional (3D) arrays [17]. Here, we utilize this model analyzing generic 2D distributions of scatterers presenting generally different behavior when a SPP impinges at the two opposite sides. This procedure can be extended either to periodic disposition of regular surface defects or to more complex configurations involving more slit

apertures. Although suffering from some limitations, this model turns out to be useful in many cases and allows us to estimate a large series of grating configurations in a very short amount of time and without the need for powerful hardware systems. In Section 2 of the present chapter, we describe the basic steps of the adopted numerical procedure; then in Section 3, we present some explicative examples of scattering both from simple gratings illuminated by a test SPP and from a system composed by a combination of a slit aperture with two side gratings illuminated by a plane wave from below the metal layer. A discussion about the limitations of this model is reported. Finally, in Section 4, the main conclusions are drawn.

4.2. - Numerical scheme.

The presented numerical procedure requires a collection of data retrieved by studying the behavior of the single compounding elements of the gratings, comprising both the complex irradiation diagram related to a unitary test SPP and the coefficients of plasmonic reflection and transmission. Many ways are adoptable for the latter of these calculations, but they are beyond the goal of this chapter.

A slit aperture illuminated by an optical beam from the input interface will be the primary source of radiation, and the excited SPP leaving the slit's output corners, together with the ones excited afterward, will undergo multiple reflections between the scatterers [19]. At each interaction, a portion of the plasmonic field will be converted into a radiated field. The totally scattered field by a surface defect will depend on the SPPs impinging at the two opposite sides, and the summation of the scattered fields by all the surface defects will define the total ID.

Before investigating the behavior of the entire slit aperture grating system, we study the radiating and plasmonic properties of a simpler collection of scatterers as shown in Fig. 4.1.

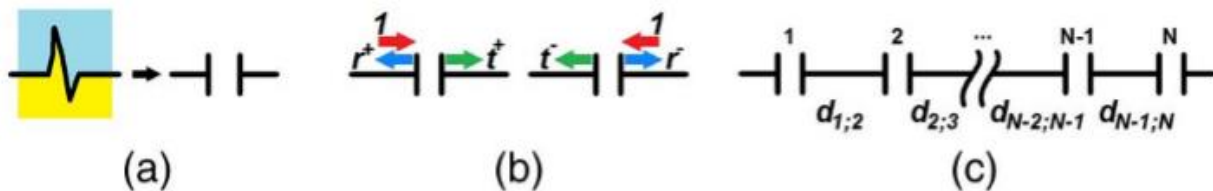


Figure 4.1. (a) Surface defects indistinctly modeled as scatterers. Their spatial limits coincide with the closest point belonging to the regular metal–dielectric interface. (b) Incident (red) test SPP, with reflected (blue) and transmitted (green) SPPs. \pm sign refers to the case of incidence from the left/right side, respectively. (c) Ensemble of N scatterers with reciprocal distances.

Indicating with $+$ and $-$ the coefficients referring to the SPP's incidence from the left and right side, respectively, we evaluate the total reflection and transmission plasmonic coefficients of N aligned scatterers by the multiple reflections theory [35]:

$$\begin{aligned}
T_{(i+1)}^{\pm} &= \frac{T_{(i+1)}^{\pm} t_{i+1}^{\pm} e^{+i\beta d_{i,i+1}}}{1 - R_{(i)}^{-} r_{i+1}^{\pm} e^{+i2\beta d_{i,i+1}}} \\
R_{(i+1)}^{+} &= R_{(i)}^{+} + \frac{r_{i+1}^{+} T_{(i)}^{+} T_{(i)}^{-} e^{+i2\beta d_{i,i+1}}}{1 - R_{(i)}^{-} r_{i+1}^{\pm} e^{+i2\beta d_{i,i+1}}} \\
R_{(i+1)}^{-} &= r_{i+1}^{-} + \frac{R_{(i)}^{-} t_i^{\pm} t_i^{-} e^{+i2\beta d_{i,i+1}}}{1 - R_{(i)}^{-} r_{i+1}^{\pm} e^{+i2\beta d_{i,i+1}}}
\end{aligned} \tag{4.1a}$$

with β being the plasmonic wave number of the metal–dielectric interface, $d_{i;i+1}$ being the mutual distances between contiguous scatterers as shown in Fig. 4.1(c), and assuming the starting and final conditions:

$$T_{(1)}^{\pm} = t_1^{\pm}, \quad R_{(1)}^{\pm} = r_1^{\pm}, \quad T_{Tot}^{\pm} = t_N^{\pm}, \quad R_{Tot}^{\pm} = R_N^{\pm} \tag{4.1b}$$

The coefficients are thus calculated after $N - 1$ iterations. The full description of the totally radiated field requires the calculation of the impinging SPPs at both sides for each scatterer. Looking at Fig. 4.2(a), the impinging plasmons are:

$$\begin{aligned}
p_{k,L} &= P_0 \cdot \frac{T_{Lk}^{+} e^{+i\beta d_{k,L}}}{1 - R_{Lk}^{-} \left(r_k^{+} + \frac{t_k^{+} t_k^{-} R_{Rk}^{+} e^{+i2\beta d_{k,R}}}{1 - R_{Rk}^{+} r_k^{-} e^{+i2\beta d_{k,R}}} \right) e^{+i2\beta d_{k,L}}} \\
p_{k,R} &= P_0 \cdot \frac{t_k^{+} T_{Lk}^{+} R_{Rk}^{+} e^{+i\beta(2d_{k,L} + d_{k,L})}}{1 - r_k^{+} R_{Lk}^{-} e^{+i2\beta d_{k,L}} - \left[r_k^{-} + (t_k^{+} t_k^{-} - r_k^{+} r_k^{-}) R_{Lk}^{-} e^{+i2\beta d_{k,L}} \right] R_{Rk}^{+} e^{+i2\beta d_{k,R}}}
\end{aligned} \tag{4.2}$$

with the suffixes L and R referring to the left and right subblocks, respectively; the + and – signs referring to impingement from the left or right side, respectively; P_0 being the complex envelope of the incident SPP on the leftmost scatterer; and T_{Lk} and R_{Lk} representing the transmission and reflection coefficients, respectively, of the two subblocks flanking the k_{th} element and calculated exactly as done in Eq. (2) for the entire series.

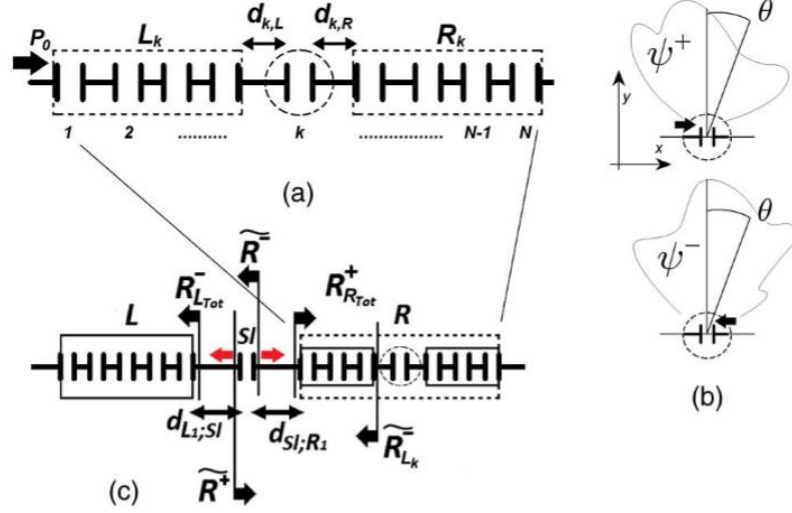


Figure 4.2. (a) Schematic view of the physical interpretation for the SPP propagation in metal gratings: a test SPP (p_0) impinges on a grating from the left side. The k th scatterer receives a portion of the beginning SPP after many internal reflections. After infinite multiple reflections, the total plasmonic field incident across the k th surface defect will be represented by two SPPs impinging a top positive sides. To know the ID, one must know the irradiation diagram of the surface defect under plasmonic incidence, as shown in (b). In (c), a larger scheme including a slit aperture and another grating is designed opposite to the first one. Each arrow cutting the line of scatterers refers to the plasmonic reflectivity of the entire system as seen from that position, and for a test SPP directed as the arrow indicates. The small red arrows represent $p_{0,R}$ and $p_{0,L}$.

For the leftmost (rightmost) scatterer, $R_{L,k}^\pm (R_{R,k}^\pm)$, $T_{L,k}^\pm (T_{R,k}^\pm)$, and $d_{k,L} (d_{k,R})$ equal 0, 1, and 0, respectively, and for incidence from the right side, the expressions in Eq. (4.2) keep valid by replacing the index L with R and vice versa. Finally, according to the symmetry conditions, the scattering element will radiate as:

$$\psi_k(\theta) = \begin{cases} p_{k,L} \cdot \psi_k^+(\theta) + p_{k,R} \cdot \psi_k^-(\theta) & \text{Asymmetric} \\ p_{k,L} \cdot \psi(\theta) + p_{k,R} \cdot \psi(-\theta) & \text{Symmetric} \end{cases} \quad (4.3)$$

with \pm referring again to the side of incidence, as shown in Fig. 4.2(b), and ψ being the scatterer's complex irradiation profile as a function of the angle θ , which is linked to the magnetic field H (which lies in z) as follows:

$$\psi_k(\theta) = H_z(\rho, \theta) \sqrt{\frac{50\rho}{2}} \quad (4.4)$$

The radial distance ρ is the one chosen to retrieve the H field profile. The angular function ψ in Eq. (4.4) is complex and independent on the average radial distance from the scatterer. This happens for lossless backgrounds, so that the total irradiated power is a conserved quantity with increasing distance from the emission point. A slit aperture flanked by two gratings in the output face will radiate the output half-space both directly as the primary emitter and by the SPPs leaving its output shoulders, which will promote scattered field by interacting with the surrounding gratings. We thus can model the entire system as a more complex collection of surface defects and sources. Looking at Fig. 4.2(c), where $R_{L,Tot}^-$ and $R_{R,Tot}^+$ refer to the reflectivity of the left and

right blocks, respectively, seen by the slit aperture and with $\rho_{0,R}(\rho_{0,L})$ being the complex envelope of the excited SPPs (as reported to the corner points and $y = 0$) propagating toward the right (left) in the absence of any surrounding defect, after some algebra we calculate the total SPPs impinging on the slit:

$$p_{Sl,R/L} = \left(p_{0,R/L} + p_{0,L/R} \frac{t_{Sl}^{\pm} R_{L/R,Tot}^{\pm} e^{+i2\beta d_{L/R}}}{1 - r_{Sl}^{\pm} R_{L/R,Tot}^{\pm} e^{+i2\beta d_{L/R}}} \right) \cdot \frac{R_{L/R,Tot}^{\mp} e^{+i2\beta d_{R/L}}}{1 - r_{Sl}^{\mp} R_{L/R,Tot}^{\mp} e^{+i2\beta d_{R/L}}} \quad (4.5)$$

The presence of the slit and one of the gratings complicates the calculation for the impinging plasmons across the scatterers of the other grating. Anyways, to calculate the plasmonic incidence across the right set of scatterers, it is still sufficient to reconsider the definitions in Eq. (4.2) and performing the following substitutions:

$$P_0 \rightarrow \widetilde{P}_{0,k} = \frac{p_{0,R} + p_{0,L} \frac{t_{Sl}^+ R_{L,Tot}^- e^{+i2\beta d_{L1,Sl}}}{1 - r_{Sl}^+ R_{L,Tot}^- e^{+i2\beta d_{L1,Sl}}}}{1 - R_{L,k}^+ \widetilde{R}^- e^{+i2\beta d_{Sl,R1}}} e^{+i\beta d_{Sl,R1}}$$

$$R_{Lk}^- \rightarrow \widetilde{R}_{Lk}^- = R_{Lk}^- + \frac{T_{Lk}^- T_{Lk}^+ \widetilde{R}^- e^{+i\beta d_{Sl,R1}}}{1 - \widetilde{R}^- R_{Lk}^+ r_{i+1}^+ e^{+i2\beta d_{Sl,R1}}} \quad (4.6a)$$

For the definitions in Eq. (4.6a), we further defined:

$$\widetilde{R}^- = r_{Sl}^- + \frac{t_{Sl}^+ t_{Sl}^- R_{L,Tot}^- e^{+i2\beta d_{L1,Sl}}}{1 - R_{L,Tot}^- r_{Sl}^+ e^{+i2\beta d_{L1,Sl}}} \quad (4.6b)$$

with the meaning of the involved parameters explained in Fig. 4.2(c). A perfectly similar procedure is adopted for the left set of scatterers, but we omit further details for the sake of simplicity. In the end, the system composed by the slit aperture and the two side gratings will radiate a total field:

$$\psi_k(\theta) = \psi_0(\theta) + \sum_{K=1}^S [p_{k,L} \cdot \psi_K^+(\theta) + p_{k,R} \cdot \psi_K^-(\theta)] e^{-ik_0 x_k \cos(\theta)} \quad (4.7)$$

where S refers to the total number of scatterers, including both the surface defects and the slit aperture, and ψ_0 is the magnetic field directly emitted by the slit as a plasmonic channel illuminated from the input face. The final ID is calculated as the square modulus of ψ , such that:

$$\int_{-\frac{\pi}{2}}^{+\frac{\pi}{2}} |\psi_{Tot}(\theta)|^2 d\theta = \int_{-\frac{\pi}{2}}^{+\frac{\pi}{2}} ID(\theta) d\theta = W \quad (4.8)$$

with W being the power per unit length flowing away and crossing a half-circle surrounding the scattering element.

A strong similarity of the investigated electromagnetic systems with multilayered media crossed by plane waves could suggest the adoption of a matrix formalism. This can be applied when the continuity conditions for tangential field

components directly link the complex envelopes of counter propagating waves in opposite sides at the interfaces connecting contiguous layers. This cannot be applied in the systems under investigation, because the plasmonic coefficients related to a generic scatterer cannot be evaluated neglecting the contribution of the other scatterers.

The algorithm can be further generalized for a collection of scatterers and multiple slit apertures by invoking the superposition principle for linear systems, and provided that all the surface defects are located at the same y level. It must be applied a number of times equal to the number of scatterers, each time turning all the slit apertures off with the exception of just one, which will still be assumed as the primary optical scatterer, and then calculating the far-field complex envelope of the H field. Finally, after many iterations, each one focused around a certain slit aperture, the total ID is calculated as the square modulus of the total summation of all the partial H fields.

4.3. - Some examples.

We start by testing our model with a grating composed by a series of grooves of equal width (150nm) but different thickness, derived on a gold [36] substrate and illuminated from the left side by a test SPP with a vacuum wavelength $\lambda = 632 \text{ nm}$. The choice of this wavelength will be implicitly set also for the next examples, and it lays on the desire of having long range SPPs also in presence of surface defects to take advantage of large gratings, which would be impossible at longer wavelengths in gold such as 800 nm, where the strong localization due to the high permittivity value would lead to high irradiative scattering across the first encountered surface defect and the immediate extinction of the SPP. We have fully taken into account absorption in the metal, both for the calculation of the plasmonic coefficients of the scatterers and for the SPP free propagation along the flat metal–dielectric interface, since the calculated value of the wavenumber β is complex (the normalized β value for the air/gold smooth interface at $\lambda = 632 \text{ nm}$ is $1.0536 + i*0.0119$). Losses are evidenced by the absorption spectra of Fig. 4.3, and by the imaginary part for β , whose presence and effects can also be observed by inspecting Fig. 4.4, where the incident, reflected, and transmitted SPPs show reduced amplitude along the spatial propagation.

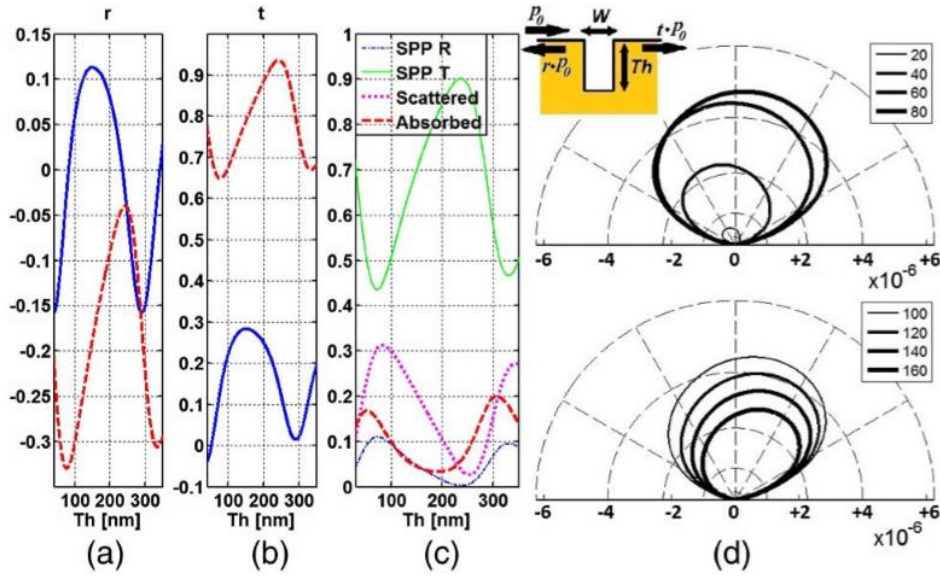


Figure 4.3. (a) Plasmonic reflection and (b) transmission coefficients for a groove scatterer in a vacuum–Au interface at $\lambda = 632 \text{ nm}$, as a function of the Th . Straight (dashed) lines refer to real (imaginary) parts. (c) Plasmonic reflectance and transmittance, scattered power, and local absorption. This last term includes also the evanescent component of the excited plasmons. (d) ID around the surface defects for some thickness values. The ID is associated with an impinging SPP of unitary amplitude at the air/gold interface level.

In Figs. 4.3(a) and 4.3(b), the plots of the plasmonic reflection and transmission coefficients in their real and imaginary parts as a function of the vertical thickness are shown, together with the scattered magnetic field diagram for some configurations in Fig. 4.3(d). In Fig. 4.3(c), we superposed the parametric functions of plasmonic reflectance and transmittance with the locally absorbed and total scattered powers. Conservation of power requires

$$1 = |r|^2 + |t|^2 + \frac{1}{P_I} \int_{\pi} ID(\theta) d\theta + A \quad (4.9)$$

Where A refers to the absorbed fraction of incident power, and the third term at the right-hand side is the scattered fraction. P_I refers to the power per unit length inserted into the scatterer by a unitary SPP, i.e., a plasmon whose envelope is 1 at ground level ($y = 0$), and is

$$P_I = \frac{1}{4\omega\epsilon_0} \left[\frac{\text{Re}(\beta/\epsilon_{r,b})}{\text{Re}(a_b)} + \frac{\text{Re}(\beta/\epsilon_{r,m})}{\text{Re}(a_m)} \right]$$

$$a_{b/m} = \sqrt{\beta^2 - k_0^2 \epsilon_{r,b/m}} \quad (4.10)$$

The absorbed fraction includes also the transitory components of the excited plasmons. Indeed, due to the high field localization, the scatterers give rise to additional field components close to their physical extension which do not undergo long-distance propagation, but strongly affect the plasmonic multiple reflections and consequently

the overall scattering process. Consequently, the presented procedure loses reliability for configurations with scatterers closer than the vacuum wavelength.

To evaluate the effect of close proximity of the scatterers, we plotted in Fig. 4.4 the plasmonic coefficients both as calculated by the discussed theory and by COMSOL Multiphysics for a couple of identical grooves in a gold substrate. The surrounding background is air/vacuum, and the grooves' width and thickness are both 200 nm. The plot shows explicitly a noticeable difference between calculated values by 2D simulations and by the proposed method, when the distance between scatterers is reduced below the plasmonic length of approximately 598 nm. These differences affect the ID calculation for grating configurations featuring scatterers which are too close to each other.

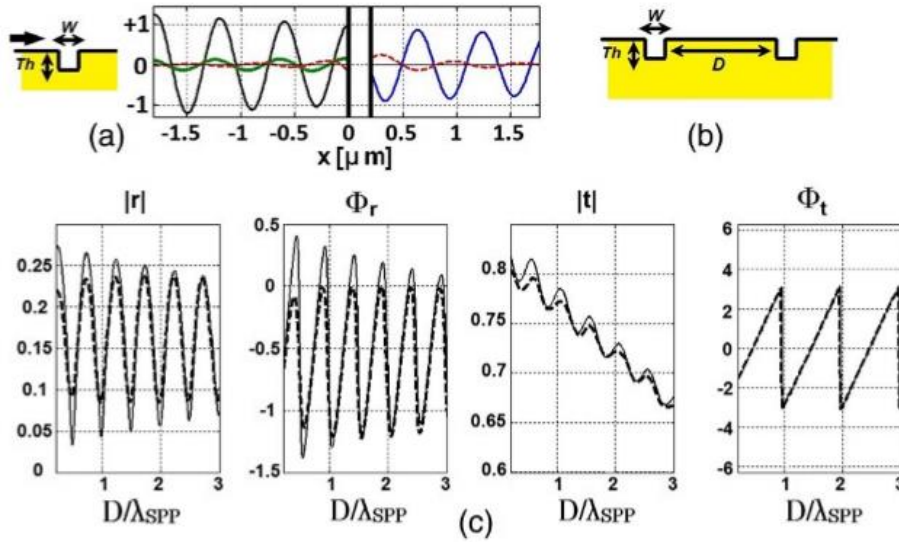


Figure 4.4. (a) Real part of SPP envelopes at $y = 0$ for a scattering groove (gold in vacuum) at $\lambda = 632 \text{ nm}$. W and Th are both 200nm. The input SPP impinges from left side. Black, green, and blue straight lines refer to the incident, reflected, and transmitted SPP, respectively. Dashed red lines refer to transitory fields. The plasmonic coefficients are $r = 0.152e^{-i0.484}$ and $t = 0.911e^{+i1.697}$. (b) Configuration with a double set of identical scatterers divided by a flat region of length D . (c) Coefficient r (t) in norm and phase as a function of the normalized distance D with respect to the plasmonic wavelength ($\sim 598 \text{ nm}$). Dashed profiles are calculated under COMSOL Multiphysics, while straight lines are calculated following Eqs. (4.1).

In Fig. 4.5, we show the results of the recombination method applied to two gratings, each composed of seven scatterers belonging to the surface defects class of Fig. 4.3, and impinged by a SPP from the left side. The figure reports also a depiction of the plasmonic gratings and two tables with the complex value of the SPPs impinging from both sides across each scatterer in terms of norm and phase. A superposition of plots shows the IDs both as calculated by the recombination method and by commercial simulation software. For this latter task, we adopted COMSOL Multiphysics Version 3.5. As described by Eqs. (4.1) – (4.2), we calculated the following values for the SPPs impinging from left and right sides across each scattering

element, and summated all the partial scattered H fields to get the total one, from which the entire system ID has been calculated by means of Eq. (4.7).

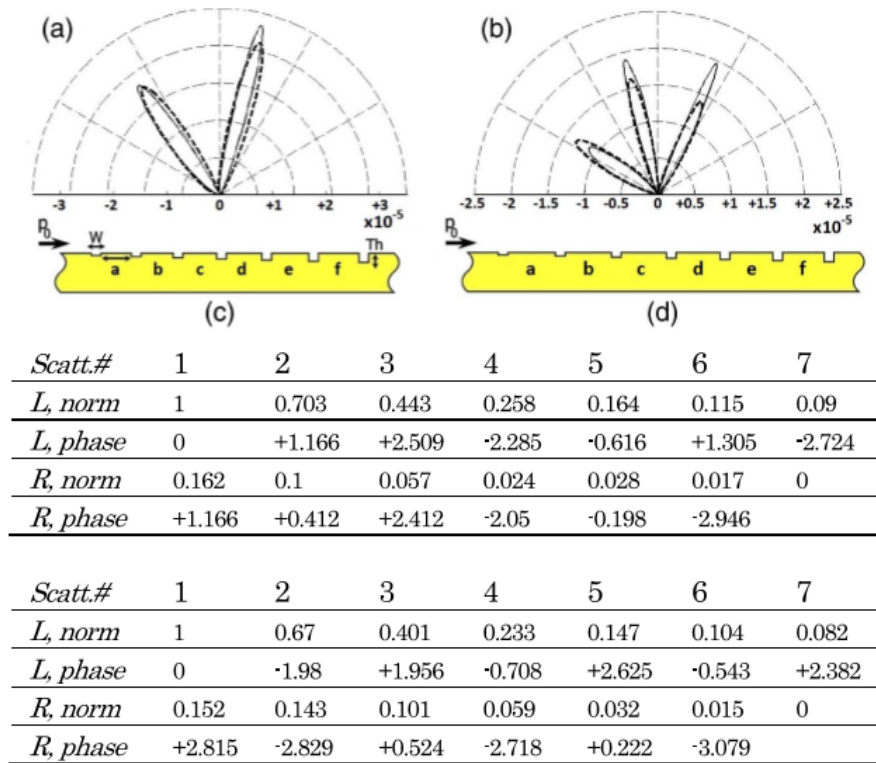


Figure 4.5. (a–b) IDs of two gold PGs in air, displayed in panels c and d, respectively, and composed of seven scatterers and impinged by a test SPP ($\lambda = 632 \text{ nm}$) from the left side. $W = 150 \text{ nm}$ commonly for all the scatterers. Th has a minimal value of 40 nm for the leftmost scatterer, growing by 20 nm after each subsequent scatterer for both gratings. Straight (dashed) lines refer to polar plots as calculated by the presented algorithm (COMSOL). For the PG in panel c (d), a; b;...;f assume values from 550 (850) nm to 700 (650) nm with a step of 30 (20) nm . Two tables display the calculated complex values of the impinging SPPs across each of the seven scatterers from the left (L) and right (R) sides.

As done in Fig. 4.5, the relative geometric description of the grating, together with its IDs and the values of the impinging SPPs across each scatterer, is enclosed in Fig. 4.7.

The importance of considering two distinct values for the plasmonic coefficients as a function of the SPP's provenience is witnessed by the presence of ID differences for the two grating variants. Indeed, both grating types show two main emission peaks roughly oriented toward 77° and 124° , with the one at 77° being the stronger for the grating type in (a) and the weaker for the grating type in (b).

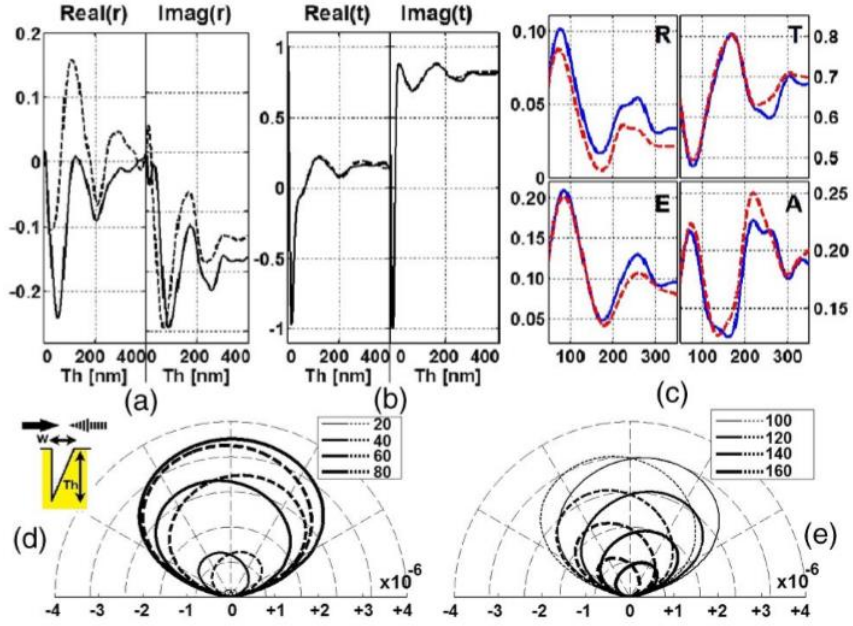


Figure 4.6. Plasmonic coefficients r (a) and t (b) as a function of Th (see inset) ($\lambda = 632$ nm in air/gold interface) for the scatterer class in the small inset. Straight (dashed) lines refer to plasmonic incidence from left (right) side. W value is fixed at 150 nm. The scatterer is nonsymmetric and triangular. (c) Plasmonic reflectance (R), transmittance (T), total scattered power ratio (E), and absorption ratio (A) as a function of Th . In (d) and (e), IDs of several surface defects of the same class are shown. The adopted convention for the lines is the same as for (c). Note that, due to the asymmetric nature of the scatterer, ψ_+ and ψ_- are not simply mirrored distributions.

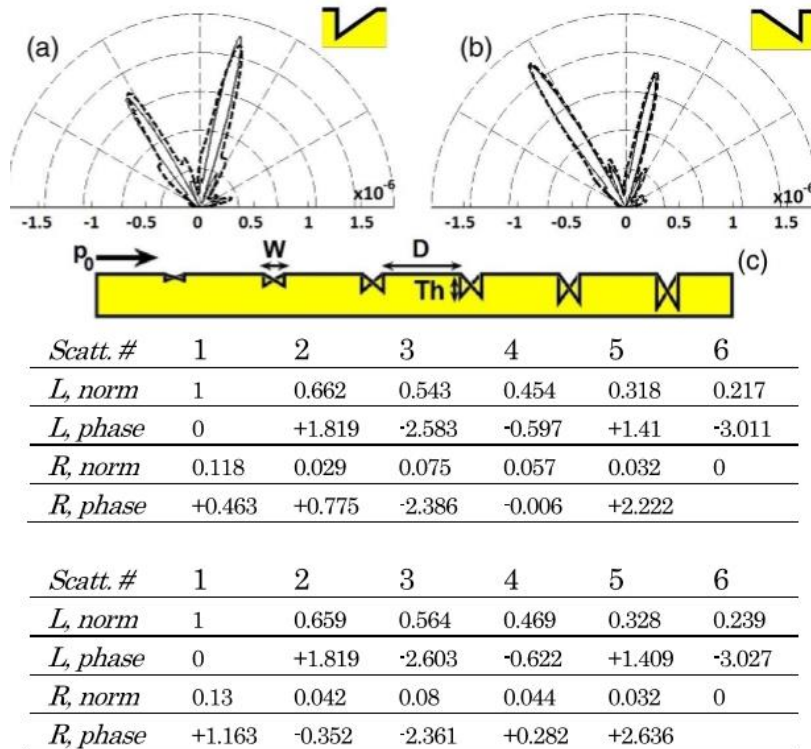


Figure 4.7. Plots for a PG in an Au layer composed of six asymmetric scatterers with impinging SPP from left ($\lambda = 632$ nm). We set $W = 150$ nm and $D = 650$ nm. Th goes from 100 to 300 nm with a step of 40 nm from the leftmost to the rightmost scatterer. In (a) and (b), IDs of scatterers are oriented as shown in the relative insets. Straight (dashed) lines are calculated with the presented algorithm (COMSOL). (d) and (e) include tables with the complex values for the SPPs impinging across the scatterers from both sides for the two grating variants.

Similar effects happen for ridge-based gratings, as shown in Fig. 4.8. In the picture, the IDs of two similar gratings composed by three identical ridge scatterers are shown. PG2 features a mirrored version of the scatterers compounding PG1. Despite the scatterers' subwavelength size ($40 \text{ nm} \times 100 \text{ nm}$), the two total IDs show evident differences, with PG2 featuring a vertical peak of emission which is suppressed in PG1. It is important to point out that, in the case of ridge elements, the choice of small H values in comparison with the vacuum wavelength is somehow mandatory in order to prevent further interactions between fields scattered by each ridge with other ridges close by. In case of high H values, the rising effects of these interactions are not taken into account by this model, and they can strongly modify the final pattern of irradiation.

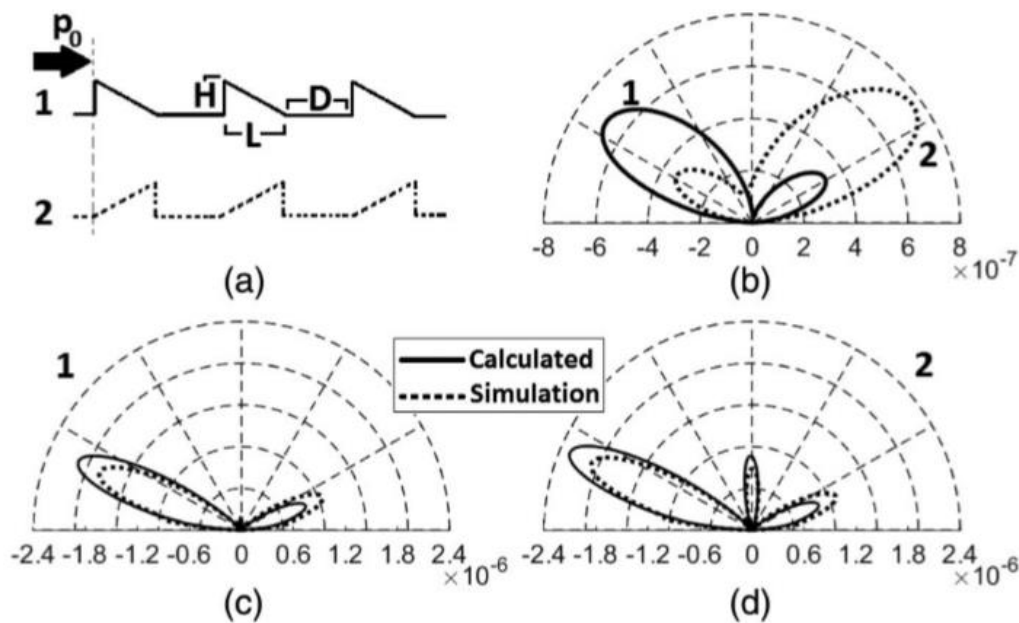


Figure 4.8. (a) Plasmonic grating assembled with three identical ridges (Vacuum–Gold at $\lambda = 632 \text{ nm}$). In the considered examples, $D = 500 \text{ nm}$, $H = 40 \text{ nm}$, and $L = 100 \text{ nm}$. In (a), the test SPP (p_0) impinges from the gratings' left corner on the two PG variants. In (b), the IDs of a single scatterer belonging to PG 1 and 2, respectively, are shown. In (c) and (d), the total PG's IDs are shown, as calculated by the discussed technique (straight line) and as simulated with COMSOL (dashed line). The plasmonic coefficients for the single scatterers of PG1 are $r = 0.231e^{-i0.26}$ and $t = 0.886e^{+i1.199}$, while those of PG2 are $r = 0.238e^{+i0.28}$ and $t = 0.886e^{+i1.198}$.

Finally, the algorithm has been applied to the calculation of the emission pattern of a system composed of two plasmonic gratings flanking a slit aperture. The system is designed in a gold layer upon a glass substrate, whose refractive index has been set to 1.4 and which occupies the input region illuminated by an incoming plane wave [indicated by the central green arrow in Fig. 4.7(c)] having the same wavelength (in vacuum) as the one adopted for the previous examples. As done in the example of Fig. 4.6, we calculated the IDs of two variants, including the respective scatterer type depicted in the respective insets at the upright corners, and we made comparisons with the results of two corresponding 2D simulations performed under COMSOL Multiphysics. The slit aperture is perfectly symmetric and, while acting as a plasmonic

channel fed by the impinging wave from the input side, the slits directly promote two twin SPPs leaving the output corners with a complex envelope as $p_0 = 0.30465e^{-i0.0006}$ in conjunction with a primary emission pattern as shown in Fig. 4.9(a). As a scatterer, it exhibits symmetric plasmonic coefficients as $r = 0.1956e^{-i1.0161}$ and $t = 0.8274e^{+i1.7208}$ and an ID as shown in Fig. 4.7(b). This latter information has been considered, together with the electromagnetic properties of the class of scatterers described in Fig. 4.5, to calculate the IDs of Figs. 4.7(d) and 4.7(e), where a comparison with the output of corresponding COMSOL Multiphysics simulations has proven the good accuracy of our method.

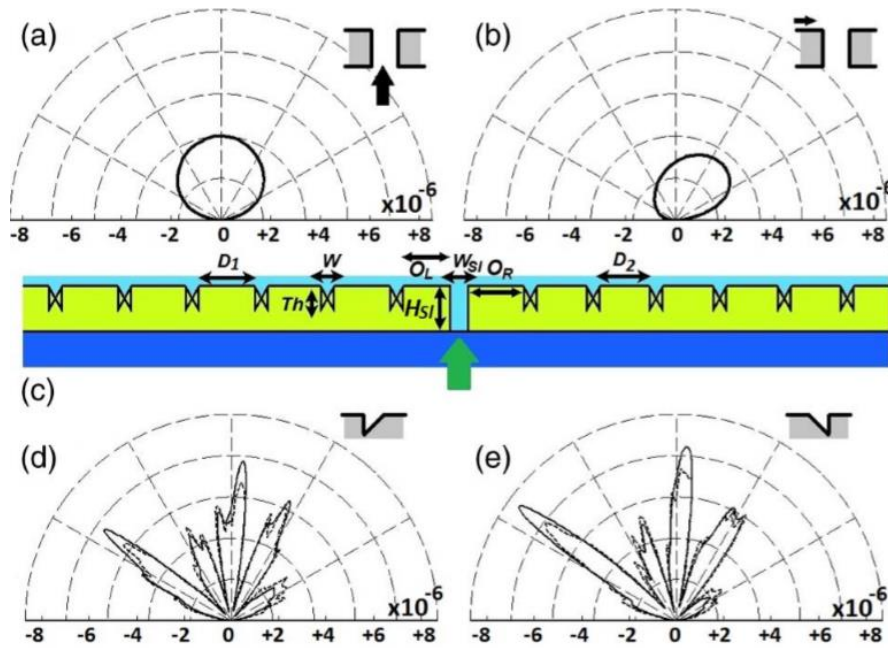


Figure 4.9. ID calculated for a system composed of a slit aperture and two flanking PGs in a gold layer upon a glass substrate ($n = 1.4$), illuminated below the metal layer by a plane wave ($\lambda_0 = 632 \text{ nm}$). The slit aperture $WS1$ is 200 nm , and the thickness $HS1 = 500 \text{ nm}$. After the interaction with the input wave, two twin SPPs are excited at the output corners and propagate parallel to the metal plane, with a complex envelope $p_0 = 0.30465e^{-i0.0006}$. At the same time, the slits scatter toward the output space featuring the ID plotted in (a). This is expressed in arbitrary units (a.u.), since its power depends on the input beam's power. (b) As a surface defect is impinged by a unitary SPP, the slit exhibits $r = 0.1956e^{-i1.0161}$ and $t = 0.8274e^{+i1.7208}$ with the ID shown. In (c), two plasmonic gratings flank the slit aperture with $D_1 = 600 \text{ nm}$, $D_2 = 550 \text{ nm}$, $W = 150 \text{ nm}$, $Th = 100 \text{ nm}$, $O_L = 525 \text{ nm}$, and $O_R = 600 \text{ nm}$. The scatterers belong to the class described in Fig. 4.5 and, when oriented as in the upper-left inset of Fig. 4.5, the ID (a.u.) assumes the profile plotted in (d), while for the opposite variant it assumes the profile plotted in (e). The polar plots in (c–d) have been calculated both by full 2D simulations (dashed lines) and the discussed algorithm (straight line).

The discussed procedure allows fast and accurate estimates of the ID even for a more general disposition of passive surface defects and slit apertures. These slits act as active emitters but also take part in the plasmonic multiple reflections and propagative field rescattering as well. By taking advantage of the superposition effect, it is possible to repeat the just-explained procedure by excluding the primary emission of each slit aperture (thus actually turning it into a simple surface defect) with the exception of

one, and then calculating the partial complex magnetic far-field distribution. The summation of this distribution returns the final ID of the entire optical structure.

This method is versatile also for the selection of appropriate plasmonic configurations in the case of prerequested IDs, because the ID calculation can be performed quickly after an efficient encoding, and several loops of calculations for a large series of gratings become possible provided that a sufficient amount of data containing all the necessary information of the scatterers is available.

4.4. - Conclusions.

We present an efficient method to estimate the 2D irradiation diagram for a linear cluster of various scatterers aligned to form a plasmonic grating and impinged by a SPP. It is general and adapted also to asymmetric surface defects, whose electromagnetic properties generally need a double description in dependence of the provenience side of the test SPP. The method includes a structured algorithm which properly combines the electromagnetic properties of its compounding elements, and the effects of combination with slit apertures have been also discussed. The case of inclusion of several slit apertures in the same structure is straightforward, and the required algorithmic improvement is just the repetition of the basic procedure to several subsystems in number equal to the illuminated slit apertures, each subsystem having been derived from the main one by setting the direct illumination of all the slit apertures off with the exception of one. The superposition of all the scattered and transmitted H fields allows the calculation of the ID for the entire structure. This approach provides excellent correspondence with the ID calculated with full-2D simulations without requiring high levels of computational time and hardware resources.

Other than being useful, the proposed technique allows us to comprehend some of the difficulties encountered by the engineer in correctly customizing plasmonic gratings in order to promote a desired emission pattern. Indeed, when a particular emission pattern is wanted by means of an undefined grating, the search for the proper combination of interstice lengths and grooves/ridges form, and aspect ratio (which affects both the complex plasmonic coefficients and the scattering function) increases in complexity and areal project is not feasible, especially in consideration of anisotropic and asymmetric scattering.

Thus it is somehow suggestible, when one requires a defined scattering pattern, to make a fast scan with multiple loops over many gratings' configurations by means of the presented algorithm, and consequently select the fittest configuration to reproduce the desired ID. To this purpose, a code implemented to execute the presented

procedure can eventually be incorporated into a larger one featuring multiparametric scan or even supporting genetic algorithms for the selection of one or more optimal configurations when in search of a desired emission pattern.

4.4. - References.

- [1] H. Raether. “Surface Plasmons on Smooth and Rough Surfaces and on Gratings”, Vol. 111 of Springer Tracts in Modern Physics (Springer-Verlag, 1988).
- [2] S. A. Maier. “Plasmonics: Fundamental and Applications”, (Springer, 2007).
- [3] B. Zeng, Et al. “Ultrathin nanostructured metals for highly transmissive plasmonic subtractive color filters,” *Sci. Rep.* 3, 2840 (2013).
- [4] Y. S. Do, Et al. “Plasmonic color filter and its fabrication for large-area applications,” *Adv. Opt. Mater.* 1, 133–138 (2013).
- [5] J.N. Anker, Et al. “Biosensing with plasmonic nanosensors,” *Nat. Mater.* 7, 442–453 (2008).
- [6] F. Pincemin, Et al. “Scattering of a surface plasmon polariton by a surface defect,” *Phys. Rev. B* 50, 15261–15275 (1994).
- [7] A. Yu. Nikitin, Et al. “Scattering of surface plasmon polaritons by impedance barriers: dependence on angle of incidence,” *Phys. Rev. B* 77, 195441 (2008).
- [8] M. Kuttge, Et al. “How grooves reflect and confine surface plasmon polaritons,” *Opt. Express* 17, 10385–10392 (2009).
- [9] G. Brucoli and L. Martín-Moreno, “Comparative study of surface plasmon scattering by shallow ridges and grooves,” *Phys. Rev. B* 83, 045422 (2011).
- [10] A. V. Zayats, Et al. “Nanooptics of surface plasmon polaritons,” *Phys. Rep.* 408, 131–314 (2005).
- [11] E. S. Lee, Et al. “Bragg reflection of terahertz waves in plasmonic crystals,” *Opt. Express* 17, 9212–9218 (2009).
- [12] T. Vary and P. Markos, “Propagation of surface plasmons through planar interface,” *Proc. SPIE* 7353, 73530K (2009).
- [13] H. Liu and P. Lalanne, “Surface plasmon generation by subwavelength isolated objects,” *IEEE J. Sel. Top. Quantum Electron.* 14, 1522–1529 (2008).
- [14] C. Balanis. “Antenna Theory”, 3rd ed. (Wiley, 2005).

- [15] A. Dhawan, Et al. “Narrow groove plasmonic nano-gratings for surface plasmon resonance sensing,” *Opt. Express* 19, 787–813 (2011).
- [16] F. Pincemin and J.-J. Greffet, “Propagation and localization of a surface Plasmon polariton on a finite grating,” *J.Opt.Soc.Am.B* 13, 1499–1509 (1996).
- [17] F. Lòpez-Tejera, Et al. “Scattering of surface plasmons by one-dimensional periodic nanoindented surfaces,” *Phys. Rev. B* 72, 161405(R) (2005).
- [18] T. Søndergaard, Et al. “Theoretical analysis of ridge gratings for long-range surface plasmon polaritons,” *Phys. Rev. B* 73, 045320 (2006).
- [19] H. Liu and P.Lalanne, “Light scattering by metallic surfaces with subwavelength patterns,” *Phys. Rev. B* 82, 115418 (2010).
- [20] J. A. Sanchez-Gil, “Distributed feedback gratings for surfaceplasmon polaritons based on metal nano-groove/ridge arrays,” *Opt. Lett.* 32, 2330–2332 (2007).
- [21] F. J. Garcìa-Vidal, Et al. “Localized surface plasmons in lamellar metallic gratings,” *J. Lightwave Technol.* 17, 2191–2195 (1999).
- [22] T.-K. Liu, Et al. “Sensible measurement of localized surface plasmon based on lithographic gratings,” *Proc. SPIE* 7135, 71352I (2008).
- [23] A. Barbara, Et al. “Plasmon dispersion diagram and localization effects in a three-cavity commensurate grating,” *Opt. Express* 18, 14913–14925 (2010).
- [24] R. Petit. “Electromagnetic Theory of Gratings”, (Springer-Verlag, 1980).
- [25] R. E. Collin. “Field Theory of Guided Waves”, (McGraw-Hill, 1960).
- [26] C. Ropers, Et al. “Plasmon-enhanced Bragg diffraction,” *Phys. Rev. B* 86, 205122 (2012).
- [27] Y. Takakura, “Optical resonance in a narrow slit in a thick metallic screen,” *Phys. Rev. Lett.* 86, 5601–5603 (2001).
- [28] Y. Xie, Et al. “Transmission of light in slit apertures in metallic films,” *Opt. Express* 12, 6106–6121 (2004).
- [29] P. Lalanne, Et al. “Approximate model for surface-plasmon generation at slit apertures,” *J. Opt. Soc. Am. A* 23, 1608–1615 (2006).
- [30] N. C. Lindquist, Et al. “Plasmonic nanofocusing with a metallic pyramid and an integrated C-shaped aperture,” *Sci. Rep.* 3, 1857 (2013).
- [31] G. Li and J. Zhang, “Ultra-broadband and efficient surface plasmon polariton launching through metallic nanoslits of subwavelength period,” *Sci. Rep.* 4, 5914 (2014).

- [32] H. Liu and P. Lalanne, “Microscopic theory of the extraordinary optical transmission,” *Nature* 452, 728–731 (2008).
- [33] L. Sahin, Et al. “Enhanced transmission of electromagnetic waves through splitting resonator-shaped apertures,” *J. Nanophotonics* 5, 051812 (2011).
- [34] F. vanBeijnum, Et al. “Quasi-cylindrical wave contribution in experiments on extraordinary optical transmission,” *Nature* 492, 411–414 (2012).
- [35] J. Lekner. “Theory of Reflection of Electromagnetic and Particle Waves”, (Springer Science & Business Media, 1987).
- [36] E. Palik. “Handbook of Optical Constants of Solids”, (Academic, 1991).

Chapter 5. – Analysis on vertical directional couplers with long range surface plasmons for multilayer optical routing.

5.1. - Introduction.

The realization of efficient Optical Integrated Circuits is one of the key efforts in order to respond to the increasing demand of high speed signal transfer and manipulation. An alternative technology to the more popular dielectric waveguide-based devices is represented by Surface Plasmon Polaritons based systems, which have been extensively researched for various applications [1– 3]. Long Range Surface Plasmon Polaritons (LR-SPPs) have received special attention, mainly due to the fact that they offer reduced propagation losses and easier interfacing with standard optical fibers, compared to the strong-confinement of SPP-based structures [4, 5]. Many LR-SPP based devices operating at telecom wavelengths have been realized and presented in the literature [1]; measurements on some specific geometries demonstrated a high data transmission capability [6 – 8] and a good coupling with Single Mode Optical Fibers [2, 9, 10]; electrical switching has been demonstrated [2]; and optical switching is possible [11].

Those devices consist of very thin metal stripes (width \gg thickness) inside a homogenous dielectric medium and usually perform their operations in a planar geometry [1]. The bound modes propagate along the dielectric/metal interface, and most of the field is localized on the dielectric side. While classical dominant technologies based on dielectric cores require multiple lithography steps, accurate deposition processes, and a good control over doping [1, 2], LR-SPP based devices need care only to the deposition of ultrathin metal layer, as the dielectric growth and lithography are more lenient on precision [2]. Moreover, when nonpolymeric dielectrics are used in dielectric core based devices, the thickness of the films acts as a major limiting factor, as it is proportional to the costs and because of the mechanical stress for values exceeding $\sim 1\mu\text{m}$; on the other hand, polymeric dielectrics can act as a very good medium for LR-SPPs and can be easily deposited on films several micrometers thick without incurring in significant mechanical stress [12]. In practice, LR-SPP technology is much cheaper than its counterpart and allows to vertically “stack” multiple layers, which is a key requirement for multilayer optical routing.

Directional coupling is one of the fundamental passive operations, and LR-SPP based directional couplers have been extensively studied [13 – 17]. Most of the devices are expected to operate at a single plane, so Lateral Directional Couplers (LDC) have been developed and optimized. Vertical Directional Couplers (VDC) between LR-SPPs has also been studied in Refs. 18 and 19; in the former work, an interferometer using such a phenomenon has been experimentally demonstrated, showing significant increase in interaction, while in the latter a comparative study with LDC has been done by taking into account the effect of the main topological (geometrical) parameters. Both works underline the potentialities of this process in the creation of multilayer photonic routing, as well as the reduction of Coupling Length, which means shorter devices and thus lower losses due to propagation.

The bend radius of the sample built in Ref. 18 was too small ($\sim 600 \mu\text{m}$ as can be estimated from the images), which resulted in a significant amount of power loss due to radiation and transition, as also stated by the authors; the results lose a quantitative meaning, making the work a good qualitative proof-of-principle. The increased interaction makes the device more sensitive to geometrical nonidealities due to fabrication imprecisions; also, the analyses have been done on vertical coupling between two straight paths and ignored the interaction on the bent part, which we demonstrate to be significant. Thus, in Refs. 18 and 19, the authors needed further parameters in order to describe all the main characteristics of the VDCs.

In the present work, a Vertical Directional Coupler (VDC) structure working in the third window ($\lambda = 1.55 \mu\text{m}$) is proposed and analyzed with the aim of achieving efficient optical routing. Differently from previous works, in order to obtain exhaustive information about the overall behavior of the device, this analysis comprises also the important topic of the additional interaction on the bent part: a practical method is presented and applied in order to engineer the correct combinations of geometrical parameters to reach the desired final amount of signal exchange, even in the presence of small geometrical parameter's variations due to fabrication issues. The scheme of the device presented here is designed in order to minimize propagation losses thanks to the presence of one only S-Bend. Between the various possible applications, we underline that the abilities to easily “stack” multiple planar circuits, and enabling them to communicate through these efficient VDCs, make LR-SPP technology a good option for the production of cheap and high density network systems [20].

In Section 2, the scheme of the device is presented along with the main parameters and settings of the calculations. In Section 3, the computation of the coupling coefficients of the different paths of the device is shown; in particular, the method used to compute the additional coupling of S-Bend is presented. In Section 4, the relationship between fabrication tolerances and relative performance to the change of some parameters is evaluated. Finally, the main summary and conclusions are drawn.

5.2. - Schematic and settings.

The calculations presented in this chapter have been carried out at telecom wavelength of $\lambda = 1.55 \mu\text{m}$ and will be focused on the fundamental, symmetric, bound quasi-*TM* modes [1, 2, 4, 5]. There are many possible geometries that can implement vertical directional coupling [18, 19, 21 – 25]; in the present work, the analysis is focused on a structure represented by two elements in two different layers: a “long” straight stripe on a layer, while on another layer two “short” straight stripes are connected on the ends of a S-bend (Figs. 1(a)–1(c) show the unscaled scheme of the whole structure).

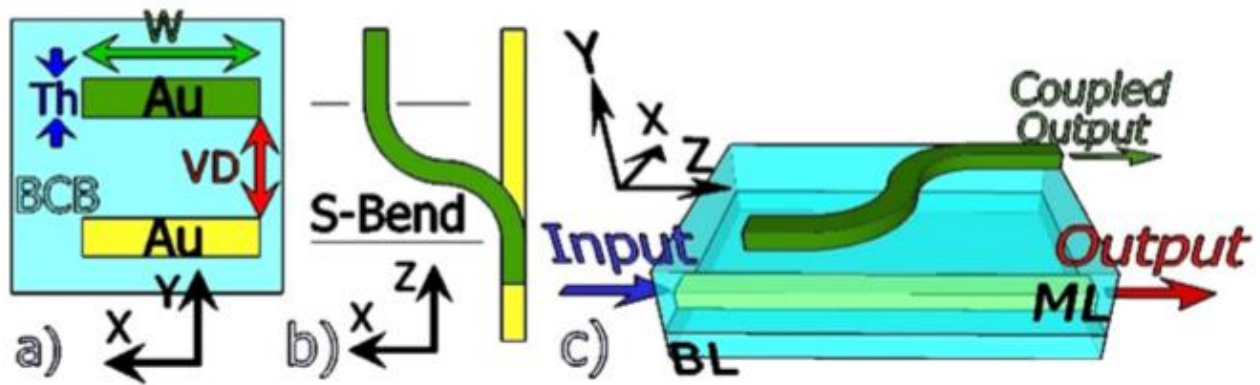


Figure 5.1. Different unscaled views of the device, with Cartesian axes. (a) Transverse view of the scheme, with the main parameters. (b) Scheme of the structure from top view. (c) 3-D view of the structure, with signal paths; top dielectric is not shown for graphical purposes.

The two layers are positioned in order to guarantee that one of the “short” straight stripes is parallel on both the vertical and horizontal directions with the “long” one (from a top view, they are overlapped); this is the region where the “straight coupling” will take place. In the region where the long straight stripe will interact with the bent stripe, “additional coupling” shall take place. These two couplings compose the total signal exchange of the device, since on the other ends the stripes are far enough to approximate the interaction to zero.

The analyzed structure has three signal ports: input, output, and coupled output. The long straight waveguide (on layer 1- in yellow) is connected on both ends with external signal paths (i.e., single mode optical fiber), which are the input and output; the S-bend (layer 2 in green in Fig. 5.1) is connected only through the coupled output.

This scheme has been decided in order to minimize insertion loss, which is the sum of all propagation, radiation, and transition losses. Big bend radii allow to reduce power loss due to radiation and transition [26], while the propagation length is reduced by increasing the interaction (as shown in Sections 5.3A and 5.3B) and by reducing the total path length; this element requires a single S-bend, differently than most directional couplers [15 – 18]; thus, it propagates on shorter paths.

In what follows, the main geometrical parameters that will be engineered are: vertical distance (VD) between the layers, the bending radius (R) of the S-bend, the single stripes’ width (W), and thickness (T). The horizontal displacement of the S-bend (distance between output and coupled output) has been fixed at 250 μm .

Once the main rule of having very low thickness is satisfied, the other geometrical shapes (W, R, VD) can be controlled to adjust the selected performance of the device. The geometrical dimensions of this analysis have been chosen to be around the range of the landmark structures present in literature [16, 17]; here Au stripes ($\epsilon_r = -93.0839 + i*11.1097$ at $\lambda = 1.55\mu\text{m}$) are embedded within polymer cladding ($n =$

1.443 at $\lambda = 1.55 \mu\text{m}$), with widths between $4 \mu\text{m}$ and $10 \mu\text{m}$ and thicknesses between 15nm and 25nm . Since those structures have a low propagation loss, a low coupling loss with SM-fiber and proven measurement values, it is easier to make comparisons.

5.3. - Parameter Evaluation.

A. Coupling length of the straight path.

In order to compute the (co)directional coupling between the strips, a supermode approach to coupled mode theory has been used [24]; the same method has been successfully used with LR-SPPs in Refs. 16, 23, 25, and 27, showing very good matching between experiments and calculations. Through Finite Element analysis (2-D) on two vertically parallel strips, the effective indexes of the symmetric and antisymmetric supermodes related to the fundamental quasi-TM mode have been extracted; from that, the “coupling length” (L_C), which is the minimum length necessary for two parallel paths to completely transfer an input signal from one to another, and the corresponding coupling coefficient (K) can be obtained from Ref. 24

$$L_C = \frac{2\pi}{\text{Re}[\beta_S - \beta_{As}]} = \frac{\pi}{2K} \quad (5.1)$$

with β_S and β_{As} the symmetric (even) and antisymmetric (odd) propagation constants, respectively, of the overall structure. As can be discerned from (1), an increase in L_C corresponds to a decrease of K and interaction. Once K or L_C are obtained, the exchange of power between the two straight stripes through the interaction path can be calculated through Ref. 24

$$\begin{aligned} P_1 &= P_0 \times \cos^2(K_Z), \\ P_2 &= P_0 \times \sin^2(K_Z) \end{aligned} \quad (5.2)$$

being P_1 and P_2 the input and coupled stripes' power, and Z is the longitudinal axis. The relation between the computed L_C and the VD between the two straight paths is shown in Fig. 5.2; stripes with different widths (thickness is fixed at 20nm) in Fig. 5.2(a) and thicknesses (width is fixed at $8 \mu\text{m}$) in Fig. 5.2(b) are shown.

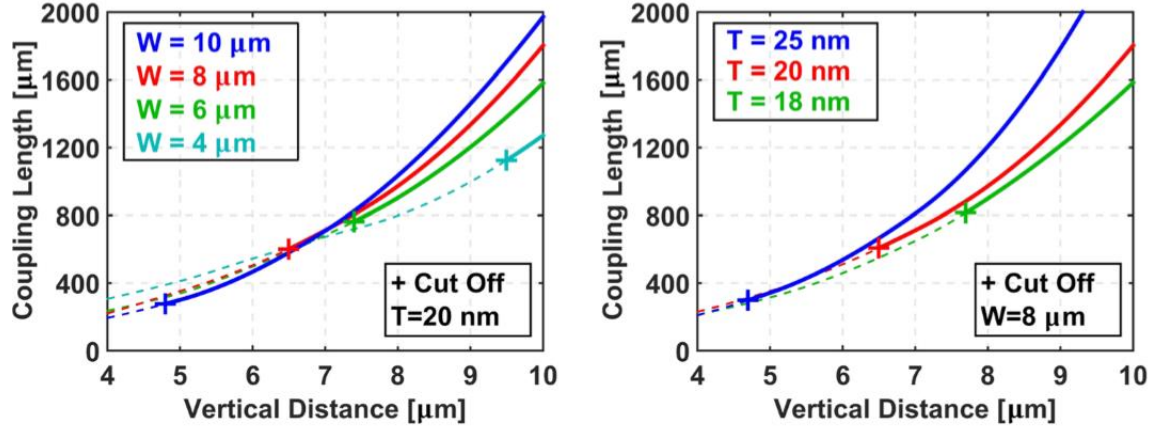


Figure 5.2. (a) Coupling Length as a function of the vertical distance for a fixed $T = 20 \text{ nm}$ and for $W = 10 \text{ μm}$ (blue line), $W = 8 \text{ μm}$ (red line), $W = 6 \text{ μm}$ (green line), and $W = 4 \text{ μm}$ (cyan line). (b) Coupling Length as a function of the vertical distance for a fixed $W = 8 \text{ μm}$ and for $T = 25 \text{ nm}$ (blue line), $T = 20 \text{ nm}$ (red line), and $T = 18 \text{ nm}$ (green line).

L_C is shorter than LDCs since the mode field is distributed more in the vertical direction than lateral: the overlap areas are increased, resulting in enhanced interactions [5, 18, 28]. A small L_C allows to have a reduced straight path and thus low overall propagation losses (but this also makes the additional coupling on the bent part more significant, as shown in Section 5.3B). As reported in Ref. 18, a limit value of VD has been found, under which the odd supermode reaches its cut-off limit and becomes leaky (dotted line in Figs. 5.2(a) and 5.2(b)). It can be observed that the increase in the size of the single stripes' width and thickness may decrease the cut-off VD value, allowing to reduce L_C more, but this needs to be counterweighted with increased losses [1, 2, 4, 5, 19].

B. Additional coupling computation and control.

In order to have negligible radiation and transition losses, LR-SPP strip based devices and circuits have very big bending radii, on the order of tens of millimeters [16, 23, 26].

This means that the separation of the two strips in the bent part of VDCs will be slow, so a relevant amount of additional coupling is expected, due also to the strong interaction along the vertical direction. Thus, while in conventional LDCs the additional coupling has a small influence on the overall device, in VDCs it is significant and needs to be taken into account. Thus, an approximated method has been introduced in order to calculate it through the same theory, tools, and simplified relations used for the straight path coupling.

The calculation of the additional coupling has been done after several steps: at first, the relation between L_C and the Lateral Distance (LD) has been computed by means of the discussed method in Section 5.IIIA (Figs. 5.3(a) and 5.3(b)); then, the

values have been interpolated; finally, after approximating a bend into many small straight segments, each with a specific LD calculated from the straight strip (Fig. 5.3(c)), the total signal exchange has been obtained by combining together all contributions from the segments.

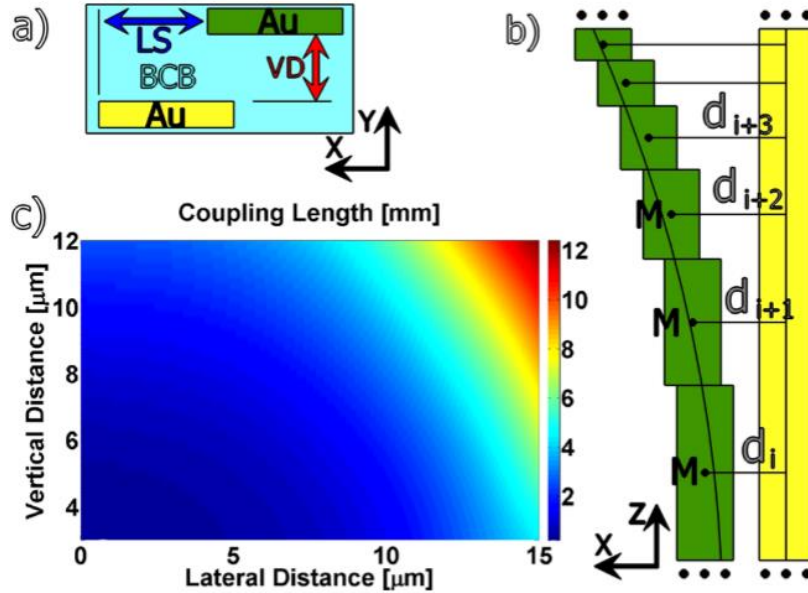


Figure 5.3. (a) Transverse unscaled view of the scheme used for the 2D Finite Element analysis, with the main parameters. (b) Plot of the Coupling Length as a function of the lateral distance among the waveguides for different vertical distance values. (c) Geometrical description of the mathematical method: the bend is divided into many small segments (each one is laterally shifted from the previous and the next by a very small value); the length of the segments shrinks as the lateral shift grows.

The different losses due to propagation through the two different paths have been taken into account: while on the straight line the attenuation loss of each segment is proportional to the length dz , on the S-bend the corresponding segment has a proportionality to $dz \cdot d\theta$.

Since the interaction decreases exponentially with LD, the variations of δK have been neglected for $LD > 27 \mu\text{m}$: over that point, the directional coupling is too weak, and the biggest differentiation between the “main” and “coupled” signals is given by the different path length (and thus propagation loss). Since the stripes are still almost parallel when the calculation is truncated, expressions (1) and (2) keep valid, and consequently this method can be assumed as genuine for the chosen range of R .

This approach has been applied on LR-SPP stripes with $W = 8 \mu\text{m}$, $T = 20\text{nm}$, $VD = 7 \mu\text{m}$, $LD < 20 \mu\text{m}$, with various R (ranging from 8 mm to 40 mm) in order to find the optimum value for the desired coupling ratio, as shown in Fig. 5.4; on the plot, $Z = 0$ represents the starting point of the bend; normalized power ($P_{main}/(P_{main} + P_{coupled})$, $P_{coupled}/(P_{main} + P_{coupled})$) is shown in order to focus more on the power ratio. Since the final lateral shift between the output and the coupled output is fixed (at $250 \mu\text{m}$), each value of R changes the longitudinal length of the S-bend

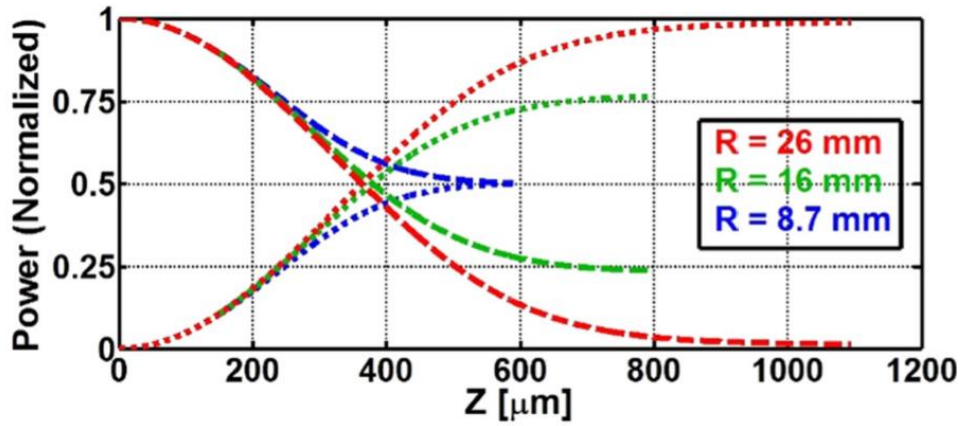


Figure 5.4. Normalized power exchange between the two stripes as a function of the length of the straight stripe (dashed line: $P_{main}/(P_{main}+P_{coupled})$, dotted line: $P_{coupled}/(P_{main}+P_{coupled})$). In the analyses, the stripes have $W = 8 \mu\text{m}$, $T = 20\text{nm}$, $VD = 7 \mu\text{m}$, propagation loss = 13.42 dB/cm (corresponding to measurements done as in Ref. 13), and several Rs. The calculation interrupts when $LD = 20 \mu\text{m}$. As can be seen, the final signal ratio can be adjusted by selecting R. The length of the device is also related to R, since the final LD is fixed.

With VD fixed, it is possible to choose the correct final power ratios (usually 50–50 or 100–0) by setting the value of R (Fig. 5.5); the only condition is that R needs to be high enough to guarantee that bend losses are due mainly to the propagation. As can be seen, there are ample areas of optimal topological choice for 100–0.

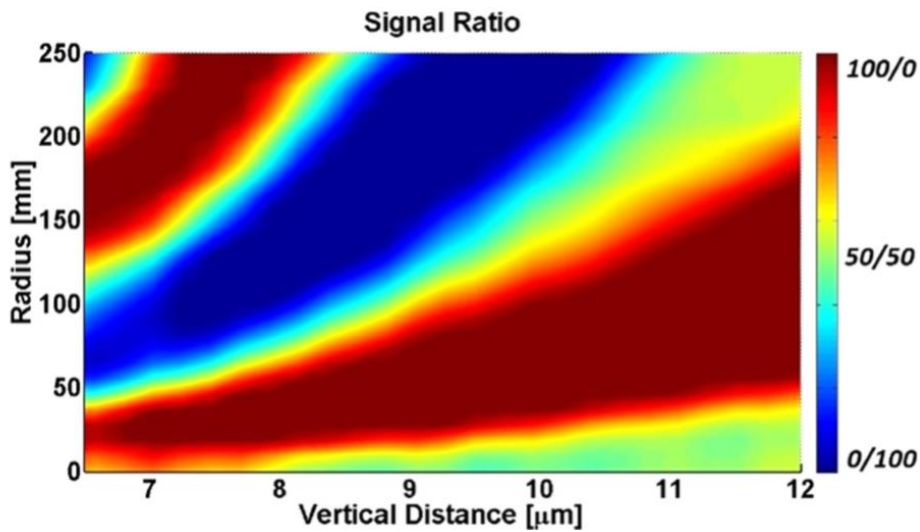


Figure 5.5. Final signal ratio of the S-Bend as a function of VD and R, with $W = 8 \mu\text{m}$ and $T = 20\text{nm}$. The calculation has been done by following the method presented above. The optimum value of R can be chosen from this graph, in combination with the length of the straight path.

At the same time, the straight part’s coupling ratio can be controlled with its length (Fig. 5.2). The total coupling of the device is given by the linear combination of the straight and S-bend parts.

Fig. 5.6 shows the coupling in the first part of S-bend when the input signal is set at the straight stripe, and $W = 8 \mu\text{m}$, $T = 20\text{nm}$, $VD = 7 \mu\text{m}$, $R = 30\text{mm}$, and $LD < 20 \mu\text{m}$; power has been extracted 100nm from the stripes. After a certain LD, the interaction becomes negligible, and the coupled power is subject mainly to propagation

loss; it should be noticed that, if X and Z axis had the same scale, they would be almost parallel (at $LD = 20 \mu\text{m}$, they would be tilted by 2°).

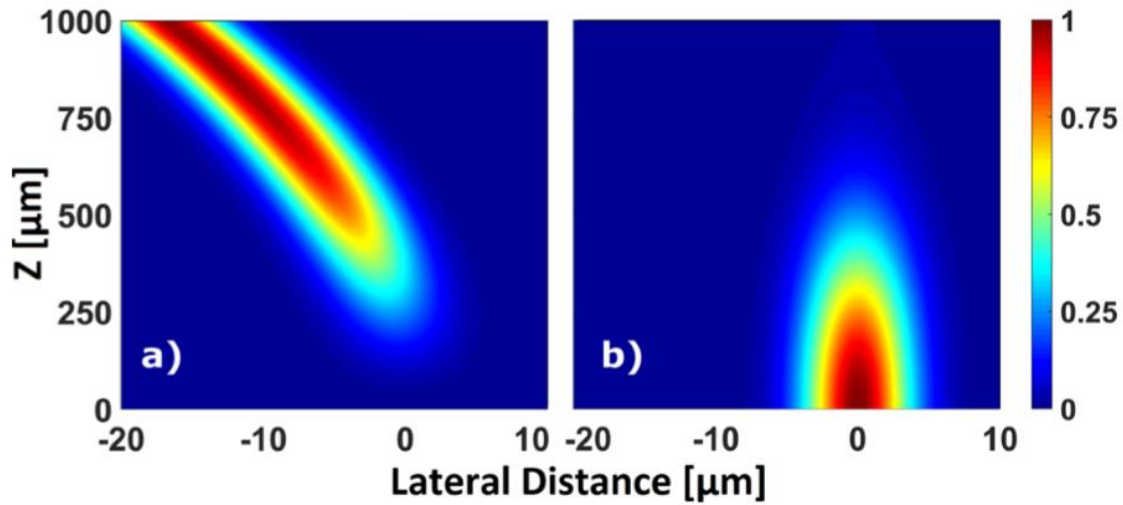


Figure 5.6. Optical power propagation extracted at 100 nm above and below the top and bottom stripes, respectively, for the 100–0 operation on the bend region up to a 20 μm LD, when $W = 8 \mu\text{m}$, $T = 20\text{nm}$, $VD = 7 \mu\text{m}$, and $R = 30\text{mm}$. (a) Power 100nm upon the S-Bend; from $LD = 20 \mu\text{m}$ to $250 \mu\text{m}$, this path carries almost the entirety of the total power, affected mainly by propagation loss from that point on. (b) Power below the straight stripe, which loses almost all power.

5.4. - Fabrication torerances.

There are in the literature many techniques, materials, and methods to fabricate ultra-thin-strip based systems on a single layer [21, 29, 30]. As shown in Sections 5.3A and 5.3B, when a multilayer interaction is involved, many geometrical parameters influence the operations, and need a specific degree of precision: stripes' width and thickness, flatness of the deposited layers, the thickness of the middle dielectric layer (VD), and the alignment between layers.

A good control over the deposited Au strips' thickness at nanometric scale is expected to be easily achievable with standard sputtering or evaporation machines, although at those dimensions the strips' flatness may be hindered by the presence of small lumps and cracks, whose main consequence is an additional propagation loss [31]. The relaxed sizes of the circuits (multi-micrometric width and multimillimetric bending radii) ease photolithographic processes with the currently available technologies, thus allowing repeatable results and a good control over the width. From Fig. 5.2, it is possible to discern that there are ideal VD values that allow to minimize the fabrication errors' effects; i.e., we notice from Fig. 5.2(a) that by choosing $VD = 7$

μm , $W = 8 \mu\text{m}$ and $T = 20\text{nm}$, it is possible to reduce significantly the effects of width variations.

VD has a significant influence on vertical Directional Coupling, as already shown in Sections 5.3A and 5.3B. Unfortunately, the cut-off values for VD are higher than the growth limits of particularly stable materials that can be deposited through accurate low-temperature fabrication processes (i.e., chemical vapor deposition grown SiO_2 [32]). The most viable materials seem to be polymeric dielectrics such as Benzocyclobutene, Cytop, or poly-methyl methacrylate, which can be deposited through spin coating, although a certain degree of inaccuracy of the film thickness (VD) is expected because of environmental conditions. By using the same methods described in Sections 5.3A and 5.3B, it is also possible to foresee the effects of the VD variations on the power exchange; while the straight coupling's characteristics are compromised, it is possible to compute for the S-Bend an optimum R that can minimize the variation of the final signal ratio. This is proven by Fig. 5.7, where the influence of a VD variation of $60.5 \mu\text{m}$ is shown, with all the other parameters fixed: $W = 8 \mu\text{m}$, $T = 20\text{nm}$, and $R = 23\text{mm}$. The chosen value of R makes allows to reduce, in the S-Bend, the effects of the variations on the final coupling ratio.

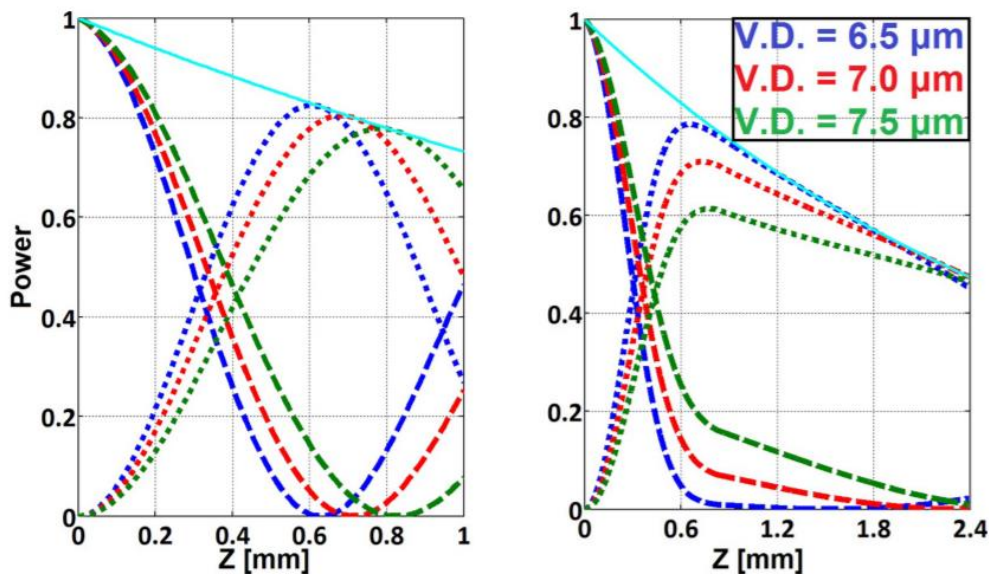


Figure 5.7. Power exchange for VDCs with $W = 8 \mu\text{m}$, $T = 20\text{nm}$, with different VDs; dashed line represents main path signal, and dotted line represents the coupled path signal. (a) On the straight coupling region VD variations change significantly the L_C . (b) In the additional coupling region, there are little changes to the final coupling ratio if $R = 23\text{mm}$.

Since this structure involves the patterning of two different layers, a certain amount of misalignment is expected. Just like VD variations, there is an optimum bend radius value that minimizes, in the S-Bend, the effects of misalignments; on the straight path L_C increases the same independently from the direction of the misalignment.

In Fig. 5.8, the resulting effects are shown, with $W = 8 \mu\text{m}$, $T = 20\text{nm}$, and $R = 23\text{mm}$, $VD = 7 \mu\text{m}$; positive misalignment represents the unwanted lateral shift of the layer towards the direction of the bend, while negative is on the opposite side.

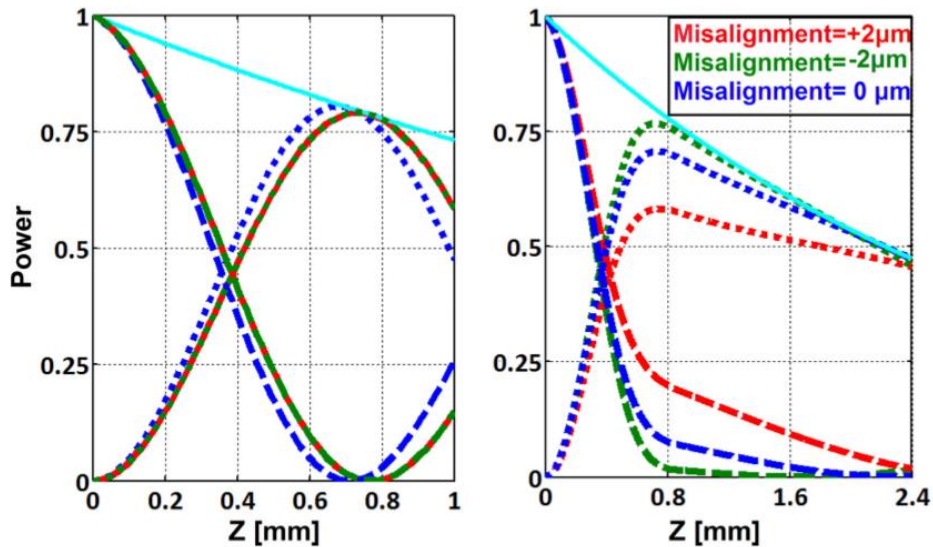


Figure 5.8. Power exchange for VDCs with $W = 8 \mu\text{m}$, $T = 20\text{nm}$, and $VD = 7\mu\text{m}$ with different misalignments; positive misalignment values represent the lateral shift of the layer towards the direction of the bend, while negative is on the opposite side. Dashed line represents main path signal, and dotted line represents the coupled path signal. (a) On the straight coupling region, misalignment variations increase LC, regardless of the direction. (b) In the additional coupling region, there are little changes to the final coupling ratio if it is close to the optimum, such as $R = 23\text{mm}$.

5.5. - Conclusions and future developments.

From the present analysis, it is possible to discern general information regarding VDCs and the methods to design them. We have introduced and used a pragmatic method to compute the interaction in the s-bend region; the approximations used within this method are coherent with the features of the most popular LR-SPP based systems. It is clear that, differently than LDCs, the interaction on the first parts of bends in VDCs is relevant and cannot be neglected. We have shown also that this "additional" coupling can be controlled by tuning the geometrical parameters, in particular, bend radius.

The major fabrication issues are those that affect the repeatability of the devices: the precision of the middle dielectric layer deposition and the misalignment between layers; their effect regards mainly the straight path, as the final coupling ratio of the bent path can be optimized through an optimum R calculated through the aforementioned method. Fig. 5.5 shows that if 100–0 additional coupling ratio is chosen for the s-bend, there is an ample range of values of bend radii to choose, like those used for Figs. 5.7 and 5.8. Lower governability of the straight path's coupling

ratio makes us expect more crosstalk in VDC than LDC, which can be reduced only by an increased amount of fabrication accuracy, and consequently costs.

Overall, while VDCs exhibit smaller propagation loss than LDCs, they require more fabrication complexity (still lower than standard dielectric based optical integrated circuits) and have lower precision in signal transmission. As formerly stated, to our opinion, the main reason to produce them should be the undeniable topological advantage they can give to LR-SPP optical circuits. The ability to easily stack different layers of optical integrated circuits which communicate through VDCs makes LR-SPP technology a good option for the production of complex network systems.

5.6. - Acknowledgments.

Many thanks to Professor Kristján Leósson and Dr. Luca Maiolo for the useful discussions on LR-SPPs and fabrication. Additionally, we would like to thank the S.B.A.I. Department for supporting us with their facilities.

- [1] S. A. Maier. “Plasmonics: Fundamentals and Applications”, (Springer, 2010).
- [2] P. Berini. “Long range surface plasmon polaritons,” *Adv. Opt. Photonics* 1, 484–588 (2009).
- [3] G. D’Aguanno, Et al. “Quenched optical transmission in ultrathin subwavelength plasmonic gratings,” *Phys. Rev. B* 83, 035426 (2011).
- [4] D. Sarid. “Long-range surface-plasma waves on very thin metal films,” *Phys. Rev. Lett.* 47(26), 1927–1930 (1981).
- [5] P. Berini. “Plasmon polariton waves guided by thin lossy metal films of finite width: Bound modes of symmetric structures,” *Phys. Rev. B* 61, 10484–10503 (2000).
- [6] J. J. Ju, Et al. “40 Gbit/s light signal transmission in long-range surface plasmon waveguides,” *Appl. Phys. Lett.* 91, 171117 (2007).
- [7] B. Banan, Et al. “Multi-channel transmission through a gold strip plasmonic waveguide embedded in Cytop,” *IEEE Photonics J.* 5(3), 2201811 (2013).
- [8] J. J. Ju, Et al. “Polymer-based long-range surface plasmon polariton waveguides for 10-Gbps optical signal transmission applications,” *J. Lightwave Technol.* 26(11), 1510–1518 (2008).
- [9] A. Degiron, Et al. “Guiding light with long range plasmons,” *Opt. Photonics News* 19, 28–34 (2008).
- [10] G. I. Stegeman, Et al. “Excitation of surface polaritons by end-fire coupling,” *Opt. Lett.* 8(7), 386–388 (1983).
- [11] N. Mattiucci, Et al. “Long range plasmon assisted all-optical switching at telecommunication wavelengths,” *Opt. Lett.* 37, 121 (2012).
- [12] R. G. Hunsperger. “Integrated Optics Theory and Technology” (Springer, 2009), Chap. 4–5, pp. 53–104.
- [13] A. Boltasseva and S. I. Bozhevolnyi, “Directional couplers using longrange surface plasmon polariton waveguides,” *J. Sel. Top. Quantum Electron.* 12, 1233–1241 (2006).

- [14] D. C. Zografopoulos and R. Beccherelli, “Long-range plasmonic directional coupler switches controlled by nematic liquid crystals,” *Opt. Express* 21(7), 8240–8250 (2013).
- [15] V. A. Zenin, Et al. “Directional coupling in long-range dielectric loaded plasmonic waveguides,” *Opt. Express* 21(7), 8799–8807 (2013).
- [16] A. Boltasseva, Et al. “Integrated optical components utilizing long-range surface plasmon polaritons,” *J. Lightwave Technol.* 23(1), 413–422 (2005).
- [17] R. Charbonneau, Et al. “Demonstration of integrated optics elements based on long-ranging surface plasmon polaritons,” *Opt. Express* 13(3), 977–984 (2005).
- [18] H. S. Won, Et al. “Vertical coupling of long-range surface plasmon polaritons,” *Appl. Phys. Lett.* 88, 011110 (2006).
- [19] T. Srivastava and A. Kumar, “Comparative study of directional couplers utilizing long-range surface plasmon polaritons,” *Appl. Opt.* 49(12), 2397–2402 (2010).
- [20] L. Carloni, P. Pande, and Y. Xie. “Networks-on-Chip in Emerging Interconnect Paradigms: Advantages and Challenges” (NOCS, San Diego, CA, 2009).
- [21] K. Leosson, Et al. “Longrange surface plasmon polariton nanowire waveguides for device applications,” *Opt. Express* 14(1), 314–319 (2006).
- [22] T. Holmgaard, Et al. “Long-range dielectricloaded surface plasmon-polariton waveguides,” *Opt. Express* 18(22), 23009–23015 (2010).
- [23] R. Charbonneau, Et al. “Passive integrated optics elements based on long-range surface plasmon-polaritons,” *J. Lightwave Technol.* 24(1), 477–494 (2006).
- [24] A. W. Snyder and J. D. Love. “Optical Waveguide Theory” (Chapman and Hall, London, 1983), Chap. 18, p. 387.
- [25] F. Liu, Et al. “Hybrid coupling between long-range surface plasmon polariton mode and dielectric waveguide mode,” *J. Lightwave Technol.* 29(9), 1265–1273 (2011).
- [26] P. Berini and J. Lu, “Curved long-range surface plasmon-polariton waveguides,” *Opt. Express* 14(6), 2365–2371 (2006).
- [27] J. Gosciniak, Et al. “Theoretical analysis of long-range dielectric-loaded surface plasmon polariton waveguides,” *J. Lightwave Technol.* 29(10), 1473–1481 (2011).
- [28] S. L. Chuang, “Application of the strongly coupled-mode theory to integrated optical devices,” *IEEE J. Quantum Electron.* QE–23(23), 499–509 (1987)
- [29] Y. Xie, Et al. “Fabrication of long-range surface plasmon polaritons waveguide by wet chemical etching,” *J. Optics* 16(6), 065006 (2014).

- [30] J. T. Kim, Et al. “Gold stripe optical waveguides fabricated by a novel double-layered liftoff process,” ETRI J. 31(6), 778–783, 1225–6463 (2009).
- [31] I. Slovinsky, Et al. “Propagation loss of long-range surface plasmon polariton gold stripe waveguides in the thin-film limit,” Plasmonics 8, 1613–1619 (2013).
- [32] G. Y. Yeom, “Plasma-enhanced chemical vapor deposition of SiO₂ thin films,” J. Korean Phys. Soc. 53(2), 892–896 (2008).

Chapter 6. – Fabrication techniques.

In this subsection are reported the main fabrication processes following the top-down approach, employed during my PhD studies. Most of them result largely used in micro-fabrication but can be adapted in the nano-fabrication field.

6.1. - Spin coating and hot plate.

Spin coating is a fabrication process with the aim to deposit uniform thin films to flat substrate. Typically, a small portion of coating material is applied on the center of the substrate, which is either spinning at low speed or not spinning at all. Then, the substrate rotated at high speed in order to spread the coating material by centrifugal force. The system used for spin coating is called a *spin coater*, or simply *spinner*.

The rotations persist while the fluid spins off the edges of the substrate and the desired thickness of the film is achieved. The applied solvent is usually volatile, and simultaneously evaporates. So, the higher the angular speed of spinning, the thinner the film. The thickness of the film also depends on the viscosity and concentration of the solution and the solvent [1].

Spin coating is largely used in micro-fabrication of oxide layers using sol-gel precursors, where it can be used to create uniform thin films with nanoscale thicknesses. It is also used intensively in photolithography, to deposit layers of photoresist with a thickness which can typically vary between 100nm to 5 μ m depending on is taking place micro-fabrication or nano-fabrication.

The spin coating process is usually followed by the *hot plate* process. A hot plate is a portable self-contained tabletop small appliance that features one, two or more electric heating elements or gas burners; In laboratory settings, hot plates are generally used to heat glassware or its contents. Some hot plates also contain a magnetic stirrer, allowing the heated liquid to be stirred automatically. In micro and nano fabrication the hot plate instrument is widely used to dry the polymer materials in order to improve their deposition.

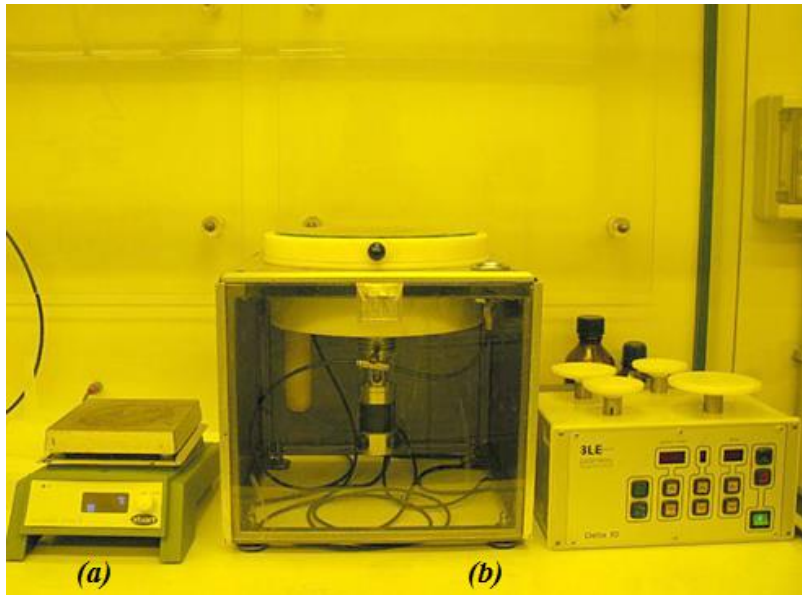


Figure 6.1. A spin coater (b) and a hot plate (a) system. The machines are contained in the CNR-IMM labs.

6.2. - Vacuum evaporator.

The *vacuum deposition* is a class of fabrication processes used to deposit layers of material atom-by-atom or molecule-by-molecule on a solid surface. These processes operate at pressures well below atmospheric pressure, i.e., vacuum. The process can be qualified based on the vapor source; *Evaporation* is a method widely used for thin-film deposition in micro-fabrication and to make macro-scale products such as metalized plastic film.

Evaporation implicate two basic physical processes: a hot source material *evaporates* and *condenses* on the substrate. The evaporation takes place in a vacuum, i.e. vapors other than the source material are almost entirely removed before the process begins; this is motivated by the fact that in high vacuum evaporated particles can travel directly to the deposition target without colliding with the background gas. At a typical pressure of 10^{-4} Pa, an 0.4nm particle has a mean free path of 60m. Furthermore, evaporated atoms that collide with foreign particles may react with them; for instance, if aluminium is deposited in the presence of oxygen, it will form aluminium oxide. They also reduce the amount of vapor that reaches the substrate, which makes the thickness difficult to control.

The evaporated materials attack the substrate generally from a single direction (mostly are preferred vertical depositions); so non-uniformity of the substrate can block the evaporated material from some areas. This phenomenon is called “shadowing” or “Step coverage”.

In any evaporation system is included a vacuum pump and an energy source that evaporates the material to be deposited. Many different energy sources exist:

In the *thermal* method, metal material (in the form of wire, pellets, shot) is fed onto heated semimetal (ceramic) evaporators known as "boats" due to their shape. Alternatively, the source material is placed in a crucible, which is heated by radiation by the means of an electric filament, or the source material may be hung from the filament itself (*filament evaporation*).

In the *electron-beam* method, the source is heated by an electron beam with an energy up to 15 keV.

In *flash evaporation*, a fine wire of source material is fed continuously onto a hot ceramic bar, and evaporates on contact.

Resistive evaporation is accomplished by passing a large current through a resistive wire or foil containing the material to be deposited. The heating element is often referred to as an "evaporation source". Boat type evaporation sources are made from tungsten, tantalum, molybdenum or ceramic type materials capable of withstanding high temperatures.

Finally, some systems mount the substrate on an out-of-plane planetary mechanism. The mechanism rotates the substrate simultaneously around two axes, to reduce shadowing [2, 3].

In my PhD thesis I will always refer to thermal method when I appoint the vacuum evaporation.

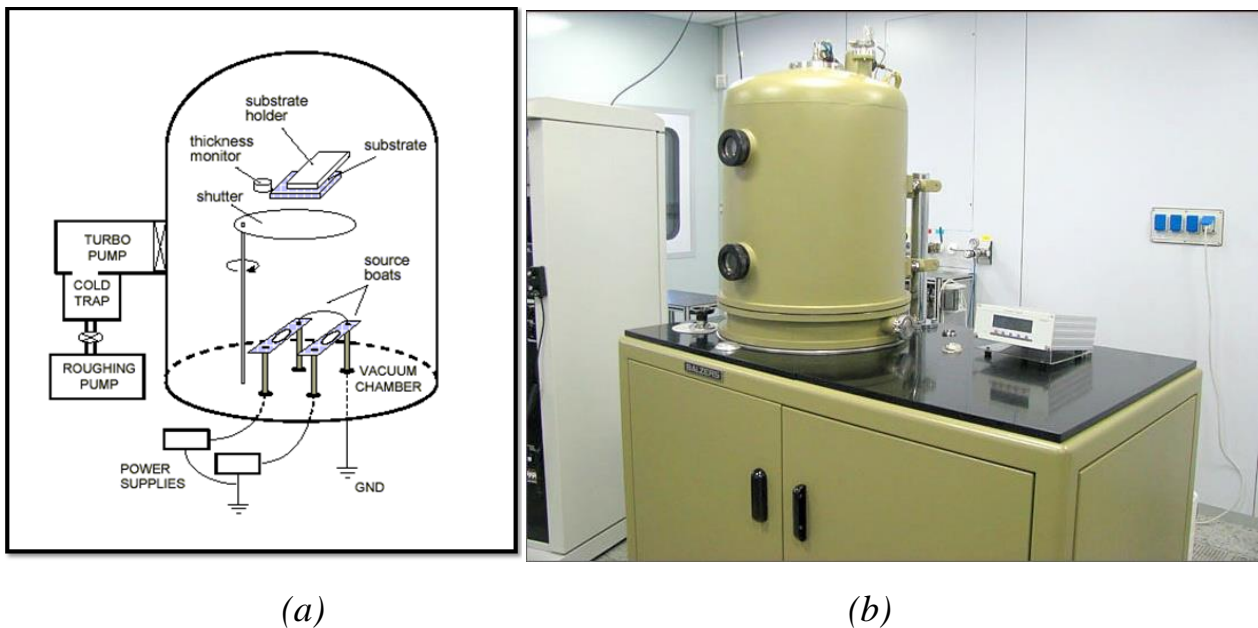


Figure 6.2. (a) Cross sectional view of a vacuum deposition system. (b) ABalzers 510 Evaporation System; the machine is contained in the CNR-IMM labs.

6.3. - Sputtering.

The *sputtering* is a process usually utilized for metal thin-film deposition and etching material.

In this method, the particles are ejected from a solid target material due to bombardment of the target by other energetic particles (generally gas ions). Such phenomenon happens when the kinetic energy of the incoming particles is much higher than conventional thermal energies ($\gg 1\text{eV}$) and then greater than the surface binding energy. If the target is thin on an atomic scale, the collision cascade can reach the back side of the target and atoms can escape the surface binding energy "in transmission". The average number of atoms ejected from the target per incident ion is called the sputter yield and depends on the ion incident angle, the energy of the ion, the masses of the ion and target atoms, and the surface binding energy of atoms in the target. For a crystalline target the orientation of the crystal axes with respect to the target surface is relevant. So, the physical sputtering is driven by momentum exchange between the ions atoms in the target materials due to collision [4- 6].

Physical sputtering has a well-defined minimum energy threshold equal to or larger than the ion energy at which the maximum energy transfer of the ion to a sample atom equals the binding energy of a surface atom. This threshold typically is somewhere in the range 10–100eV. The primary particles for the sputtering process can be supplied in a number of ways: for example, by a plasma, an ion source, an accelerator or by a radioactive material emitting alpha particles.

The *sputter deposition* is a *physical vapor deposition* (PVD) methods of thin film made by sputtering. This involves ejecting material from the target that, in this case, is the source onto a substrate: sputtered atoms ejected from the target have a wide energy distribution, typically up to tens of eV (100,000 K), the sputtered ions (typically only a small fraction of the ejected particles are ionized, on the order of 1%) can ballistically fly from the target in straight lines and impact energetically on the substrate causing the depositing of the particles. Sputtering deposition usually uses for the primary particles an argon plasma because argon, a noble gas, will not react with the target material.

There are many type of sputter deposition, following are reported the most widely used:

Magnetron sputtering: in this method the sources employ magnetrons that utilize strong electric and magnetic fields to confine charged plasma particles close to the surface of the sputter target. In a magnetic field, electrons follow helical paths around magnetic field lines, undergoing more ionizing collisions with gaseous neutrals near the target surface than would otherwise occur. The extra plasma ions created as a result of these collisions lead to a higher deposition rate and can also be sustained at a lower pressure.

RF sputtering: this method is often present together with the magnetron sputtering; in RF sputtering the sign of the anode-cathode bias is varied at a high rate (commonly 13.56 MHz), it is generally used in order to produce highly insulating oxide films [2]; but it has the negative consequence to added expense of RF power supplies and impedance matching networks.

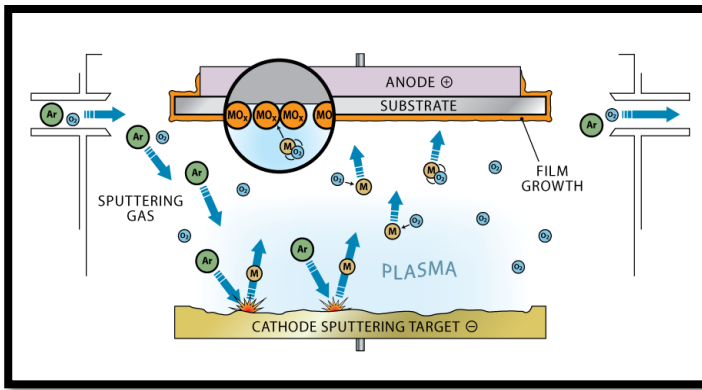
Ion-beam sputtering (IBS) is a method in which the target is external to the ion source. The advantage of IBS reside in the fact of have the energy and flux of ions controlled independently and it has found large application in the manufacture of thin-film heads for disk drives. The principal drawback of IBS is the large amount of maintenance required to keep the ion source operating.

Reactive sputtering: in this method the sputtered particles undergo a chemical reaction before coating the substrate. The composition of the film can be controlled by varying the relative pressures of the inert and reactive gases and with this method the deposited film can be different from the target material.

Ion-assisted deposition (IAD): the substrate is exposed to a secondary ion beam operating at a lower power than the sputter gun. NASA used this technique to experiment with depositing diamond films on turbine blades in the 1980s. IAD is used in other important industrial applications such as creating tetrahedral amorphous carbon surface coatings on hard disk platters and hard transition metal nitride coatings on medical implants.

At last, the sputtering process can lead, during prolonged ion or plasma bombardment of the target to significant erosion of material, this phenomenon in semiconductor industry is largely used to etch the samples [7]. Sputter etching is chosen in cases where a high degree of etching anisotropy is needed and selectivity is not a concern; the major drawback of this technique is wafer damage.

During my PhD I have usually used the magnetron and RF sputtering.



(a)



(b)

Figure 6.3. (a) Schematic description of the sputter process inside the sputter deposition machine's room.(b) AVS-40 Sistec Sputtering System; the machine is contained in the CNR-IMM labs.

6.4. - Photolithography.

The *photolithography*, also denominated *optical lithography* or *UV lithography*, is a process widely used in microfabrication to transfer a geometric pattern from a photomask to a light-sensitive chemical "photoresist", or simply "resist," on the substrate with light. Then a series of chemical treatments then either engraves the exposure pattern into, or enables deposition of a new material in the desired pattern upon, the material underneath the photo resist; so, a single iteration of photolithography combines several steps in sequence.

The manufacture of a microelectronic device can need more photolithography cycles; in complex integrated circuits, for example, a modern CMOS wafer will go through the photolithographic cycle up to 50 times.

The geometries desired are imprinted to the photoresist through a *photomask*: an opaque plate with holes or transparencies that allow light to shine through in a defined pattern; the cost of a photomask may vary depending on the resolution of the design structure; for high resolution masks, with dimension of the micron order, can reach several thousands of euros.

Follow are reported the principal steps for a single photolithography process:

- I. *Cleaning*: if on the wafer surface are present organic or inorganic contaminations, they are usually removed by wet chemical treatment, e.g. the RCA clean procedure based on solutions containing hydrogen peroxide. In order

to clean are also used other solutions made with trichloroethylene, acetone or methanol.

- II. *Preparation*: the wafer is heated to a temperature sufficient to drive off any moisture that may be present on the wafer surface, 150 °C for ten minutes is sufficient. Then a liquid or gaseous "adhesion promoter", such as Bis(trimethylsilyl)amine ("hexamethyldisilazane", HMDS), are usually applied to promote adhesion of the photoresist to the wafer [9].
- III. *Photoresist application*: The wafer is covered with photoresist by spin coating (section 2.7.1). The photo resist-coated wafer is then prebaked to drive off excess photoresist solvent, typically at 90 to 100 °C for 30 to 60 seconds on a hotplate.
- IV. *Exposure and developping*: the photoresist is exposed to a pattern of intense light. The exposure to light causes a chemical change that allows some of the photoresist to be removed by a special solution, called "developer". *Positive photoresist*, the most common type, becomes soluble in the developer when exposed; with *negative photoresist*, unexposed regions are soluble in the developer. Sometimes it is better to "hard-baked" the resulting wafer, typically at 120 to 180 °C for 20 to 30 minutes, in order to solidify the remaining photoresist, to make a more durable protecting layer in future ion implantation, wet chemical etching, or plasma etching.
- V. *Photoresist removal*: After a photoresist is no longer needed, it must be removed from the substrate. This usually requires a liquid "resist stripper", which chemically alters the resist so that it no longer adheres to the substrate. Another method for dry etch the photoresist is made by using plasma containing oxygen, which oxidizes it; this process is called *ashing*.

For the first photolithographic systems, from the early 1960s through the mid-1980s, were used ultraviolet light from gas-discharge lamps using mercury, sometimes in combination with noble gases such as xenon. These lamps produce light across a broad spectrum with several strong peaks in the ultraviolet range and the spectrum is filtered to select a single spectral line at 436 nm ("g-line"), 405 nm ("h-line") and 365 nm ("i-line"). In order to continued advance of Moore's Law the semiconductor industry's need both higher resolution (to produce denser and faster chips) and higher throughput (for lower costs), the lamp-based lithography tools were no longer able to meet the industry's high-end requirements. This problem has been fixed when excimer laser lithography was proposed and demonstrated at I.B.M. [8, 9] and now excimer laser lithography machines (steppers and scanners) are the primary tools used worldwide in microelectronics production.

The commonly used deep ultraviolet excimer lasers in lithography systems are the krypton fluoride laser at 248 nm wavelength and the argon fluoride laser at 193 nm wavelength. Optical lithography has been extended to feature sizes below 50 nm using the 193 nm ArF excimer laser and liquid immersion techniques. In the last decade lasers

have been used to indirectly generate non-coherent extreme UV (EUV) light at 13.5 nm for extreme ultraviolet lithography. The EUV light is not emitted by the laser, but rather by a tin or xenon plasma which is excited by an eximer laser. Fabrication of feature sizes of 10 nm has been demonstrated in production environments, but not yet at rates needed for commercialization.



Figure 6.5. Mask Aligner Karl Suss MA160. The machine is contained in the CNR-IMM labs.

6.5. - Etching.

The *etching* processes are used in micro and nano fabrication in order to remove layers from the surface of a wafer during manufacturing. Etching is a critically important process module, and every wafer undergoes many etching steps before it is complete. In most of the processes etching steps, part of the wafer is protected from the etchant by a "masking" material which resists etching. the masking material can be a photoresist, a metal or other depending on how you want the mask durable.

Etching methods can be divided into two main branches: *wet etching* and *dry etching* processes. Wet etching processes make use of liquid-phase ("wet") etchants: the wafer are immersed in a bath of etchant, which must be agitated to achieve good process control. Different specialized etchants can be used to characterize the surface etched; for instance, buffered hydrofluoric acid (BHF) is used commonly to etch silicon dioxide over a silicon substrate. The wet etchants are usually isotropic, which leads to large bias when etching thick films and they also require the disposal of large amounts of toxic waste; for these reasons, they are seldom used in state-of-the-art processes. In contrast with the wet etching dry etching do not use "wet" reagents; typically dry etching refers to removal of material by exposing the material to a bombardment of ions (usually a plasma of reactive gases such as fluorocarbons, oxygen, chlorine, boron trichloride; sometimes with addition of nitrogen, argon, helium and other gases) that eject portions of the material from the exposed surface. A common type of dry etching is "for example" *reactive-ion etching*. Unlike with many of the wet chemical etchants used in wet etching, the dry etching process typically etches directionally or anisotropically; for this attribute dry etching is widely used, in conjunction with photolithographic techniques, in semiconductor manufacturing, where predominantly vertical sides are desired. Furthermore, dry etching processes are particularly useful for materials and semiconductors which are chemically resistant and could not be wet etched, such as silicon carbide or gallium nitride [10, 12].

6.6. - Electron beam lithography.

The electron beam lithography (e-beam lithography or EBL) is the method which uses a focused beam of electron to draw custom shapes on a surface covered with an electron sensitive film called e-resist. The electron beam changes the solubility of the e-resist, enabling selective removal of either the exposed or non-exposed regions of the resist by immersing it in a solvent. The purpose is to create very small structures in the resist that can subsequently be transferred to the substrate material with other processes. This

type of photolithography has the main advantage of obtain high resolution (can reach sub-10 nm precision) with cheap cost because the EBL don't use physical masks: the desired geometries are imprinted to the e-resist by the use of a software.

The electrons may be emitted from a conducting material either by heating it to the point where the electrons have sufficient energy to overcome the work function barrier of the conductor (thermionic sources) or by applying an electric field sufficiently strong that they tunnel through the barrier (field emission sources). Three key parameters of the source are the virtual source size, its brightness (expressed in amperes per square centimeter per steradian), and the energy spread of the emitted electrons (measured in electron volts). Lower-resolution systems use thermionic sources, which are usually formed from lanthanum hexaboride. However, systems with higher-resolution requirements need to use field electron emission sources, such as heated W/ZrO₂ for lower energy spread and enhanced brightness. Electrons can be focused either by electrostatic forces or magnetic forces through *electron lenses*. Although electron lenses in principle behave the same as optical lenses, there are differences; generally, it can be said that electrostatic lenses have more aberrations and so are not used for fine focusing [11, 12].

The most common e-resist using in EBL is Polymethyl methacrylate (PMMA), also known as acrylic or acrylic glass as well as by the trade names Plexiglas, is a transparent thermoplastic also used in sheet form as a lightweight or shatter-resistant alternative to glass. The same material can be utilized as a casting resin, in inks and coatings, and has many other uses.

The following formula gives the main parameter for an EBL exposure: the area dose given for each dot of your geometry:

$$Area\ Dose = \frac{Beam\ Current \times Area\ Dwell\ Time}{Step\ Size \times Line\ Spacing} \quad (2.6)$$

Where the beam current is given by the electron source, the step size and the line spacing provides the step of the stage movement respectively for each dot and in line, and the *area dwell time* is the time to expose each point of the geometry. For example, for an area with a beam current of 110 pA and dwell time of 4×10^{-4} s it takes $14.5 \mu\text{C}/\text{cm}^2$ for each point. The time is a serious limitation for electron beam lithography, especially when writing dense patterns over a large area: the EBL is about 10 million times slower than current optical lithography and this does not make it efficient for industry applications.

Even if the EBL tools are capable of forming extremely fine probes, things become more complex when the electrons hit the workpiece. As the electrons penetrate the resist, they experience many small angle scattering events called *forward scattering*, which tend to broaden the initial beam diameter. As the electrons penetrate

through the resist into the substrate, they occasionally undergo large angle scattering events: *backscattering*. In the forward scattering the effective increased beam diameter is given empirically by the formula $df = 0.9(R_t/V_b)$ where R_t is the resist thickness in nanometers and V_b is the beam voltage in kilovolts; such phenomenon is minimized by using the thinnest possible resist and the highest available accelerating voltage. The backscattering electrons may return back through the resist at a significant distance from the incident beam, causing additional resist exposure. This is called the electron beam *proximity effect*. The range of the electrons (defined as the distance a typical electron travels in the bulk material before losing all its energy) depends on both the energy of the primary electrons and the type of substrate. When the primary electrons slow down, much of their energy is dissipated in the form of *secondary electrons* with energies from 2 to 50 eV. They are responsible for the bulk of the actual resist exposure process. Since their range in e-resist is only a few nanometers, they contribute little to the proximity effect. A small fraction of secondary electrons may have significant energies, approximately 1 keV. They are called *fast secondaries* and can contribute to the proximity effect in the range of a few tenths of a micron.

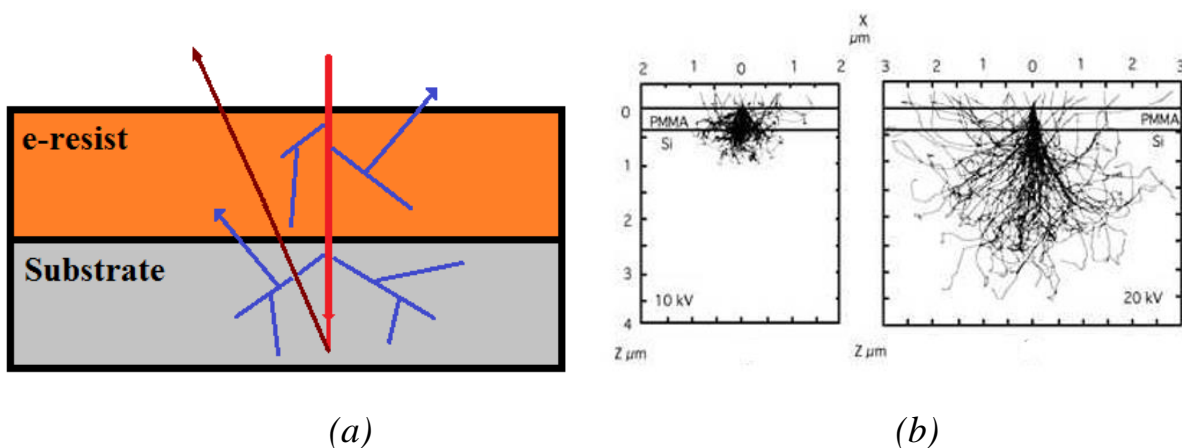
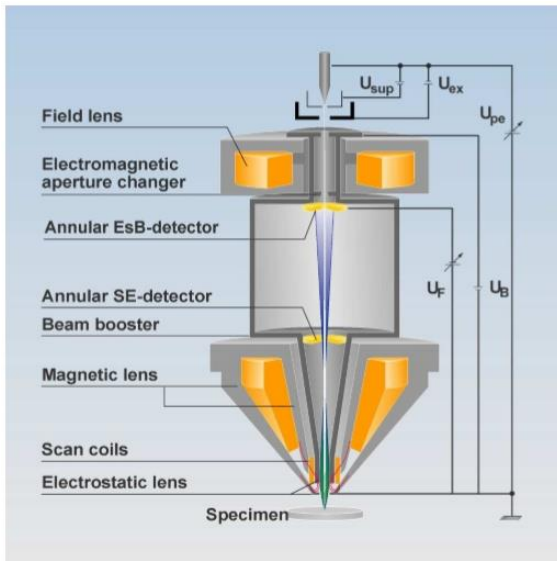


Figure 6.6. (a) Electron trajectories in e-resist: An incident electron (red) produces secondary electrons (blue); the incident electron may itself be backscattered as shown here and leave the surface of the resist (purple). (b) Monte Carlo simulation of electron scattering in PMMA on a silicon substrate at 10 KeV and 20 KeV [48].

The proximity effect is the major problem for patterning desired geometries especially when we want to go below 25nm lines and spaces: the range of secondary electron scattering is quite far, sometimes exceeding 100nm [11, 12] but becoming very significant below 20nm. So for example, narrow line between two large exposed areas may receive so many scattered electrons that it can actually develop away (in positive resist) while a small isolated feature may lose so much of its dose due to scattering that it develops incompletely. Many techniques have been developed in order to minimize the proximity effect; the most common are: the *dose modulation* where each individual shape in the pattern is assigned a dose as to (in theory) the shape prints at its correct size and the *pattern biasing* where the extra dose that dense patterns receive is compensated for by slightly reducing their size. Generally, the cad of the

structure is engineered with the techniques of proximity correction until getting the desired design.

Part of my PhD work, in order to make the synthesis of devices with size less than $1\mu\text{m}$, was the characterization and optimization of the Elphy Quantum EBL module, integrated in a FESEM Zeiss Auriga located in the La Sapienza's C.N.I.S laboratory. In section 7 is reported this aspect of my work.



(a)

(b)

Figure 6.7. (a)Electron optical setup of the Zeiss Gemini column optimized for low energy electrons. (b) FESEM Zeiss Auriga model located in the La Sapienza's C.N.I.S laboratory.

6.7. - References.

- [1] LE. Scriven, "Physics and applications of dip coating and spin coating". MRS proceedings. 121, (1988).
- [2] R. C. Jaeger. "Film Deposition". Introduction to Microelectronic Fabrication (2nd ed.). Upper Saddle River: Prentice Hall. ISBN 0-201-44494-1, (2002).
- [3] Mattox, Donald M. "The Foundations of Vacuum Coating Technology". Noyes Publications ISBN 0-8155-1495-6, (2003).
- [4] R. Behrisch (ed.). "Sputtering by Particle bombardment". Springer, Berlin. ISBN 978-3-540-10521-3, (1981).
- [5] P. Sigmund, "Mechanisms and theory of physical sputtering by particle impact". Nucl. Instr. Meth. Phys. Res. B (1987).
- [6] J. F. Ziegler, Et al. "The Stopping and Range of Ions in Solids," vol. 1 of series Stopping and Ranges of Ions in Matter". Pergamon Press, New York. ISBN 978-0-08-021603-4, (1984).
- [7] H. Dimigen, H. Lüthje. "The influence of the target material on sputter etching processes". Thin Solid Films, vol. 27, is. 1, (1975).
- [8] K. Jain. "Excimer Laser Lithography", SPIE Press, Bellingham, WA, (1990).
- [9] D. Basting, et al. "Historical Review of Excimer Laser Development," in "Excimer Laser Technology", Eds. Springer, 2005.
- [10] P.R. Choudhury. "Handbook of Microlithography, Micromachining and Microfabrication" SPIE Press Monograph PM 39.
- [11] G.R. Brewer. "Electron-Beam Technology in Microelectronic Fabrication" McGraw Hill, (1980).
- [12] S. Cabrini and S. Hawata. "Nanofabrication Handbook". CRC Press, (2012).

Chapter 7. – Nano and micro manufacturing.

In this section is introduced the manufacturing work. My first approach with the nano fabrication field had its origin in the context of realization of the devices studied in chapter 4: a single slit with chirped grating; the main goal is prove the quality of the calculation method for the design of these new type of plasmonic gold devices. The slit aperture with chirped grating is a part of a larger project whose main purpose is to create new optical electro-optic components in order to obtain electronic calculators, more integrable, cheaper and faster than the classical devices.

7.1. - Fabrication of gold nano slit apertures with chirped grating.

The device is designed with the width of the slit aperture of 90nm and it was made in gold with a thickness of 150nm on a glass substrate. The nano gold chirped grating it's located very next to the slit aperture, on the gold film, with the thickness of 50nm and it can be described with the following function:

$$y = \frac{1}{2} \left[1 + \text{sign} \left(\sin \left\{ \Phi + \frac{2\pi}{M} \cdot \ln \left[\left| 1 + \frac{M}{T_0} \left(x - \frac{g}{2} \right) \right| \right] \right\} \right) \right] \quad (7.1)$$

by the following parameters: $T_0 = 150\text{nm}$, $M = 0.0539$, $\Phi = 0.187\pi$ and $g = 90\text{nm}$; a 3D view of the device and a schematic vertical sizing is shown in figure 7.1

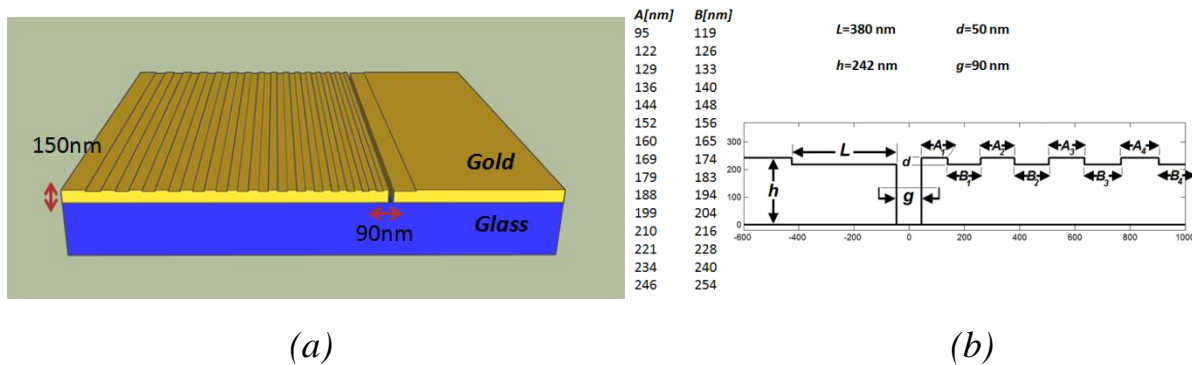


Figure 7.1.(a) 3D view of the devices: the substrate is glass while the body of the structure is gold. (b) schematic vertical sizing of the slit aperture with chirped grating made following the design rules reported of formula (7.1).

The device was originally designed in order to work with a laser source with 830nm of wavelength which impinging the structure from the glass film and through the interaction of the TM modes with the nano gold walls (who create a mirrors effects) return a desired e.g. beam from the aperture's output (figure 7.2).

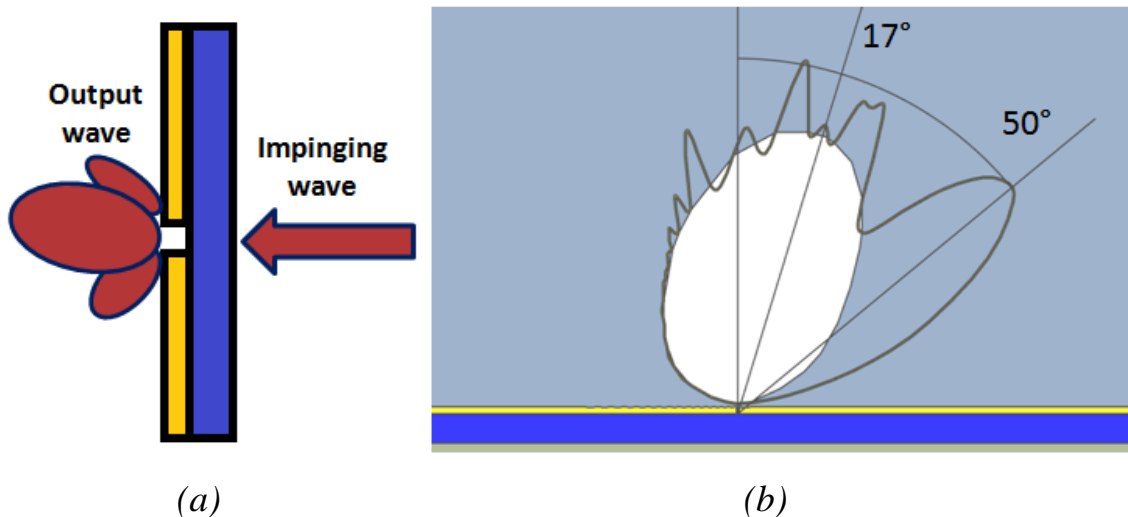


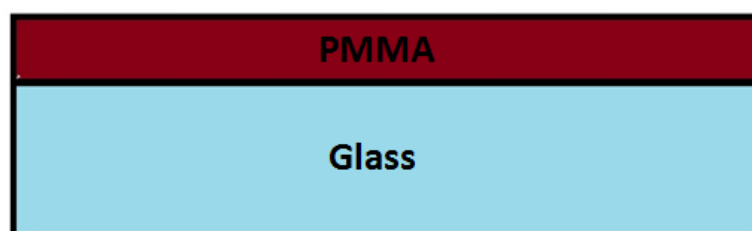
Figure 7.2. (a) 2D schematic view of device operation: the wave impinging the glass substrate and comes out from the slit aperture. (b) The predicted output beam made by the calculation method presented in section 4.

During the first part of my PhD I have worked in order to find the optimal fabrication process flow for achieving the closest structure than those presented in this subsection. Therefore, in the subsections 7.2 - 7.5 are reported the methods used to manufacture a gold grating on a 50nm gold film that is the first step for the realization of the entire device; at the end of this work the grating is ready for the characterization process.

7.2. - Fabrication of gold nano slit apertures with chirped grating: fabrication process flow.

For the manufacture of the entire device I followed the classical methods used in micro-fabrication (chapter 6) in top down approach, adjusting them for the nano resolution. Here are reported the 2D fabrication process flow for the single gold slit aperture and for the gold grating.

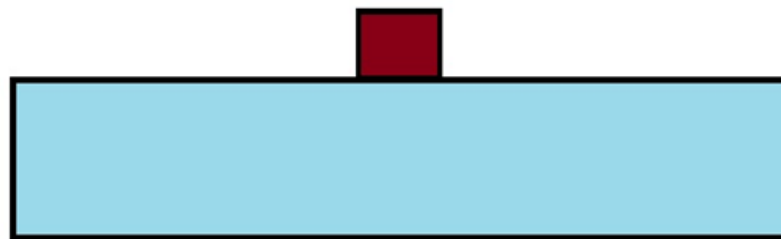
- Step 1: deposition of PMMA positive e-resist on the glass substrate by use of spin-coating and hot-plate.



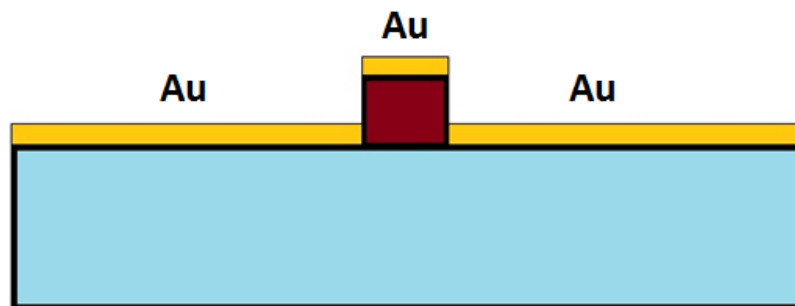
- Step 2: electron beam lithography process. I must choose this process because the EBL can guarantee resolution of 50 – 100nm.



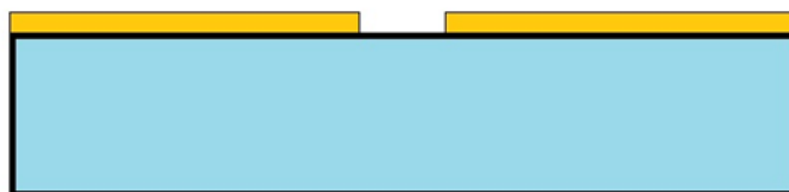
- Step 3: e-resist develop and stopping process.



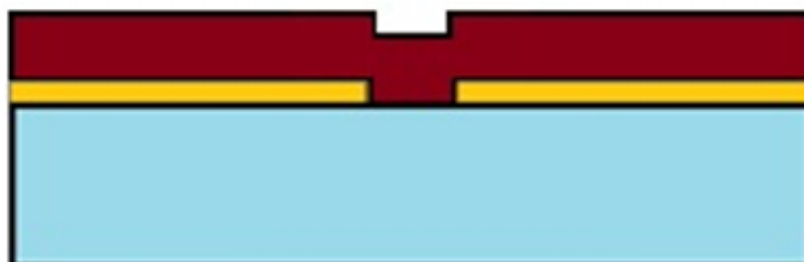
- Step 4: gold deposition by vacuum evaporator.



- Step 5: removing residual e-resist by using acetone.



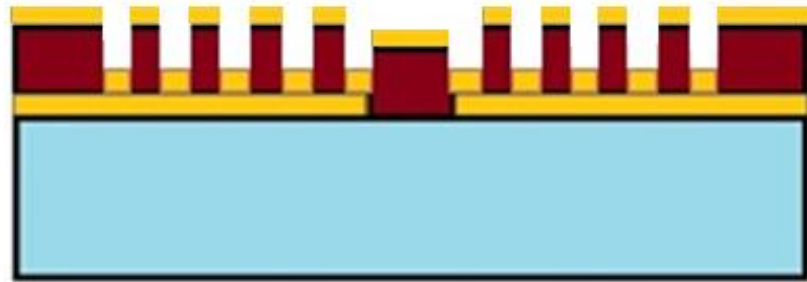
- Step 6: second deposition of PMMA on the device by spin-coating and hot-plate.



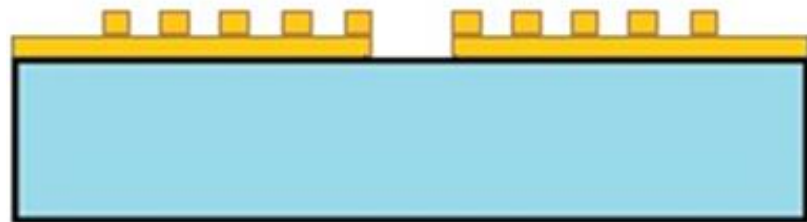
- Step 7, 8: EBL process and develop/stop of the e-resist.



- Step 9: gold deposition by vacuum evaporator.



- Step 10: remove of the e-resist residual by acetone. After this process the device is ready to be characterized.



This kind of methods which use a resist as a stencil for the deposition of the other materials on the substrate is commonly called *lift-off*; I choose lift off because it guaranteed the best uniformity and resolution for the deposition of materials which is a fundamental requirement if you want to nano manufacture. The key parameter for lift-off is the aspect ratio between the resist thickness and the material want to deposit, it must be 3:1; this because the resist remover must be able to penetrate and take all excess material off.

As already mentioned in the previous subsection I firstly prefer to fabricate the gold grating in order to evaluate the goodness and the limits of the fabrication process flow and after the characterization of this component I will proceed to the fabrication of the complete device.

It is clear, in the process flow, that the main method for my nano fabrication approach is the EBL: through the EBL process we can obtain the PMMA stencil upon which we can draw our nanostructures; so, intense part of my PhD work was aimed at

studying EBL instrument with the PMMA e-resist, in order to find the best working condition for my purposes.

7.3. - EBL study and characterization.

For the EBL process I could make use of FESEM Zeiss Auriga (subsection 6.6) which has three main functions:

- Scanning electron microscope (SEM) (resolution 1nm).
- Focused ion beam (FIB), (resolution 7nm).
- The electron beam lithography, (nominal resolution 40nm).

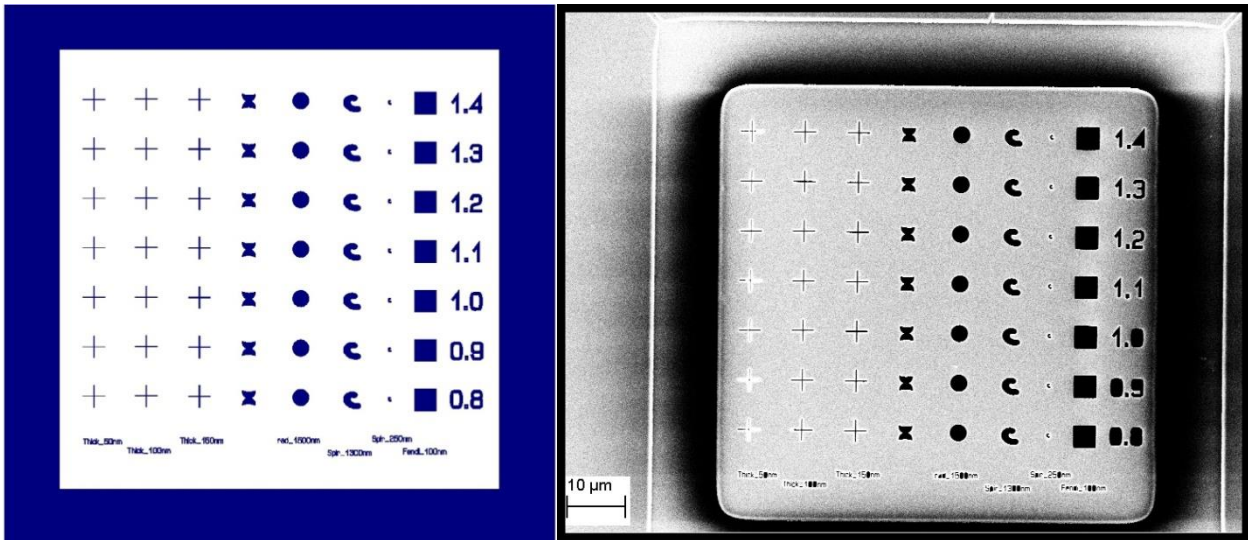
In particular for the EBL I have four main parameters; by varying those specification we can reach the best writing resolution:

- I. *Working distance*: the distance in which the electron beam is performed from the sample.
- II. *EHT*: namely the voltage difference in KeV on which works the electron beam.
- III. *Area Dose*: the electron beam dose for each single writing area (subsection 6.6) the measurement unit is $\mu\text{C}/\text{cm}^2$.
- IV. The development time: i.e. the time in which the sample is immersed into the developing solution.

Another important factor that an EBL's technologist must consider very seriously is the aspect ratio between the e-resist thickness and the geometry to be printed on the sample: generally a good aspect ratio is 3:1 or below. For instance if the minimal dimension of the mask CAD is 100nm the thickness of the e-resist for a good EBL writing can be at most 300nm.

Finally, for the EBL process it is necessary that under the e-resist there is a conductive material; this is due to the intrinsic nature of the method: the geometry transfers to the e-resist thanks the trajectory of the electron inside the polymer; when the electron reaches the substrate under the e-resist it must be able to finish its own path and discharges away. If under the e-resist we have an electrical insulator material the electron remain trapped and the final geometry is blurry due to the increase of the proximity effect (subsection 6.6).

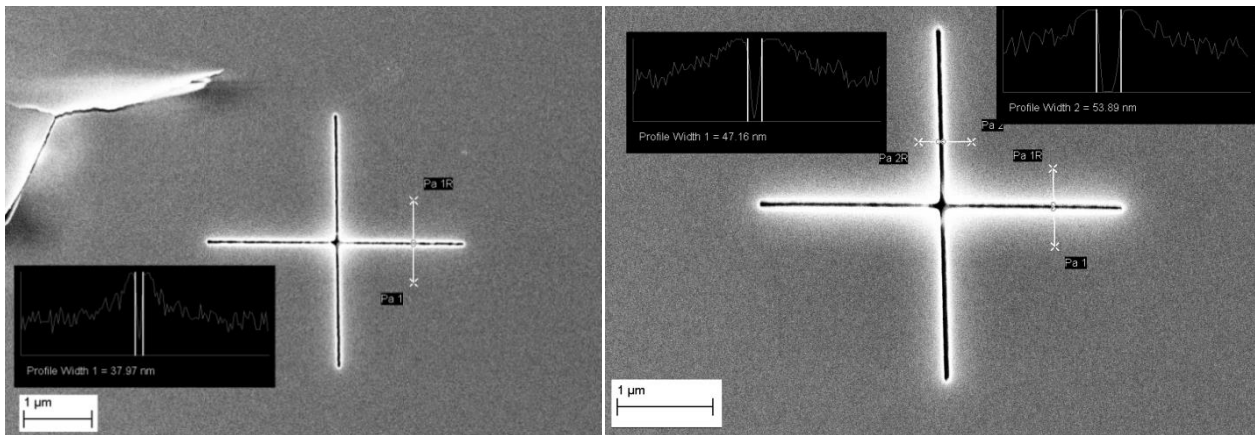
In figures 7.3 and 7.4 it is reported an example of EBL writing, on a PMMA of $1.6\mu\text{m}$ thick, with different geometries; varying the area dose value between 900 and $3690\mu\text{C}/\text{cm}^2$.



(a)

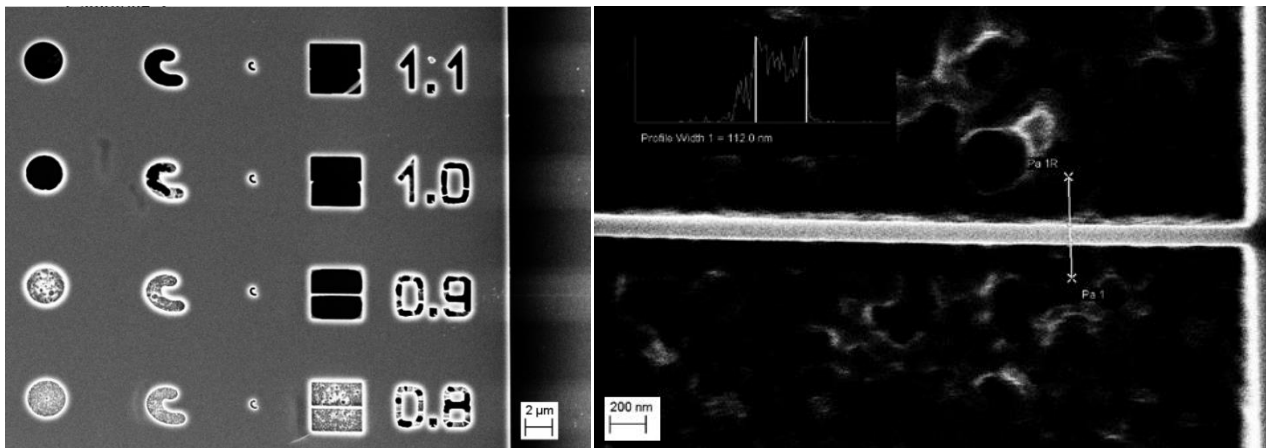
(b)

Figure 7.3. (a)the CAD use for the EBL mask: there are 8 different geometries and the area dose value change in each line is multiplied by the number indicated on the right. (b)General vision of the area after the EBL processes on 1.6µm thick PMMA.



(c)

(d)



(e)

(f)

Figure 7.4. Particular of the different geometries of figure 7.3: (a-d)changing the area dose values it varies the definition and the size of the crosses. (e, f) Different geometries all have one different area dose value that makes them clearly defined.

It is clear that for each geometry corresponds a different area dose optimal value in order to obtain a correct imprint to the PMMA. The task of an EBL technician is to engineer the EBL mask in order to find the most suitable value for each type of geometry in relation to the e-resist thickness. In table 7.1 are reported the EBL parameter used for the example of figures 7.3 – 7.4.

EHT	30 KeV
Diaphragm	15μm
Working distance	6mm
Step size	6nm
Line space	6nm
Beam current	73 pA
Area dose	900μC/cm²

Table 7.1 EBL parameters used for the example show in figures 7.3 – 7.4.

For the lift-off process I need an high aspect ratio between the PMMA and the EBL mask so I actualize a statistic process flow with the purpose to find the best working conditions for my project (subsection 7.2).

7.4. - Dose influence on the PMMA e-Resist for the development of high-aspect ratio and reproducible nanostructures by Electron Beam Lithography.

7.4.I. - Introduction.

The dramatic development of the nanotechnologies during the last ten years has requested rapid advances in the nanofabrication for the submicron regime, and especially for the so-called top-down technique, where the pattern transfer happens at the nanometer scale (e.g. 100 nm). Electron Beam Lithography (EBL) results to be one of the most used technique for obtaining nanostructures down to sub 10nm, using different strategies such e-resist development processed with cold developers (4-10°C) or through a double layer resist system consisted in a 15 nm thick Chromium mask [1, 2, 3].

Nevertheless, it exists also other different techniques for reaching this aim, as, for example, the immersion lithography, able to increase the resolution of classical deep UV lithography down to 20 nm using excimer lasers with wavelengths of 193 and 248 nm[4, 5], the nano imprinting lithography (NIL) that creates patterns by mechanical deformation of imprint resist and subsequent processes[6, 7, 8], or the Focused Ion Beam (FIB) Lithography [9, 10].

However, the Electron Beam Lithography (EBL) maintains yet its leading role, because of its possibility to exist as stand-alone devices or integrated in a normal electron microscope, equipped with a beam blanker [11, 12]. Besides, EBL allows to obtain microsystems or nanostructures with high resolution, high reliability in processing, high accuracy in positioning/alignment, and high flexibility in pattern

replication [13, 14]. These features are such that EBL has been used in different research areas like metamaterials and nanophotonic structures [4, 8, 15, 16], microfluidic devices [17, 18] and even in Bioscience and Medical field [19, 20].

Generally, in nano-fabrication field, the EBL plays a fundamental part in the lift-off technique, together with the use of the Poly-Methyl-Methacrylate (PMMA), or with the assistance of other materials [21, 22, 23]. The PMMA is the most common positive e-resist used for the EBL, and this is due for its flexibility and other well known features [11], as well for its possibility to reach high resolution [24, 25, 26]. As rule of thumb, the choice of the resist thickness should be done considering that the final aspect ratio of the wanted nanostructure should be less than three times the thickness of material to be deposited on the substrate [12, 27]. So, the main goal is to push the working limits of thick PMMA towards high aspect ratio, in order to have just a single layer of positive resist for different application in micro and nano-fabrication field, like, for example, the use of a single PMMA layer as sacrificial mask in a lift-off technique.

In this chapter we present a statistic process control on 1.6 μm thick PMMA AR-P 672 (Allresist, Germany), performed with an Raith Elphy Quantum EBL module, inspecting the quantity of electric charge per squared centimeters used to expose the e-resist, normally defined as Area Dose, for the formation of curved lines with different dimensions. At the end of this study we have obtained an aspect ratio of 4:1 between e-resist thickness and the CAD structures dimensions with an Area Dose windows range comprised between 500 and 1050 $\mu\text{C}/\text{cm}^2$.

7.4.II. - Material & methods.

The substrate used for this chapter has been a standard electronic grade wafer silicon <100> from (MEMC Electronic Material Spa) while the e-resist is the PMMA AR-P 672.08 (All-Resist-de, Germany). The e-resist is deposited by Spin-Coating WS-650-23B (Laurell Technologies Corporation), with the following operating conditions: 300 rpm for 5 s, followed by 2000 rpm for 45 s and hot plate baking at 170°C for 5 minutes; the final thickness obtained is 1.6 μm . The PMMA has been characterized using the Atomic Force Microscopy (Icon, Veeco), whose results are reported in Figure 7.5.1.

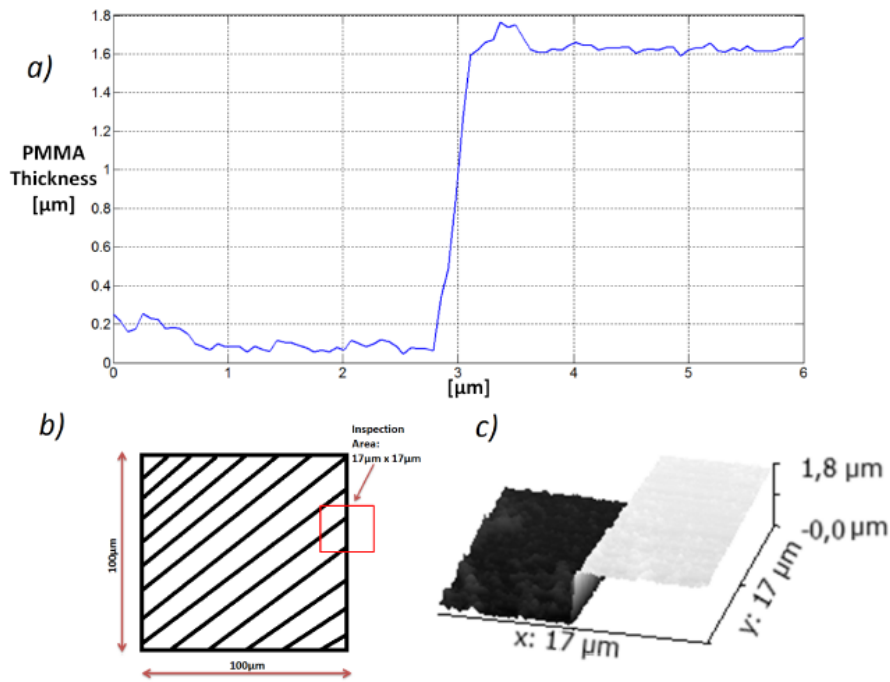


Figure 7.5.1. a) Line profile of the PMMA thickness obtained by Atomic Force Microscopy (AFM); b) dimensions of the inspected area; c) 3D image of the thickness variation inside the area of 17 μm x 17 μm chosen for the measurement.

The Electron Beam Lithography has been performed using an Elphy Quantum EBL module, integrated in a FESEM Zeiss Auriga instrument, writing in longitudinal area mode. The patterned structure has been obtained through a CAD consisting of curved lines with different width and has been made with Raith GDSII v1.1 and reported in figure 7.5.2. The choice of this kind of geometry has been made considering the need to study the performance of the instrument on both linear and curvilinear elements, and to examine the interaction of the elements at different distances. The development phase has been performed using a Methyl Isobutyl Ketone (MIBK) solution diluted with Isopropyl Alcohol (IPA) in relation 1:3 for 75 s and then placed in a pure IPA solution for 30 s. The patterned wafers have been analyzed with the Electron Microscopy. In order to prevent a deep variation on the morphology, caused by a direct contact between the unexposed e-resist and the electron beam, all the exposed and developed sample have been coated with a 20 nm Chromium layer using a metal sputter (Quorum Q150T). Then, all the images have been analyzed using Image J software to build up a Statistic Control with numerical methods in Matlab environment, so to obtain a direct correlation between the effective dimension of the printed structures with the area dose value set of the EBL instrument.

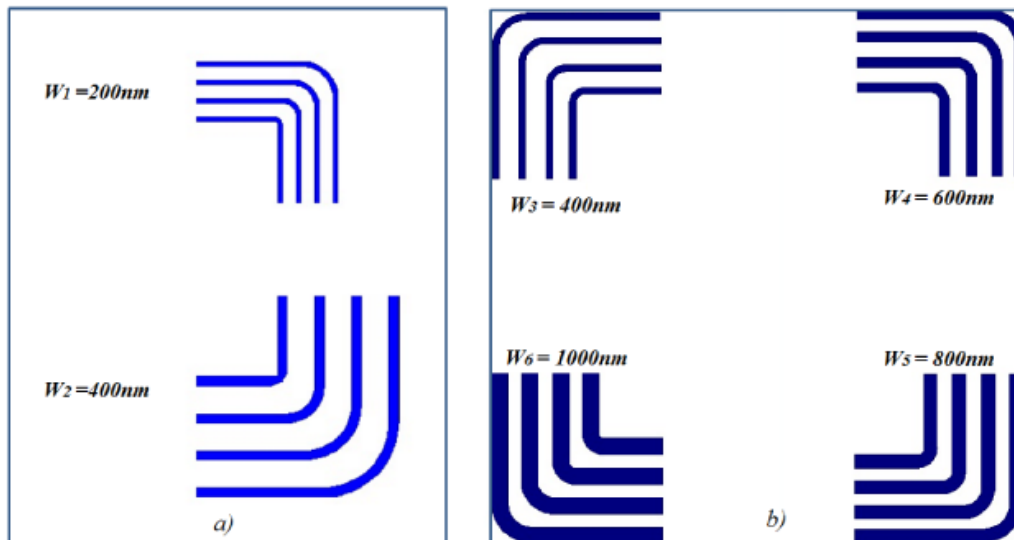


Figure 7.5.2 . a) CAD used for the to the first writing cycle, having structures with width of 200 nm (W1) and 400 nm (W2); b) CAD used during the second writing cycle with width that changes from 400 to 1000 nm. The width and the curvature radius of the structures showed in figure have the same dimensions.

7.4.III. – Results & discussion.

In order to obtain a a repeatable process window for an EBL writing process, a first writing session has been performed, taking as reference structure, the one showed in figure 7.5.2a, and analyzing a wide range of dose, repeated with a 50 increasing dose steps. The performing parameters are reported in Tab. 1, where:

- The working distance is the distance between the sample and the electronic gun.
- The dwell time is the time that electronic beam remains fixed in a single point.
- The step size is the distance along the x axis between two points written by the EBL.
- The line spacing is the distance along the y axis between two points written by the EBL.
- The area dose is the quantity of electric charge per squared centimeters used to expose the e-resist.

TABLE 7.4.1. : EBL parameter for the writings cycle.

	First Writing Cycle	Second Writing Cycle
Acceleration Voltage	30 keV	30 keV
Working Distance	6 mm	6 mm
Beam Current	71.4 pA	85.4 pA
Dwell Time	0.002 ms	0.0033 ms
Step Size	6 nm	6nm
Line Spacing	6 nm	6nm
Area Dose, start value	350 $\mu\text{C}/\text{cm}^2$	400 $\mu\text{C}/\text{cm}^2$
Area Dose, final value	3350 $\mu\text{C}/\text{cm}^2$	1500 $\mu\text{C}/\text{cm}^2$
Dose Steps	50	25

The SEM analysis of this first writing cycle has permitted to have a first clue value about the dose range and its repeatability. In fact, from the image analysis it has been possible to calculate the value of Normalization Deviation Standard (N-SD) for the obtained width from each group of curves (Eq. 1), that provides an information about the accuracy of the writing cycle respect the desired feature. Its known that values lower than 5%, indicates an excellent repeatability [28].

$$N - SD = \frac{\sqrt{\text{variance}}}{\text{mean value}} \quad (7.4.1)$$

Observing the graph showed in Fig. 7.5.3, and highlighted by the regression line, it's evident that we have an increase of the structure dimensions proportional with the area dose value, where the determination value is $R^2 = 0.9311$.

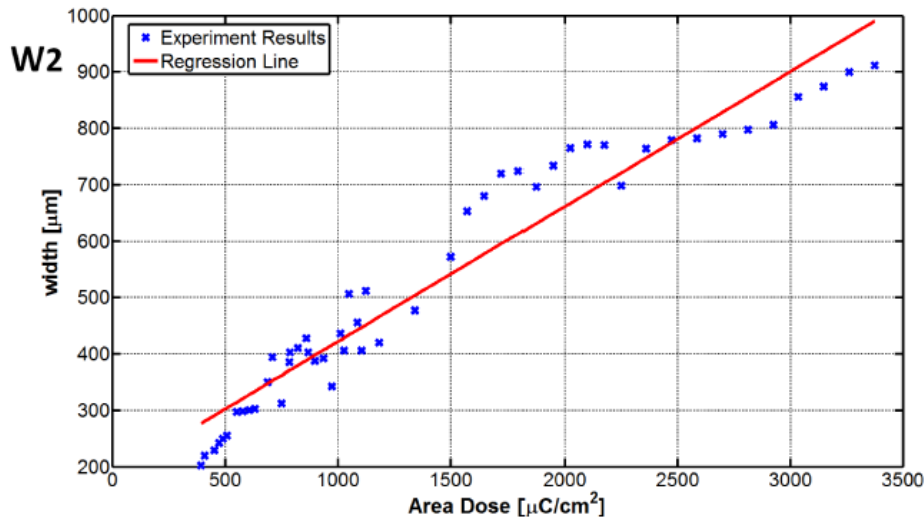


Figure 7.5.3. EBL first writing cycle result, on the x-axis are report the Area Dose value and on the y-axis the curved lines width.

Beside, from this data, it was obtained an important information about the Area Dose range (ADr) for the structures with thickness of 200 and 400 nm. Broadening the graphic around the area containing the points near the desired thickness (Figure

7.5.4), it is possible to limit the ADr with high N-SD value. These data have been calculated from the graphical analysis of the SEM images of the first writing cycle. The red line represents the expected dimension, while the green one is the mean value obtained from the imaging analysis and finally, the two dashed lines correspond to the $\pm 3\sigma$ error.

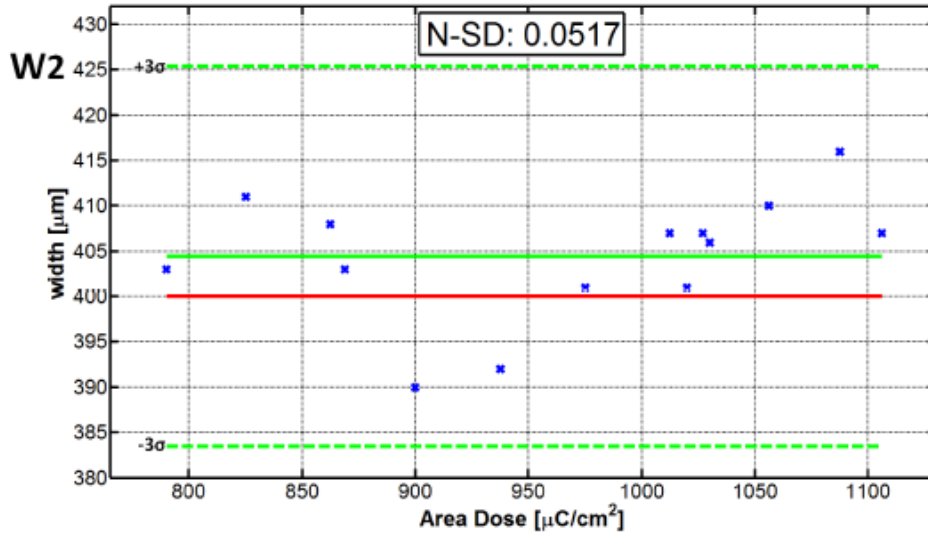


Figure 7.5.4. In the graph are reported all the experimental values of the 400 nm width structures (x) versus the Area Dose.

The results are that the ADr $869 \mu\text{C}/\text{cm}^2$ - $1106 \mu\text{C}/\text{cm}^2$, for the structure with the width of 200 nm, showed aN-SD of 12%, while for the other structures with a width of 400 nm, the ADr is $785.5 \mu\text{C}/\text{cm}^2$ - $1185 \mu\text{C}/\text{cm}^2$, with an excellent N-SD of 5.1%. The good quality of the patterning can be observed from Fig. 7.5.1a, where it is reported the AFM profile of a EBL writing. In fact, considering also the effect due to the shape of the AFM cantilever, it can be seen that the polymer walls created after the lithography has an angle close to the 88° degree. For this reason, is possible to claim that for the 400 nm structures, we have performed a good lift off process of 4:1 aspect ratio. Besides, the high N-SD value given by the 200 nm patterning, means that there are other aspects of the process, like the resist spinning, developing time and temperature, ecc. [29], that have to be carefully optimized in order to obtain more high aspect ratio.

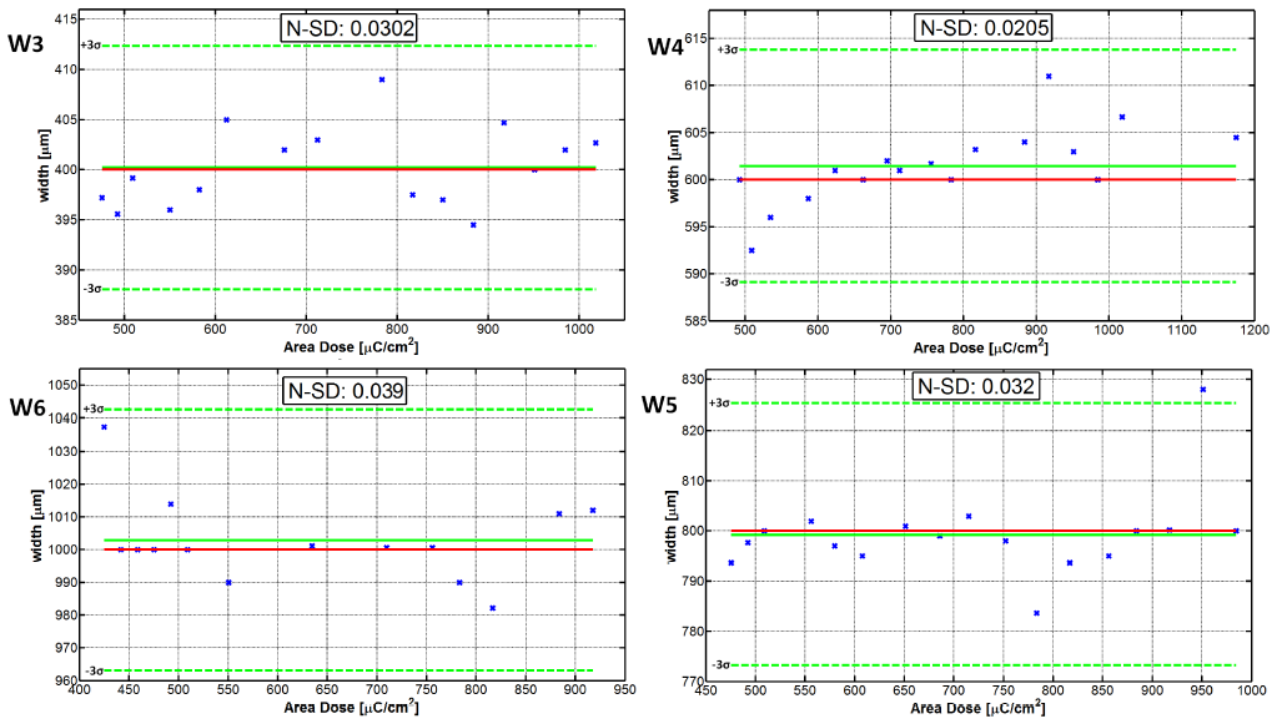


Figure 7.5.5. In the graph are reported all the experimental values of the nanostructures' width (x) versus the Area Dose.

So, after these outcomes, we have performed a second writing cycle for investigating structures with higher thickness, with the aim of acquiring, also in this case, an high reproducibility. The patterning parameters are reported in Tab. 7.4.1. The image analysis for this new writing session and the N-SD value are represented in the four graphs in Fig. 7.5.5, whose composition has been described before. It is well evident that all the elements have values all under 5%, demonstrating that these patterns are all reproducible in a wide dose range. We have also reported in Fig. 7.5.6, the SEM images for the four nanostructures obtained after the EBL process.

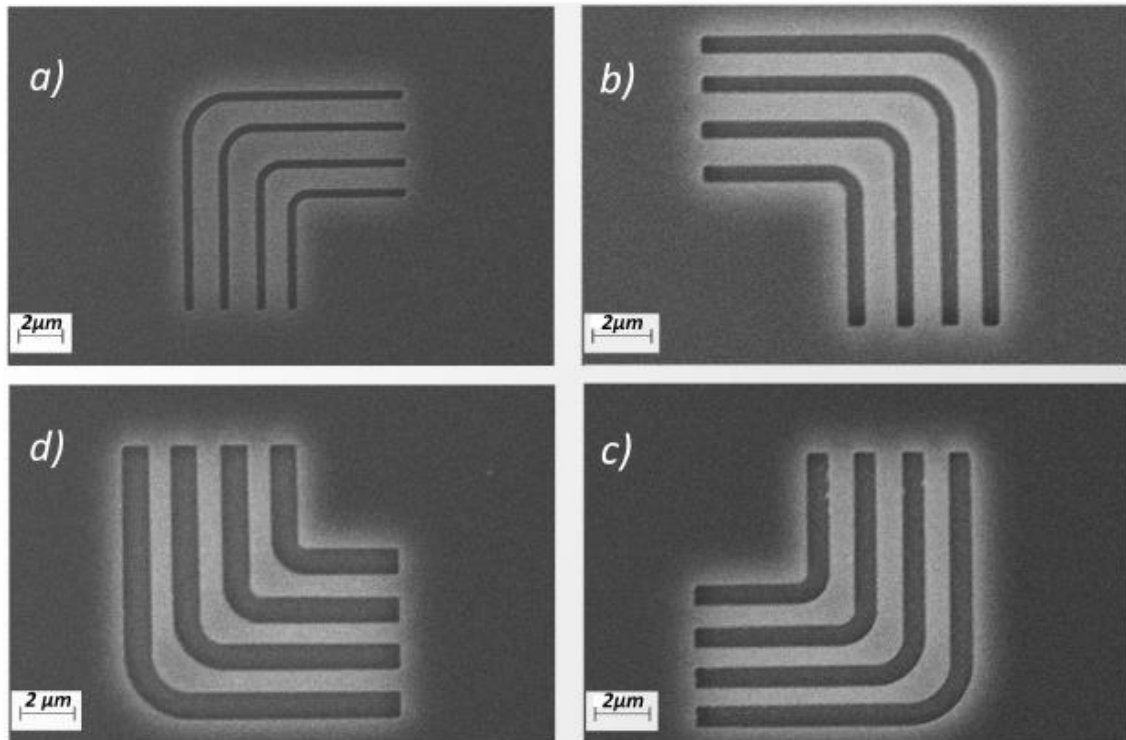


Figure 7.5.6. SEM images of the four nanostructure (W1÷ W4) obtained by EBL with a developing time of 75s. The width of the L-shape structures increase in clockwise direction from a).

It results that the complex shapes of the CAD are well reproduced, as well as the borders are quite smooth. Besides, the presence of various sub-micron structures in a small area seems not to create any problem due to the proximity effect. This fact evidence further confirms of the good quality of the process.

In electron beam lithography, together with exposure dose, one of the most influential parameter is the development time. In fact, Mohammad et al. [29] reports in their work that this parameter can affects the sensitivity of the e-resist, the exposure window and, above all, the ultimate resolution of the e-resist. For this reason, it has been necessary to investigate the same ADr with different development times, respectively, 40 s and 150 s. Looking at the graph in Figure 7.5.7, it can be observed how dramatically development time influences the reproducibility of the lithography. In fact, a lower time respect the 75 s could create underexposed resist with irregular shapes. Instead, developing with higher times, the final width can be seriously modified by the solvent, because it could attack also the unexposed areas [29].

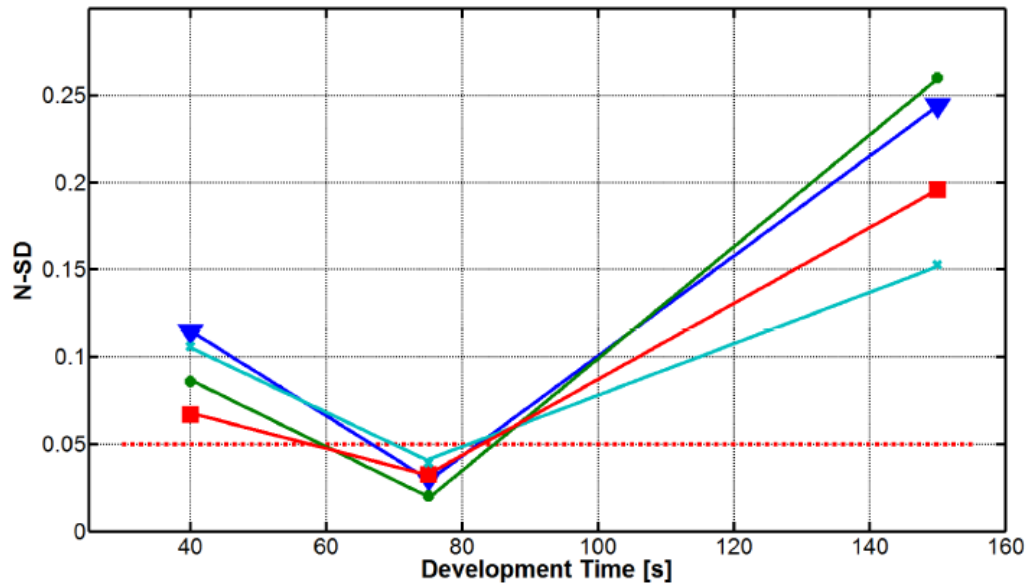


Figure 7.5.7. The values of the normalization standard deviation (N-SD) compared with the developing time for W1 (▼), W2 (●), W3 (■) and W4 (x).

7.4.IV. - Conclusion.

A deeply investigation on the writing properties for a sub-micron resolution with high aspect ratio of the PMMA AR-P 672.08 is presented in this work. Through a statistical descriptive computing performed on the SEM images of the written patterning, it has been possible to found out the optimized Area Dose range for the a repeatable lithography process (N-SD values < 5%) of sub-micrometer structures. The most important result regards the formation of 400nm width structures in PMMA of 1.6m thickness, using 75s as developing time. In fact, we have obtained a very low N-SD value (3.03%) and together with an high aspect ratio (4:1). Besides, it has been also investigated the effect of the developing time on the EBL process. We have found out that lower times lead to unexposed patterning with undefined shapes, while higher times can create uncontrolled increase of the width. This result gives us an additional confirmation that the developing time of 75s is an optimized parameter . Besides, this study can open the way to develop an high performance use of the PMMA in single layer fabrication processes.

7.4.V. - Acknowledgments.

The authors would like to thank Prof. Concita Sibilìa from Department of Basic and Applied Sciences for Engineering (BASE), Sapienza University of Rome, for her support to research.

7.5. - Fabrication of gold nano slit apertures with chirped grating: fabrication results of the gold grating.

In this subsection are reported the fabrication results of the gold grating discussed in the previous paragraphs. The structure is made by 50nm thickness of gold grating on 100nm thickness of gold substrate, for this first prototype it was decided that the width of the ridge is constantly 150nm all 600nm equidistant; in figure 7.6 is reported an a schematic 2D diagram of the device.

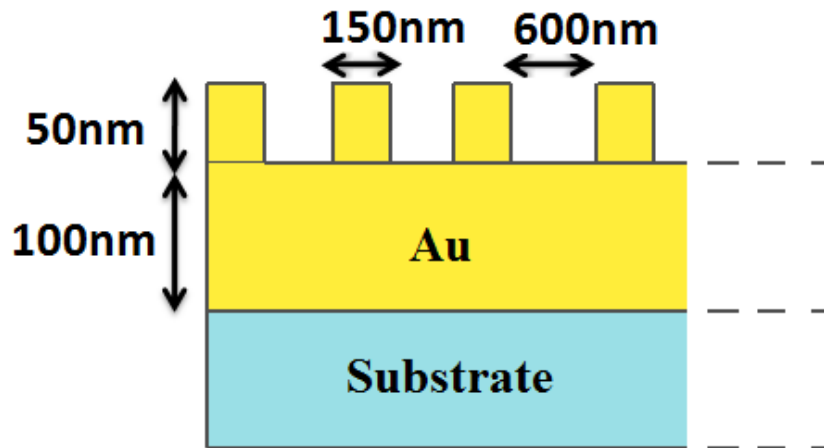
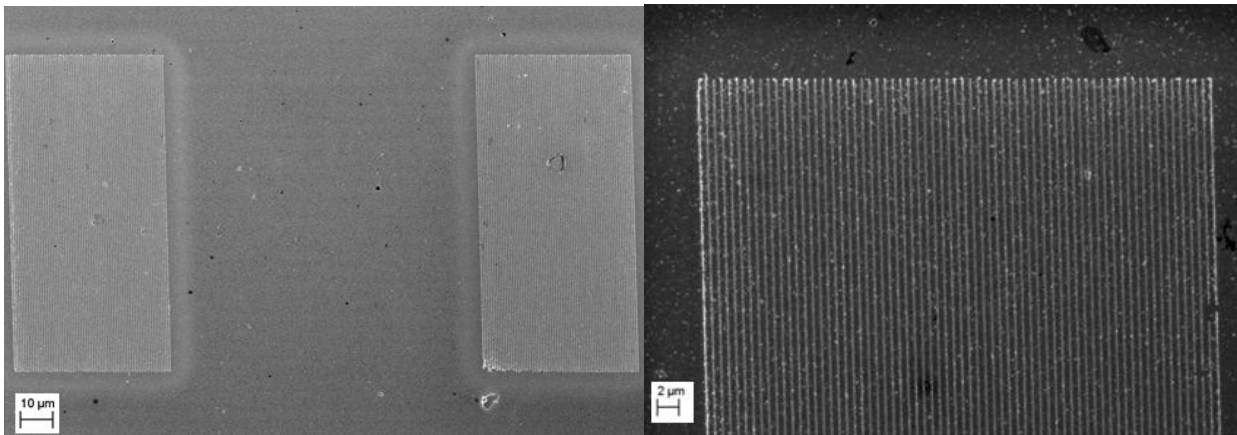


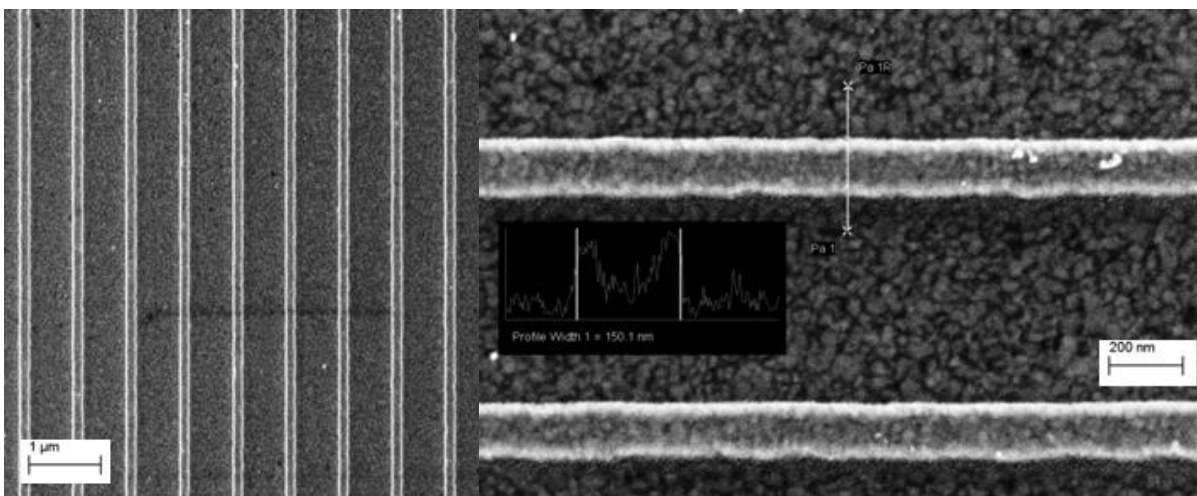
Figure 7.6.2D schematic image of the gold grating device, the 50nm of gold grating is made on 100nm gold grating film.

Following they are shown the SEM images of the gold grating fabricated with the process flow discussed in subsection 7.2; in the figure 7.7(a) is demonstrated that the structure is reproduced several times. Is therefore clear that the methods used prove to be successful in order to nano-manufacture this type of samples.



(a)

(b)



(c)

(d)

Figure 7.7. The SEM images of the final gold grating: from the image (a) to (d) there is a progressive zoom on the device details.

The device is now ready to be characterized by a laser beam system with 830nm of wavelength. After this phase it will proceed to the manufacture of the gold slit aperture and after a consecutive characterization of that to the realization of the entire device.

7.6. - Fabrication of metamaterial THz absorber.

In this final paragraph the manufacture of a metamaterial THz absorber is presented. The base cell of the device is reported in Fig. 7.11, as can be observed the dimensions of this component are extremely large compared to those of the devices manufactured in the previous subsections. For example the gold grating of sub. 7.5 cover a total area of $50\mu\text{m} \times 100\mu\text{m}$, while a single element of the absorber is $80\mu\text{m} \times 80\mu\text{m}$. A single cell is constituted by a layer of 100nm of gold (having a mirroring function) on the substrate above which it is deposited a polymer film and on top of the polymer there is another gold layer modeled as the geometries shown in Fig 7.8(a). Due to the minimum size of the device the following methods are appointed as micro-fabrication processes.

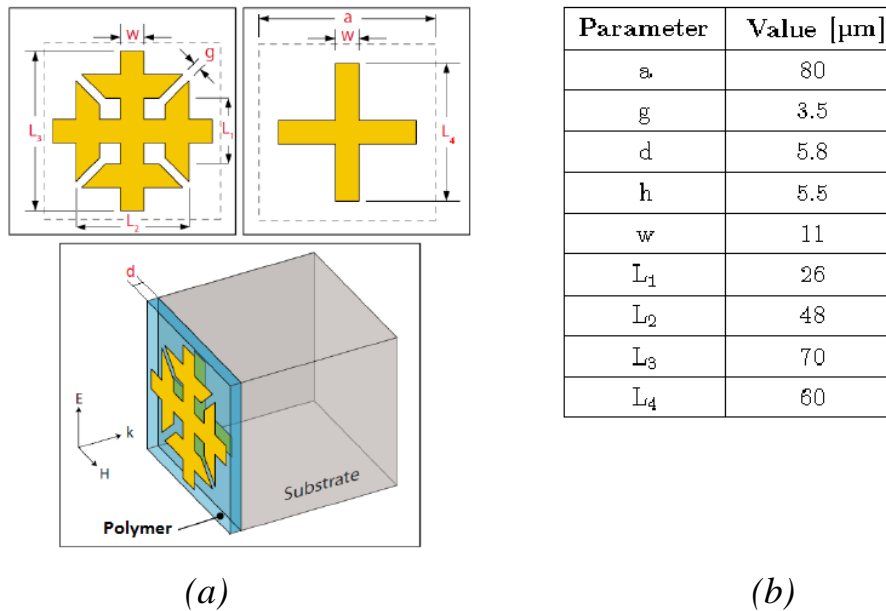
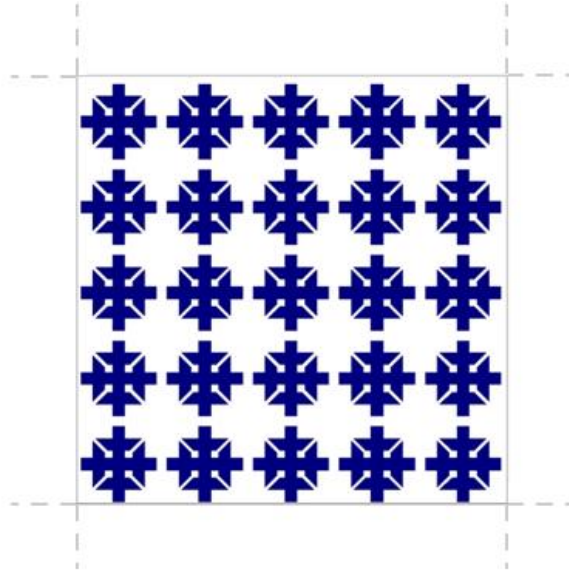


Figure 7.8. Base cell of the THz absorber: (a) 3D and 2D element design; (b) dimensions of the unit cell.

For requirements associated to the measuring system the total area of the working part of the absorber must be $6\text{cm} \times 6\text{cm}$. This constraint means that the electron beam lithography is unfit for the project: the imprint of a single cell would require a time of about one hour, covering an area of $6\text{cm} \times 6\text{cm}$ it means print about 5625 cells; so in terms of time and costs it is overmuch for the EBL.

In this context I have chosen to use the UV-lithography (Subsection 6.5) which allows to imprint a large area with one impression. This kind of method involves a loss of resolution; then, in order to obtain a perfect imprint for an area of $6\text{cm} \times 6\text{cm}$ we have redesigned the base cell of the device (Fig. 7.11(a)).

Parameter	Value [μm]
a	80
g	5.659
d	5.2
h	5.5
w	11
L_1	18
L_2	42
L_3	72

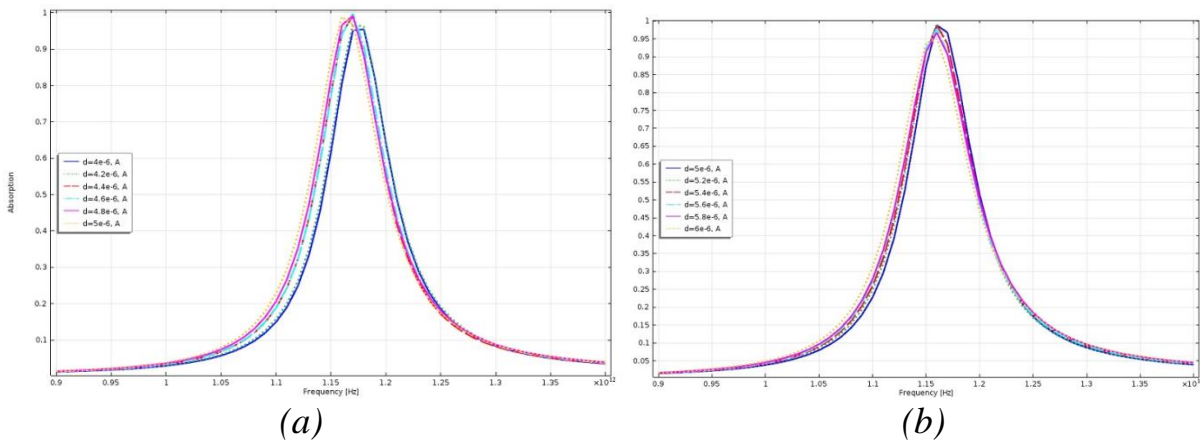


(a)

(b)

Figure 7.9. Dimension of the unit cell redesigned(a). Portion of the CAD mask used for the UV-lithography (b).

For the polymer film we have chosen the Polyimide (Appendix A.1) for its response in THz regime and its capacity to bind to metals. The thickness of the polyimide layer has been selected in connection with the absorption peak of the material (with geometries resized in Fig. 7.9) in THz frequencies simulated with COMSOL Multiphysics (Fig 7.13); At the end we have chosen $5.4\mu\text{m}$ thicknes wherein it had the best behavior.



(a)

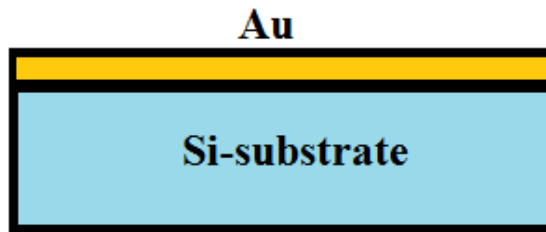
(b)

Figure 7.10. COMSOL Multiphysics simulation of the absorption peaks of the device in relation with the polyimide thickness in THz regime. In (a) the thickness varies between an initial value of $4\mu\text{m}$ to $5\mu\text{m}$; in (b) the thickness varies between $5\mu\text{m}$ to $6\mu\text{m}$.

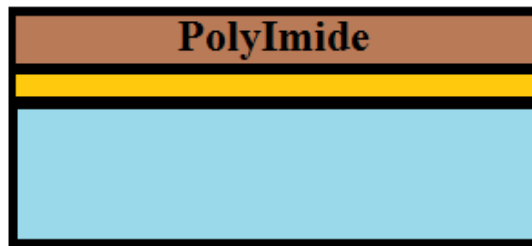
The final significant change to the initial device was the addition of 10nm chromium layer between the final gold layer and the polyimide to improve the adhesion of the gold layer. the simulations performed with regard to this variation don't show significant modifications of the absorption peaks.

Following is reported the fabrication process flow of the devices:

- Step 1: deposition of 10nm of chromium and 100nm of gold on the silicon substrate by use of vacuum evaporator.



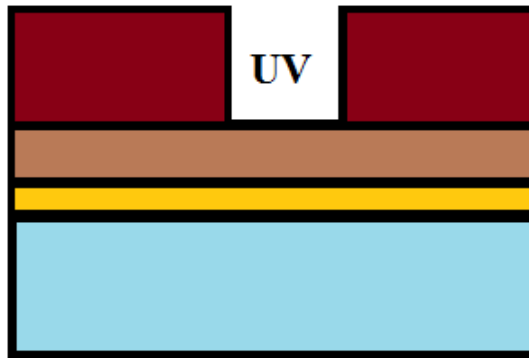
- Step 2: deposition of a 5.4 μm -thick polyimide film by spin-coating on the gold film and curing in a vacuum oven.



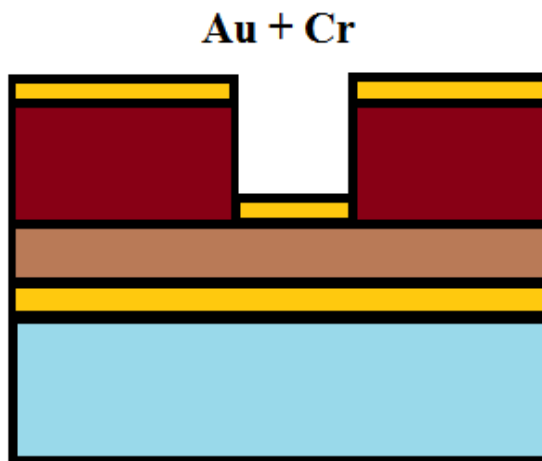
- Step 3: deposition of the UV-resist by spin-coating and hot-plate.



- Step 3/4: UV-lithography and resist development.



- Step 5: vacuum evaporation of 10nm chromium and 100nm of gold.



- Step 6: remove of the UV-resist residual by acetone.



In Fig. 7.14 the 3D schematic vision of the device after the step 8.

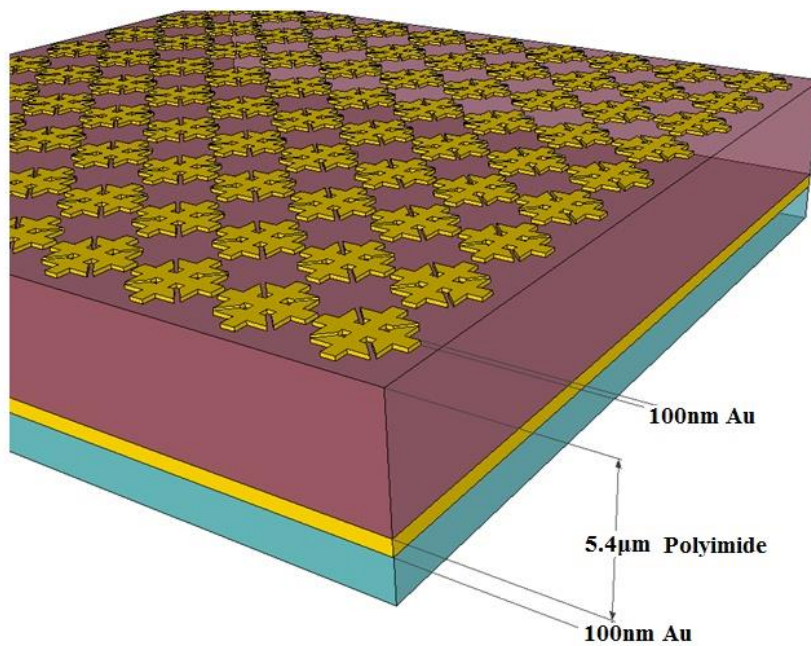


Figure 7.11. 3D view of the device after the fabrication process step 8.

Finally, below are reported the images made by an optical microscope of the finished device. The absorber is now in the characterization phase.

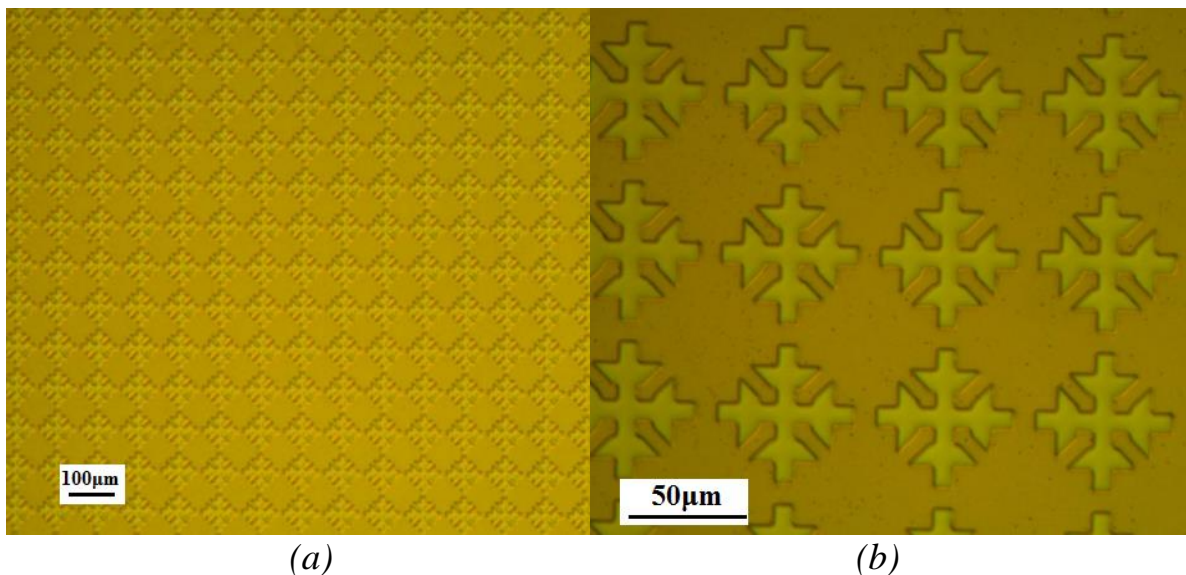


Figure 7.12. The final device, the images are made by an optical microscope. In (a), (b) there is a progressive zoom on the particulars.

7.8. - References.

- [1] W. Hu, K. Sarveswaran, and M. Lieberman, *Vac. Sci. Technol. B* 22, p. 1711 (2004).
- [2] P. Hoffmann, Et al. “Comparison of fabrication methods of sub-100nm nano-optical structures and devices,” in *Nanophotonic Materials and Systems II*, Proceedings SPIE 5925, edited by Z. Gaburro and S. Cabrini (SPIE, 2005) p. 592506.
- [3] I. Maximov, Et al. *Microelectronic Eng.* 61, 449–454 (2002).
- [4] N. Dutta, Et al. *Materials* 3, 5283–5292 (2010).
- [5] P. Dumon, Et al. *Phot. Tech. Lett. IEEE* 16, 1328 – 1330 (2004).
- [6] X. Zhao, Et al. *J. Mater. Chem.* 7, 1069 – 1074 (1997).
- [7] Y. Li, Et al. *J. Colloid & Interface Sc.* 458, 300–304 (2015).
- [8] A. Boltasseva and V. M. Shalaev, *Metamaterials* 2, 1–17 (2008).
- [9] O. Volciuc, Et al. “Fabrication of photonic crystal circuits based on gan ultrathin membranes by maskless lithography,” in *Nanotechnology VII*, Proceedings SPIE 9519, edited by I. Tiginyanu (SPIE, 2015) p. 951904.
- [10] E. Miele, Et al. *Microelectronic Eng.* 141, 51–55 (2015).
- [11] W. Smith and J. Hashemi, in *Foundations Of Materials Science and Engineering* (4. ed) (McGraw Hill, 2006) p. 509.
- [12] G.R. Brewer, in *Electron-Beam Technology in Microelectronic Fabrication* (McGraw Hill, 1980).
- [13] Y. Chen, *Microelectronic Eng.* 135, 57–72 (2015).
- [14] H. Kollmann, Et al., *Nano Lett.* 14, 4778–4784 (2014).
- [15] B. Taylor, Et al. *Opt. Express* 22, 13234–13243 (2014).
- [16] F. Domenici, Et al. “Colloids and Surfaces A: Physicochemical and Engineering Aspects”, 498, 168–175 (2016).
- [17] S. Youn, Et al. *Microelectronic Eng.* 85, 918–921 (2008).
- [18] V. Nock and R. J. Blaikie, *Microelectronic Eng.* 85, 1077–1082 (2008).
- [19] C.J. Bettinger, Et al. *Chem. Int. Ed.* 48, 5406–6415 (2009).
- [20] C. M. Kolodziej and H. D. Maynard, *Chem. Mater.* 24, 774–780 (2012).
- [21] P. Carlberg, Et al. *Microelectronic Eng.* 67/68, 203–207 (2003).
- [22] D. Tu, M. Liu, Et al. “A zep520-lor bilayer resist lift-o_ process by e-beam lithography for nanometer pattern transfer,” in *IEEE Nano 2007* (IEEE, 2007), pp. 624–627.
- [23] R. E. Howard, Et al. “A zep520-lor bilayer resist lift-o_ process by e-beam lithography for nanometer pattern transfer,” in *IEEE Transactions On Electron Devices* (IEEE, 1981) p. 1378.
- [24] A. Gangnaik, Et al. , *Microelectronic Eng.* 123, 126–130 (2014).
- [25] S. Yasin, Et al. *Appl. Phys. Lett.* 78, p. 2760 (2001).
- [26] S. P. Beaumont, Et al. *Appl. Phys. Lett* 38, p. 436 (1981).
- [27] S. Cabrini and S. Hawata, in *Nanofabrication Handbook* (CRC Press, 2012).
- [28] S. Institute Inc., *JMP11 Quality & Process Methods* (SAS Institute Inc., Cary, NC, USA, 2014).

[29] M. A. Mohammad, Et al. “Nanofabrication Handbook” (CRC Press, 2012), pp. 11–41.

Chapter 8. – Planar plasmonic bean-like nano-structures for high dichroic filtering: theory, fabrication and experiment.

8.1. - Introduction.

Surface Plasmon Polaritons (SPPs) [1] are e.m. waves that propagate along the interface between metallic layer and dielectric substrate. SPPs based devices have been demonstrated to be very attractive for photonic applications in many areas such as nano-optics [2, 3], high density optical data storage [4, 5], wave-guiding [6, 7], near-field optical microscopy [8, 9] and biomedical sensing [10, 11], because of their sub-wavelength scale features and field enhancement effect [12]. The plasmonic structures can also enhance interaction with circularly polarized light and some exhibit strong chiroptical effect [13]; thus, in the recent years chiral plasmonic nanostructures have gained substantial interest [14, 15]. At the state of the art, these structures exhibit a high amount of circular dichroism compared to common biomolecules [16, 17], but it can also massively enhance the signal obtained from them, as reported in [18]. Many ways to exploit this are being researched in order to produce a high sensitivity device which can detect the handedness of a given molecule [19].

In this section we introduce a new planar geometry through which we have been able to achieve a high value of circular dichroic factor(CDF) over a large bandwidth. The samples have been produced through an accurate top-down fabrication by using electron beam lithography (EBL) to shape a high quality thin Au layer on ITO substrate.

While the state of the art for 3D dichroic devices reach a CDF of 37% [20], our 2D structure shows measured CDF of 17%; our theoretical analysis shows that we can reach CDF values up to 60% over a bandwidth of 100nm; our planar dichroic structures are also cheaper to build in comparison with 3D structures, since they require just one lithography process.

In the subsection 2 we present the theoretical study and numerical methods used for the design and optimization of the geometries. In the subsection III we report the details of the fabrication of the devices. In section IV the measurement setup and the final results are shown. Finally, the main conclusions are drawn.

8.2. - Theoretical Project and FDTD Analysis.

The beginning design has been performed by means of FDTD instruments, this choice is due to the fact that for the plasmonic devices, which have geometries of hundreds of nanometer, FDTD numerical methods are able to perform 3D projection with the minimal use of computational power.

In Fig. 8.2 it is reported the base unit cell for the numerical calculation: the single unit is a generic gold Archimedean spiral on a ITO substrate; the mutual distance and

the filament cross section have been set in in order to prevent collisions and deformations during the growing process. The general 2D profile follows a triangular scheme of identical units, which have been rotated of 120° to prevent any form of linear on-plane anisotropy. Finally, the elongated stripes are been engineered to obtain a variable angular extension, exceeding from a fixed offset value, we have set the angular extension for the final structures in order to obtain the best circular dichroism (CD) performances; in Fig. 8.2. is reported the final base unit cell choice for the calculation method.

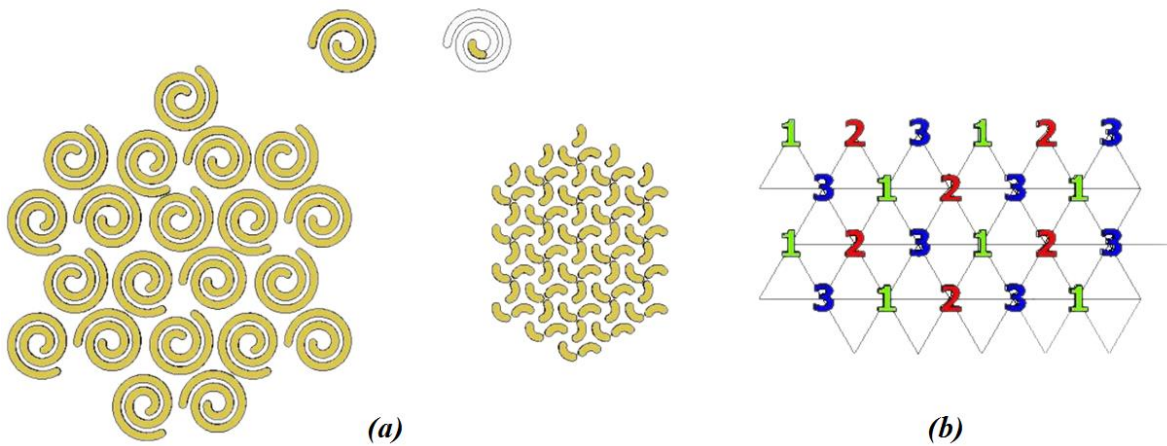


Figure 8.1. (a)The single unit is an Archimedean spiral: the elongated stripes have a variable angular extension; the units are been rotated of 120° . (b)The 2D profile follow a equilateral triangular scheme.

The 3D box is perfectly squared but properly cut in order to reproduce the effect of a triangular distribution with the aid of PBC set at its boundaries.

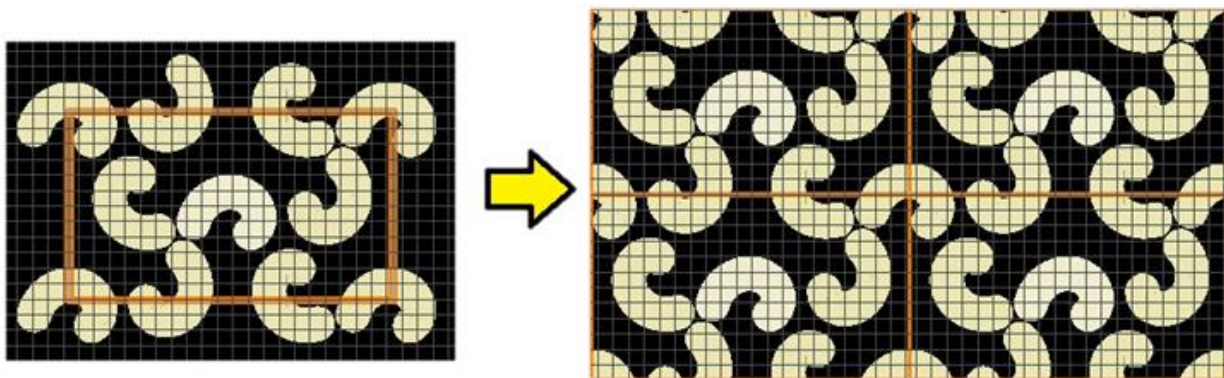


Figure 8.2. The base cell for the calculation method: the angular extension is chosen to obtain the best CD performances; with the PBC boundaries we can simulate all the device creating a perfect periodic distributions of identical units.

Therefore, with PML at opposite sides, we have inspected the far-field transmission, under normal illumination of the base cell; we made a set of simulations varying the structures thickness between an initial value of 50nm and 300nm.

For each simulated configuration we recorded the CD calculated as:

$$CD = 2 \frac{T^+ - T^-}{T^+ + T^-} \quad (8.1)$$

where T^+ and T^- are the output transmission spectra for left and right circularly polarized impinging waves, respectively, in a large spectral window ranging from the near-infrared to UV frequencies, evaluating only the fundamental scattered mode.

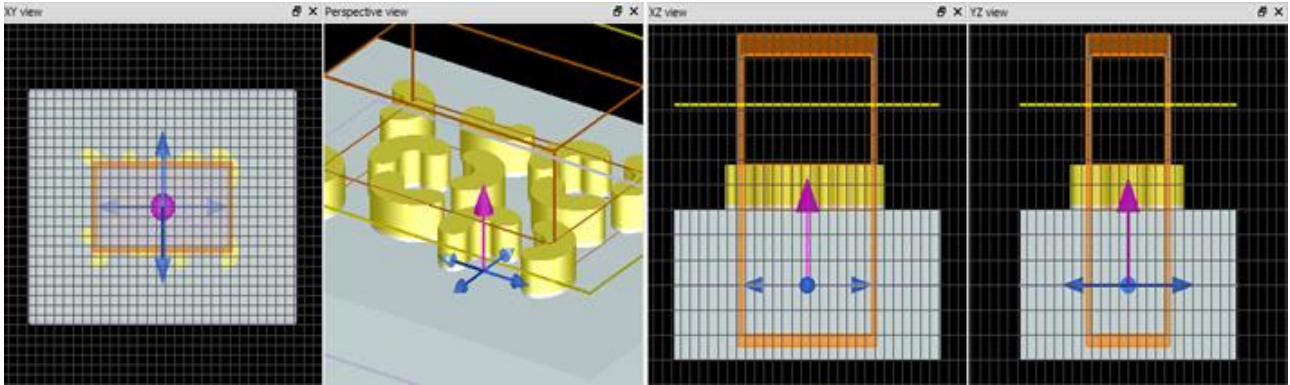


Figure 8.3. The Lumerical FDTD 3D box interfaces: the e.m. source is placed in the glass layer, under the gold structures, in the bottom of the simulation area.

In figure 8.4 are reported the simulation results: the predicted CD levels exceeds 60%, with remarkable resonances spectrally located in quite stable regions despite structural variations. We have decided to set the nano-bean thickness at 210nm (Fig. 8.4(a)) that guarantees a good CD coefficient (20%) in a large bandwidth (800-900nm).

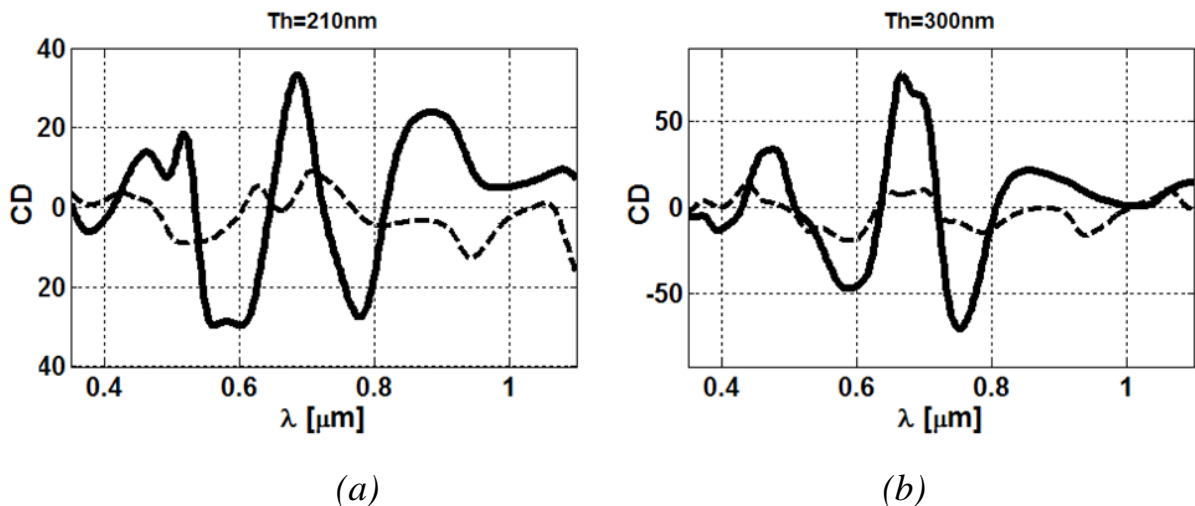


Figure 8.4. The simulation results: on x-axis the wavelength and on y-axis the CD. We can reach an a CD value greater than 60% in structures with a thickness of 300nm; we have chosen 210nm of gold thickness because it guarantee a more stable CD value, around 20%, in a larger bandwidth: 800-900nm.

8.3. - Fabrication process flow of the nano-beans.

Following is reported the fabrication process flow of the device:

- I. 650nm of PMMA e-resist is deposited by spin-coating on the ITO substrate.
- II. EBL process to imprint the geometry on the PMMA.
- III. PMMA developing after EBL process.
- IV. Vacuum deposition of 210nm of gold.
- V. Removing of the PMMA residual by using acetone.

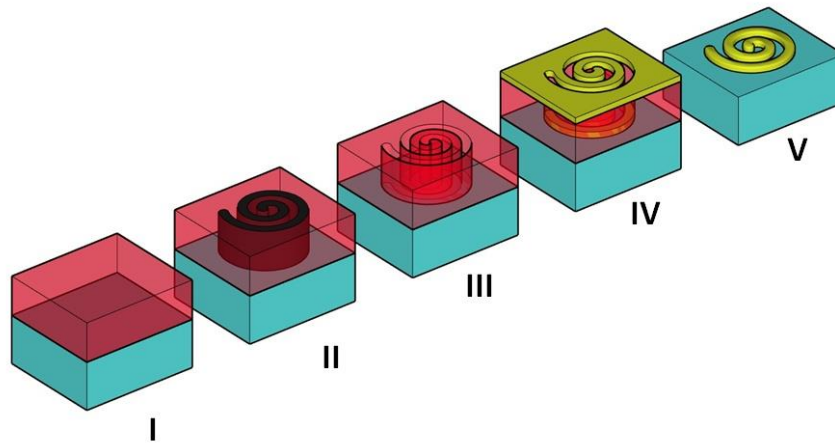
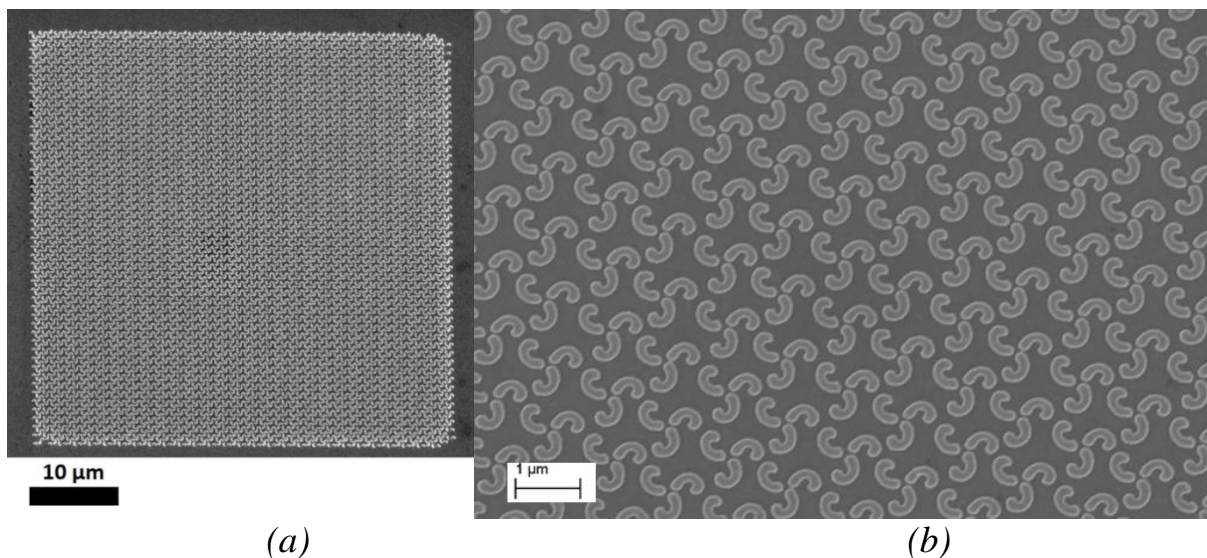


Figure 8.5. 3D schematic view of the fabrication process flow of the nano-beans.

The fabrication result is showed in Fig 8.6 - 8.7 current samples are $50 \times 50 \mu\text{m}$ and $100 \times 100 \mu\text{m}$, but this technique is highly scalable to bigger surface areas.



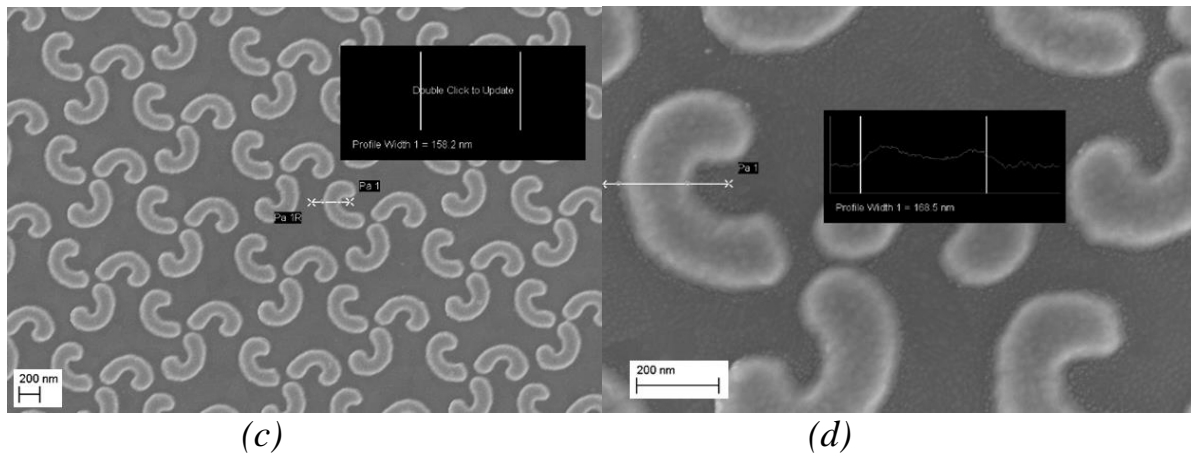


Figure 8. 6. SEM images of a general view of the device. The details are gradually zoomed from (a) to (d).

For each sample there are manufacture different areas with a gradually increase of the structure width; are shown below the SEM images of area 6.

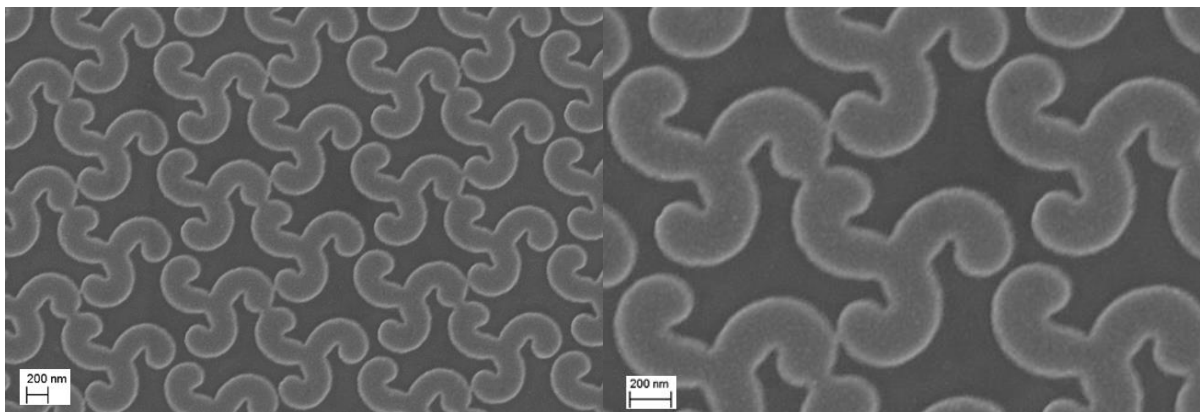


Figure 8.7. SEM images of the area 6.

8.4. - Measurement setup and results.

The sample was optically studied by normal incidence transmission made with an home-made confocal setup. Light from a tungsten lamp was collimated and focused on the sample by an adjustable numerical aperture condenser (from 0.05 to 0.95). For normal incidence, the minimum numerical aperture was used, corresponding to a semi-aperture incidence angle of less than 3° . Circular polarization was obtained by means of a linear polarizer coupled to a broadband quarter wave-plate (Zeiss Microscopy, item number 445226-0000-000). Transmitted light was collected by a 10x 0.45 NA objective lens coupled to three cascaded (focusing, collimating and refocusing) lenses, and analysed with a CCD camera coupled to a mono-chromator. Optical transmission was evaluated with respect to the light transmitted through the bare glass substrate.

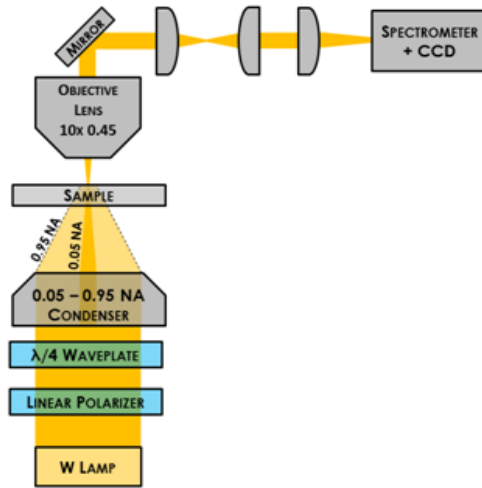


Figure 8.8. Schematic view of the measurement setup.

The measurement result is shown in figure 8.9 we can reach a CD of 17% in the area 6 over a bandwidth between 800nm and 900nm; the result is very next to the simulation's projections of section 8.2.

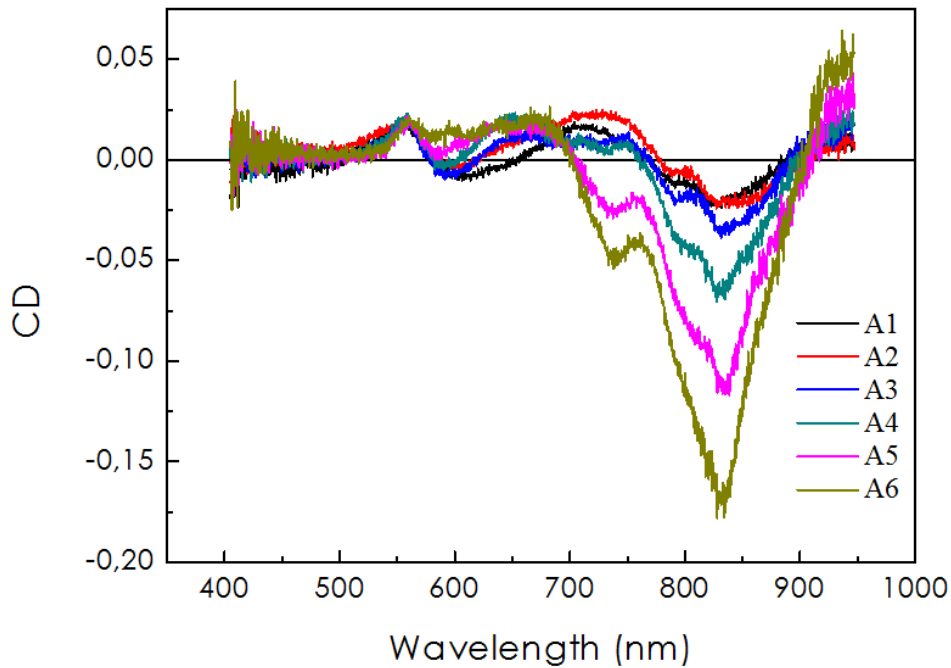


Figure 8.9. Measurement result: on the x-axis we have the wavelength and on the y-axis the measure CD.

These CD values make the sample competitive with 3D helix devices [20], which are extremely efficient but require major costs.

8.5. - Conclusions.

The device showed high CD levels in transmission over a large range of frequencies, demonstrating that the construction technique is the winning one in producing cheap but reliable samples. Together with their basic role of optical filters, we aim this class of cheap, resistant, durable, and fast produced metasurfaces to be used also as good support for cheap enantiomeric bio-sensing systems and optical integrated circuits [21 - 23].

8.6. - References.

- [1] S. A. Maier. “Plasmonics: fundamentals and applications”. Springer Science Business Media LLC, (2007).
- [2] W.L. Barnes, Et al. “Surface plasmon subwavelength optics”, *nature*, Vol 424,(2003).
- [3] J. Miao, Et al.“Far-Field Focusing of Spiral Plasmonic Lens”. *Plasmonics*, 7:377–381, (2012).
- [4] M. Mansuripur, Et al.“Plasmonic Nano-structures for Optical Data Storage”. OSA, (2009).
- [5] H. Ditlbacher, Et al.“Spectrally coded optical data storage by metal nanoparticles”. *Optic letters*, Vol. 25, No. 8, (2000).
- [6] S. I. Bozhevolnyi, Et al.“Channel plasmon subwavelength waveguide components including interferometers and ring resonators”, *nature*, Vol 440, (2006).
- [7] A. Mahgir, Et al. “Plasmonic coaxial waveguide-cavity devices”. OSA, Vol. 23, No. 16, (2015).
- [8] T. J. Antosiewicz, Et al.“Performance of Scanning Near-Field Optical Microscope Probes with Single Groove and Various Metal Coatings”. *Plasmonics* 6:11–18, (2011).
- [9] T.Ishi, Et al. “Si Nano-Photodiode with a Surface Plasmon Antenna”. *jjap*, Vol. 44, No. 12, (2005).
- [10] O. S. Wolfbeis. “Fiber-Optic Chemical Sensors and Biosensors”, *Anal. Chem.* 76, 3269-3284, (2004).
- [11] K. Kurihara, Et al. “Fiber-optic conical microsensors for surface plasmon resonance using chemically etched single-mode fiber”. *Analytica Chimica Acta* 523, 165–170, (2004).
- [12] W. Knoll.“Interfaces and thin films as seen by bound electromagnetic waves”. *Annu. Rev. Phys. Chem.* 49:569–638, (1998).
- [13] V. K. Valev, Et al. “Chirality and Chiroptical Effects in Plasmonic Nanostructures: Fundamentals, Recent Progress, and Outlook”, *Adv. Mater.* 25, 2517–2534, (2013).
- [14] M. Schaferling, Et al.“Tailoring Enhanced Optical Chirality: Design Principles for Chiral Plasmonic Nanostructures”, *Phys. Rev. X* 2, 031010, (2012).

- [15] A. O. Govorov, Et al. “Theory of Circular Dichroism of Nanomaterials Comprising Chiral Molecules and Nanocrystals: Plasmon Enhancement, Dipole Interactions, and Dielectric Effects”. *Nano Lett.* 10, 1374–1382, (2010).
- [16] Tun Cao, Et al. “Extrinsic 2D chirality: giant circular conversion dichroism from a metal-dielectric-metal square array”, doi 10.1038/srep07442, (2014).
- [17] M. Kuwata-Gonokami, Et al. “Giant Optical Activity in Quasi-Two-Dimensional Planar Nanostructures”, *PRL* 95, 227401, (2005).
- [18] A.O. Govorov. “Plasmon-Induced Circular Dichroism of a Chiral Molecule in the Vicinity of Metal Nanocrystals. Application to Various Geometries”, *J. Phys. Chem. C* 115, 7914–7923, (2011).
- [19] N. A. Abdulrahman, Et al. “Induced Chirality through Electromagnetic Coupling between Chiral Molecular Layers and Plasmonic Nanostructures”. *Nano Lett.* 12, 977–983, (2012).
- [20] M. Esposito, Et al. “Triple-helical nanowires by tomographic rotatory growth for chiral photonics”. ncomms7484. doi: 10.1038, (2015).
- [21] A.O.Govorov, *J.Phys.Chem. C*, Vol.115, No.16, 7914–7923, (2011).
- [22] N.A. Abdulrahman et al. *NanoLett.* Vol.12, pp.977–983, (2012).
- [23] B.Alam Et al. *Journ.Appl.Phys.* Vol.120, Is.8 (2016).

Chapter 9. – Conclusion.

As already stated previously, research on plasmonic and optical & THz metamaterial structures is mature from analytical and numerical points of view; today, the challenge is represented by the effective synthesis of the theoretical studies into actual working devices. Following this aim, my research activities have been divided in two main phases.

At first, I have participated in numerical and analytical analyses, focused on the design of various optical elements based on plasmonics and metamaterials. This way, other than the actual scientific results, I have also obtained knowledge and skills on the state of the art. In chapter 2, I have presented the theoretical fundamentals while, in the following three sections, I have shown such projects.

In chapter 3, I have presented the study on the transmission properties of a new kind of meta-surfaces: gold plasmonic nano-resonators grown on a layer of polystyrene spheres; by the use of Lumerical FDTD, I have analyzed the transmission properties both for linear and circular polarization of the impinging wave, obtaining the electromagnetic field distribution and the general dichroism of the structures. So, by varying the deposition parameter of the gold nano-resonators, through our methods it is possible to predict both field distribution and dichroism; thus, such device can be used to produce an efficient and versatile dichroic filter, such as circular polarized and optical rotators for visible light and near infrared frequencies. This theoretical work has been completed and published on [1].

In chapter 4, I have introduced an efficient method to estimate the 2D irradiation diagram (ID) for a linear cluster of various scatterers aligned to form a plasmonic grating impinged by SPP. The method was made with a structured algorithm that combines the electromagnetic properties of its compounding elements: the superposition of all the scattered and transmitted H fields allows the calculation of the ID for the entire structure. Such approach can provide a full-2D ID prediction without requiring high levels of computational time and hardware resources. The technique allows to design a correctly customized plasmonic gratings to promote a desired emission pattern from optical integrated components. This work was published in [2].

In chapter 5, I have shown an analysis on vertical directional couplers (VDCs) with long range surface plasmons (LR-SPP) in order to discern information about their overall interactions and to find suitable parametric choices to design them. A new method has been introduced and used to compute the interaction in the s-bend region. The study shows that the "additional" coupling is strong and significant, but it can also be controlled by tuning the geometrical parameters, in particular the bend radius. The interest in this element comes from the "topological" advantage it may give to Optical Integrated Circuits based on LR-SPPs: while technological characteristics (in particular the polymeric claddings) allow to stack vertically various layers of circuits, VDCs enable an interlayer communication; this makes LR-SPPs the ideal technology for Multilayer optical integrated circuits, capable of satisfying the needs of present and

future Network-On-Chip systems. This work was published in [3], and currently samples are being developed [9].

In the second part of my PhD, my research focused on the fabrication of elements: by using the same top-down approach from micro/nano-electronics, I have developed methods to nanofabricate plasmonics and metamaterials based devices. I have described the fundamentals in chapter 6.

The first fabricated element was a grating placed on a gold thin layer with the schemes obtained from calculation produced in chapter 4. For this aim, as shown in chapter 7, I performed an extensive study on the Electron Beam Lithography (EBL) instrument, by a statistic process flow, in order to find the best working condition. Multiple samples have been produced, and are now ready to be measured and optimized. The same tools, used for the fabrication of the gratings, have been implemented also for other devices, like the Nano-sieve polyimide filter for microfluidic sensing on lab-on-chip presented in appendix [A.1]. At the end of chapter 7, I have also presented the process flow used to micro-manufacture a metamaterials based THz absorber; in this case I used UV-lithography instead of EBL because of the device dimension. The absorber has been successfully produced, and is now being characterised.

In chapter 8, I have presented the development on a dichroic filter based on a planar plasmonic nanostructured metamaterials. The structures, thanks to their good response as optical filter, can be used as good support for cheap enantiomeric bio-sensing system and optical integrated circuits. First the devices were designed through numerical methods with Lumerical FDTD and Matlab environment; then the device has been manufactured through an accurate lift-off process and the use of EBL instrument. The samples have been characterized in CNR-Nanotech labs: the results showed a high Circular Dichroism Factor in transmission over a large range of wavelengths, confirming the numerical results. The first results have been submitted [10].

During the actual fabrication of the devices, I had to deal with a wide range of non-idealities: the precision of the geometrical shapes, materials' physical conditions, and also measurement setups, are not always to be taken as granted. A key aspect to take into account is the set of feedbacks from the fabrication process and the theoretical study; there have been many modifications on the analyses ending sometimes on an increase in computational complexity, sometimes in compromises and a reduction of performance prospects.

I can also state the validity and the efficiency of the fabrication methods used extensively during these research activities; metal deposition by thermal evaporation and lift-off have granted excellent flatness and uniformity to the plasmonic metamaterials I have produced; also, EBL has proven to be a very precise, dependable and versatile instrument for the definition of the geometry. Despite the non-idealities, the quality of the final samples, as shown by the various SEM images, is still very good and their performances are relevant, as demonstrated by the preliminary measurements. Overall, our works have demonstrated the effectiveness of plasmonics and metamaterials as enhancing factors of present and future sensors and circuit elements;

we predict further development of these research fields for the next years, as well as an increase of their applications.

9.1. - Author's bibliography.

PUBLICATIONS:

- [1] A. Benedetti, A. Belardini, A. Veroli, M. Centini and C. Sibilìa, "Numerical tailoring of linear response from plasmonic nano-resonators grown on a polystyrene spheres layer". J. Appl. Phys. 116, (2014); doi: 10.1063/1.4900992.
- [2] A. Benedetti, A. Veroli, C. Sibilìa, and F. A. Bovino, "Numerical evaluation of irradiation diagram by plasmonic gratings and slit apertures". J. Opt. Soc. Am. B, Vol. 32, No. 4 (2015).
- [3] B. Alam, A. Veroli and A. Benedetti. "Analysis on vertical directional couplers with long range surface plasmons for multilayer optical routing". J. Appl. Phys. 120, (2016); doi: 10.1063/1.4961419.

PROCEEDING:

- [4] F. Bovino, A. Benedetti, A. Veroli, C. Sibilìa. "On the controllable optical beam direction by means of nanopatterned plasmonic device". Proc. SPIE 9126, Nanophotonics V, (2014); doi:10.1117/12.2052495.
- [5] F. Bovino, A. Benedetti; A. Veroli; C. Sibilìa. "Controllable Optical Beam Scan by Means of Nanopatterned Plasmonics Device". Fotonica 2014 Napoli.
- [6] A. Benedetti, A. Veroli, C. Sibilìa, F. Bovino. "Accurate Numerical Procedure for Fast Evaluation of the Irradiation Diagram From Scatterers in The Optical Domain". S.E.D.A. 2014 (The 3rd International Conference in Software Engineering for Defense Applications).
- [7] A. Veroli, F. Mura, M. Balucani and R. Cammini. "Dose influence on the PMMA e-Resist for the development of high-aspect ratio and reproducible nanostructures by Electron Beam Lithography". AIP Conference Proceedings 1749, (2016); doi:10.1063/1.4954493
- [8] M. Muzi, A. Veroli, A. Buzzin, B. Alam, G. De Cesare, D. Caputo, L. Maiolo, M. Marrani, F. Frezza. "Nano-sieve filter for microfluidic sensing on lab-on-chip". Poster submission at Nano Innovation 2016.

[9] B. Alam, A. Veroli, A. Benedetti. “Multilayer optical routing by means of vertical directional coupler with long range surface plasmons”. Poster submission at Nano Innovation 2016.

[10] A. Veroli, B. Alam, L. Maiolo, F. Mura, R. Camminiti, F. Todisco, M. De Giorgi, L. Dominici, A. Benedetti. “Planar plasmonic bean-Like nano structures for high dichroic filtering: theory, fabrication and experiment”. Poster submission at Nano Innovation 2016.

Acknowledgments.

The author want to thank all the people who have contribute to the results of his PhD work. First of all my parents: Anna and Claudio and granmother Teresa for their fundamental support in this years. My friends and colleagues Badrul Alam, Alessio Benedetti and Alessio Buzzin for the professionalism with they have supported my projects; finally, I mention Luca Maiolo, Francesco Mura, Gregory Leahu and Prof. Ruggero Camminiti for their outstanding contribution to my research.

Appendices.

A.1. - Nano-sieve filter for microfluidic sensing on lab-on-chip.

With technologies acquired in the assemblage of the gold grating, in particular with the features of the EBL instrument, it is possible to realize a wide range of different devices. In this subsection is reported how is possible to produce a polyimide sieve for biomedical applications in microfluidic systems.

During last years we have assisted to an increasing interest on the integration of opto-electronic and mechanical devices in lab-on-chip systems for biomolecular detection [1, 2]and analysis of cell culture behavior [3, 4]. An important task is to operate an efficient mechanical separation of the suspended particulate of a biological material in order to simplify its study and characterization; from this point of view we have studied a new fabrication method to produce a **polyimide-based nano-sieve** for biomedical applications in microfluidic systems.

We have chosen the polyimide for different reasons: it is lightweight, flexible, resistant either to heat and chemicals and it can form stable bonds with most of metals. It is traditionally used as stress buffer/passivation layer over semiconductor circuitry and now It is having extensive use in MEMS applications.

For the design of the nano-sieve it was decided to start with an orthogonally alterned groove patterns (fig. 1).

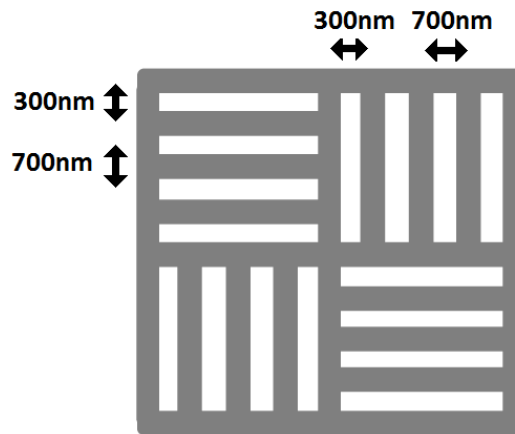


Figure 1. Schematic 2D vision of the design used for the polyimide nano-sieve: the width of the lines is 300nm spaced 700nm.

The width of the stripe lines is 300nm spaced 700nm and the thickness of the polyimide is 6 μ m; so, the device turns out to have an high aspect ratio (1:20). Therefore the following fabrication method can be replicated implementing various geometries (keeping the same aspect ratio) in order to sifting different kinds of suspended cells/particulate.

In fig. 2 is reported the fabrication process flow for the device:

- I. Oxidized silicon substrate.
- II. Deposition of a 6 μ m-thick polyimide film by spin-coating on the silicon substrate and curing in a vacuum oven.
- III. Vacuum evaporation of a 40 nm- thick Al film.
- IV. Spin coating of a 600 nm-thick PMMA e-resist layer.
- V. Electron Beam Lithography (Area Dose = 500 μ C/cm²) to imprint the nano-sieve geometry on the PMMA film.
- VI. Pattern definition on the Al film by wet etching.
- VII. Pattern imprinting on the polyimide film by Reactive Ion Etching (RIE).
- VIII. Peeling of the **nano-sieve** from the substrate.

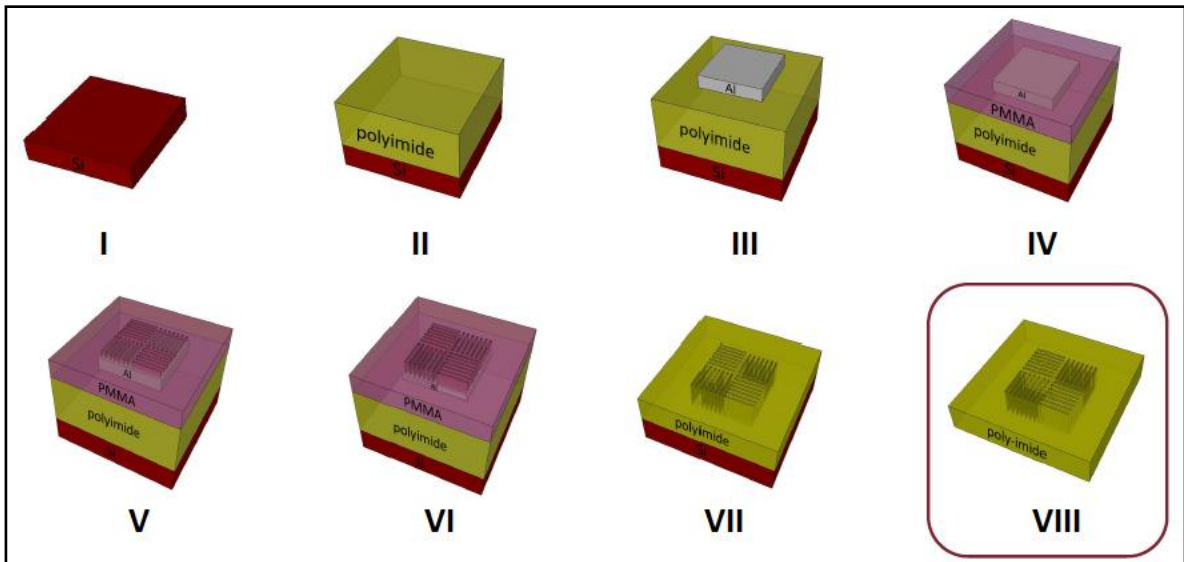


Figure 2: 3D schematic view of the fabrication process flow of the polyimide nano-sieve.

The device, successfully manufactured is shown in fig. 3.

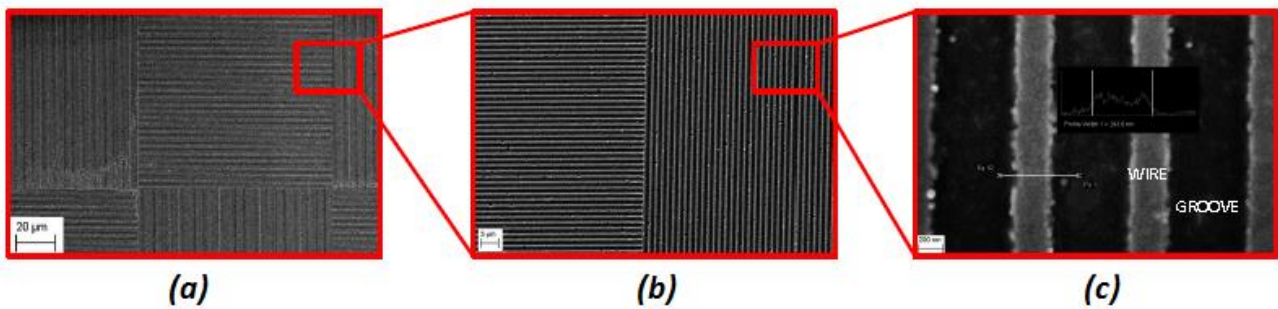


Figure 3. The SEM images of a general view of the device is zoomed in to inspect the geometry details: (a) geometry overview; (b) orthogonal grooves pattern; (c) polyimide wires (300 nm wide) and grooves (700 nm wide).

From the results it is clear that the fabrication procedure for manufacturing nano-sieve devices is correct, reaching an aspect ratio of **1:20**. The polyimide structure will be implemented in a more complex microfluidic networks to analyse biological material in lab-on-a-chip systems.

A.2. - Nano electro-mechanical systems.

During my PhD work I have created a nanofabrication top-down procedure, which can be used to manufacture different type of heterogeneous devices. These results may be useful not only in the metamaterial field, but can drive on new research perspectives in different areas. The capacity of the EBL instrument to generate geometries with the nanometer detail was recently employed, with the set of fabrication techniques and methods exposed, in order to produce a new type of *Nano Electro-Mechanical Systems* (NENS) (Fig. 4).

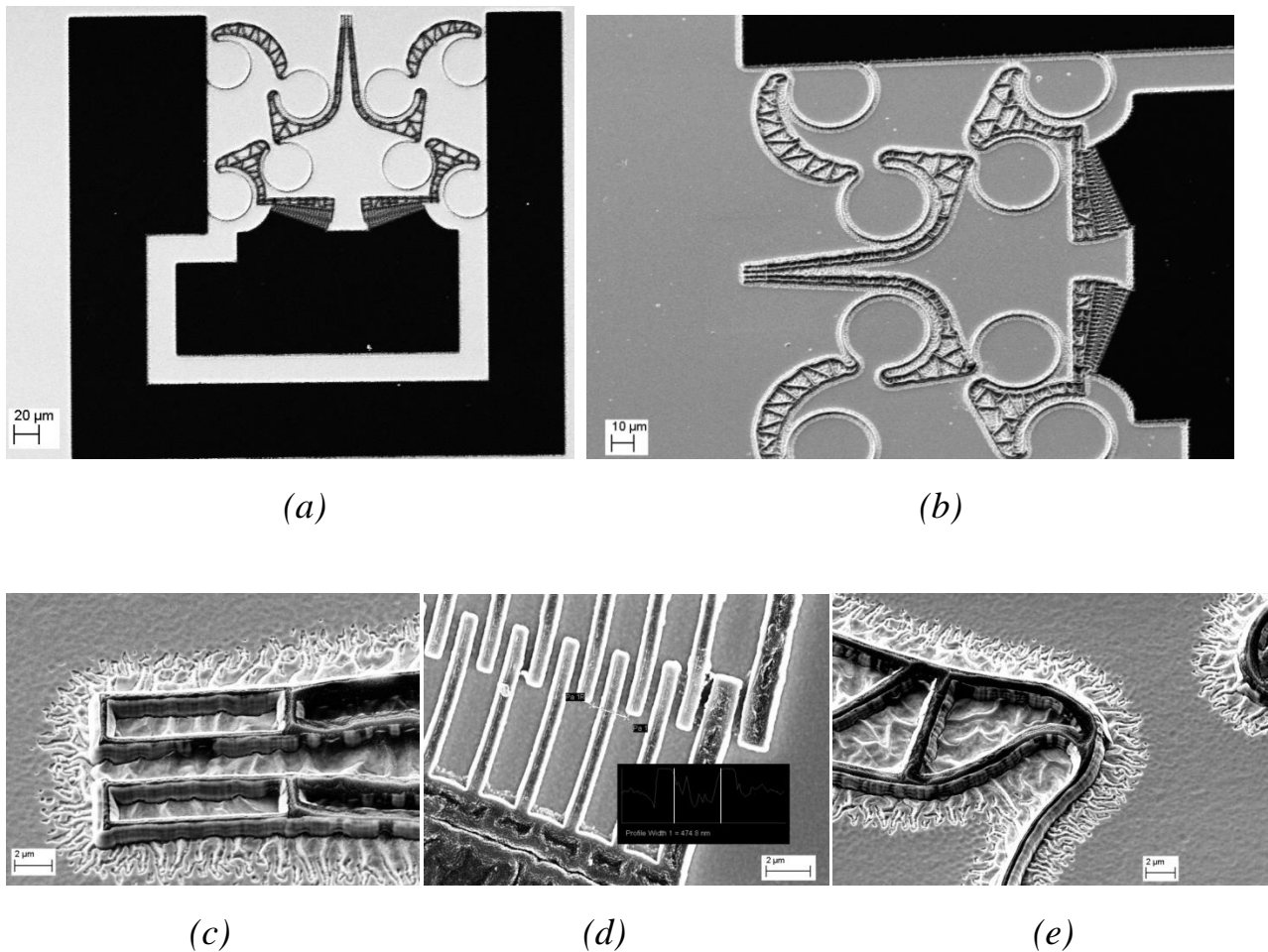


Figure 4. The SEM images of the nano electro-mechanical device: (a) top view of the device; (b) angular vision, the sample is tilted of 35°; (c-e) detail of the areas.

The construction of the device is still in the development phase, but it may have a wide application in medicine and robotic field.

A.3 - References

- [1] D. Caputo, et al. "Lab-on-glass system for DNA analysis using thin and thick film technologies."MRS Proceedings. Vol. 1191. Cambridge University Press, 2009.
- [2] B. Alam, Et al. "Analysis on vertical directional couplers with long range surface plasmons for multilayer optical routing."Journal of Applied Physics 120.8 (2016).
- [3] F. Frezza, Et al. "In silico validation procedure for cell volume fraction estimation through dielectric spectroscopy". Journal of biological physics, vol. 41(3), 223-234, (2015).
- [4] M. Muzi, Et al, "Hierarchical in silico validation procedure for biomass estimation techniques based on dielectric spectroscopy", Proceedings of: XX RINEM, September 10th-14th, 2014, Padua, Italy.